博士論文

論文題目

High-speed electrical gating of single electron spin qubits with semiconductor quantum dots
（半導体量子ドットを用いた単一電子スピン量子ビットの高速電気制御）

氏名　　米田　淳

Dissertation Supervisor: Professor Seigo Tarucha Author: Jun Yoneda

High-speed electrical gating of single electron spin qubits with semiconductor quantum dots

Abstract

Requirement of scalability has made solid-state implementations exceptionally attractive in the search for future quantum computing architectures. Spins in quantum dots (QDs) are regarded as one of the most promising among them. Recent experiments have shown that spins in electrically-controlled semiconductor QDs meet many prerequisites for quantum computers. However, the ability to manipulate qubits on timescales much shorter than the coherence time, which lies at the heart of quantum computation, has been elusive in this system. In contrast to exchange-mediated two-qubit operations in less than a nanosecond, single spin rotations via ESR are slow, due to small amplitudes of the Rabi a.c. magnetic field. Despite intensive efforts, it is still technically challenging to achieve spin flip times (T_π) much shorter than the ensemble phase coherence time (T_2^*) limited by the interaction with the surrounding nuclear spins in the host material.

This thesis presents high-speed manipulations of a single electron spin confined in GaAs semiconductor QDs. To overcome the problem of a weak ESR driving field compared with the hyperfine field, we utilize an on-chip micromagnet (MM). The MM-induced stray field gradient couples the electron's spin degrees of freedom to an oscillating electric field or microwave (MW) and allows for electrically driven ESR. In order to achieve spin rotations faster than the dephasing, we refine the MM design and the QD device design of the preceding MM-ESR experiments. We achieve above 120 MHz Rabi oscillations, the fastest in the electrically-controlled QDs, with T_π roughly an order of magnitude shorter than T_2^*. Vanishing effects of nuclear spins in the fast Rabi oscillation are evidenced by observation of no initial $\pi/4$ phase shift and a chevron interference pattern. We also establish for the first time direct control of spin phase, which serves as a single-step z-rotation gate. We demonstrate above 50 MHz phase rotation, providing a faster implementation of phase gates such as the so-called $\pi/8$ gate than with the 120 MHz ESR.

Based on the fast spin operations demonstrated in this thesis, all required gate-times will become an order-of-magnitude shorter than T_2^* of the system, allowing high-fidelity single-qubit gates in a highly scalable platform with an established fast entangler. We therefore believe these achievements contribute to future advances in quantum information processing in QD systems, e.g. state tomography by fast ESR gates, CNOT gates incorporating phase shift gates. The observed recovery of the exponential coherence decay of the strongly-driven spin qubit (albeit coupled to the nuclear-spin bath with a long memory time) would be crucial for realization of quantum error correction. The MM techniques studied here should be also applicable to other material systems with longer coherence times, e.g. isotropically purified silicon- or carbon-based QDs.

Acknowledgements

The work presented in this thesis was obviously not completed by myself alone but with many people, in and outside the Tarucha group at the University of Tokyo. My sincerest gratitude belongs to Prof. Seigo Tarucha, who has given me the opportunity to work on this exciting subject in such a world-class environment. I wouldn't be here without his passionate one-on-one supervision (sometimes hours a day despite his crowded schedule) at "my place" in the basement laboratory room! He has also shared with me the experience and knowhow accumulated in the group over decades, high-end lab equipment free to use and the key tricks to make an appealing scientific presentation. Lecturer Akira Oiwa has always, practically every day, helped me out with major and minor puzzels and issues both in the clean room and the basement. The door to his office was always open (figuratively as well as literally), which considerably facilitated carrying out my research. Assistant Prof. Michihisa Yamamoto frequently helped me track down and solve the problems I encountered. His deep physical insight has been truly instructive especially at indecisive moments.

I owe more than words can say to our Spin-Qubit group members. I was very fortunate to be able to work closely with Dr. Tomohiro Otsuka, who guided me through the basics of electronics and cryogenics (using our "educational" dilution fridge). He designed and co-fabricated the double-dot device presented in this thesis and constructed the initial experimental setup from scratch! He has also introduced many innovative experimental technologies to our lab, and offered virtually any support that helped me concentrate on physics. Dr. Toshiaki Obata designed the high-bandwidth chip carriers and device holders without which I wouldn't have succeeded in the ESR experiments. He has also not only been a reliable source of cryogenic and craft techniques, but also a source of everyday laughter as well. Dr. Tatsuki Takakura kindly

coached me on the fine art of device design and fabrication when I was still a stranger to this field, and has given me valuable, experience-based suggestions on device tuning. The triple-dot experiments were performed with Mr. Akito Noiri, an industrious student who quickly absorbed all the spin-qubit-related knowledge that I had to offer and swiftly began contributing to our project. His passion has never died in spite of repeated untimely deaths of working devices caused by uncontrollable failures of the fridge! Dr. Takashi Nakajima has always been a pleasant person to discuss physics with, and often provided me with the perspective that I was seeking. I am in debt for the digitizer-board program to Dr. Matthieu Delbecq, which finally made the longed-for fast data-processing available to us. I gratefully acknowledge frequent useful advice in the clean room from Mr. Kenta Takeda, who has spent definitely much longer time there despite being one year younger. I have been really pleased with the printed-circuit board for high-frequency experiments designed by our student Mr. Retsu Sugawara under supervision of Nakajima-san, Takeda-kun and me.

The idea of the phase-rotation experiments was conceived by Assistant Prof. Michel Pioro-Ladrière at the University of Sherbrooke, from whom I gained much insight into electron spin qubits and scientific reasoning. I would like to thank Prof. David Reilly at the University of Sydney and his group members, for letting me stay in their laboratory and learn readout techniques. The two-week experience in Australia has greatly improved my understanding of radio frequency technology, which I believe was integral for detecting the first reflectometry signals in our lab. I would like to acknowledge a long-term theoretical contribution to our group from Prof. Tokura at the University of Tsukuba. He kindly introduced to me the relevant theoretical frameworks and discussed the unexplained results with me, which made my picture of the physics in the experiment much clearer. None of the experiments presented here would have been possible without the high-quality 2DEG. We are fortunate to work in close collaboration with the Gossard group and the Palmstrøm group at U.C. Santa Barbara, the Manfra group at Purdue University and the Wieck group at Ruhr-Universität Bochum.

My five-year graduate life has turned out to be truly enjoyable, thanks to all the current and former lab staff and members who created this nice and open group atmosphere. I was especially lucky to join the lab in the same year

as two excellent PhD students. Having actually become group members one year earlier, they helped me as a former laser-physicist to kick off research on low-temperature transport. I would like to thank Mr. Takafumi Fujita also for being a good friend of mine for almost a decade (it's been such a long time since we entered the university and studied Spanish together!). He was always there for my random conversations for a change or a clue. Mr. Shintaro Takada always entertained us when chattering over everyday dinner at Morikawa, our favorite restaurant.

Last but definitely not least, my deep appreciation goes to my parents for their love, reassuring support and perpetual belief in me. Thank you.

Table of Contents

Chapter 1

Introduction

1.1 Background

Recent advances in semiconductor processing technology have realized nanometer scale artificial structures called quantum dots (QDs) [1]. As the number of trapped electrons approaches zero, these structures behave as quantum systems rather than as just tiny charged boxes. QDs are also referred to as artificial atoms, owing to the similarity in the electronic properties and the richness of observed quantum phenomena [2, 3]. A big difference from natural atoms, though, is in their external tunability. With QDs, electrostatic gates can be used to change the exact number of trapped electrons as well as the shape of the confinement potential. Furthermore, electrical contacts can be made to measure the electronic property on a single-electron level in a real-time manner [4, 5]. The QD system therefore offers an excellent experimental platform for investigating individual electrons and spins.

In 1998, Loss and DiVincenzo pointed out that a coupled QD array can physically implement quantum computation with single spins in a QD as quantum bits (qubits) [6]. The architecture is considered remarkably promising especially in terms of scalability, since it can be integrated in principle with the help of advanced industrial semiconductor technology. Multiple spins in a QD array will hold a long-lived superposition and entangled state, as spins are relatively insensitive to the environment in solid-state quantum systems [7]. Since the proposal, considerable scientific interest has been devoted to the spin

physics in electrically-controlled QDs, and now many of the prerequisites for quantum computers have been fulfilled, including preparation, manipulation and measurement of single spins in QDs [8].

1.2 Motivation of the Present Work

Any quantum operation on a collection of qubits can be approximated by a sequence of quantum gates from a finite set, a *universal gate set* [9]. A universal set can be constructed from only single- and two-qubit gates [10], the most canonical example being probably the controlled-NOT (CNOT) gate and single qubit rotations [11]. For single-electron-spin qubits with QDs, electron spin resonance (ESR) and the Heisenberg exchange interaction are the time-honored resources of single- and two-qubit gates, respectively. The group of gates induced by these interactions suffice for a universal gate set.

A general enemy to quantum computing is decoherence, in which the quantum information encoded in qubits is lost through interactions with the other systems [12]. At the same time, measurable susceptibility is required to control qubit states for information processing. This gives rise to a stringent requirement that a qubit has to be in uncontrolled manners isolated from, and in controlled ways tightly coupled to its environment.

The dominant source of decoherence in the case of electron spin qubits in QDs is the hyperfine interaction with surrounding nuclear spins in the host material [13, 14]. All manipulations must be performed within the imposed phase coherence time in order to be meaningful in light of quantum information.

Prior to this study, single-qubit rotation in this system was slow enough (typical gating time was several tens of nanoseconds in GaAs QDs), to let the electron spin heavily mix with the nuclear spins during operation. The long interaction with hyperfine fields makes the Rabi oscillations qualitatively deviate from the one expected from the Markovian Bloch equations [15, 16]. On the other hand, the two-qubit gating can be completed on much shorter timescales (less than a nanosecond) [17]. Realizing fast single-qubit gates compared with the hyperfine-induced dephasing in this architecture is, hence, an essential step toward quantum computation. Fast ESR would also provide means to probe single electron spin dynamics in solids from a viewpoint of basic science, and

may find applications in spintronics [18, 19].

In this work, we explore the micro-magnet (MM) technique [20, 21] to achieve fast electrical control of a single electron spin. Our tailored MM placed near the QD produces the large stray field gradient that strongly mediates the electron's spin coupling to an electric field, which allows for fast spin gating. We obtain above 120 MHz ESR, making the single-qubit gating time much shorter than the time-ensemble phase coherence time (T_2^*). The improved qubit control fidelity is evident from observations distinct from the conventional non-Markovian driven-spin dynamics. We also prove that the MM stray field can further be exploited for a single-spin rotation around the z-axis at above 50 MHz, which is not directly implementable by ESR rotations. We estimate the highest fidelities for spin- and phase-flip to be 97 % and 98 %, respectively, with substantially smaller infidelities than previously reported. These high-fidelity single spin operations are fast enough to perform all necessary gates in key quantum circuits within a fraction of T_2^*, together with the established two-qubit gates through the exchange interaction.

1.3 Organization of this Dissertation

Chapter 2 describes the basic electrical properties of QDs. Transport currents and stability diagrams of single, double and triple QDs are discussed.

Chapter 3 gives a brief introduction to spin qubits with QDs. Spin states in few-electron QDs are explained. Important previous achievements in this field are partially listed. Methods for spin manipulations in QDs, including various ESR implementations, are theoretically reviewed.

In Chapter 4, optimization of the MM design is discussed. Required properties of the stray field for fast electrical spin manipulations are clarified. Based on simulation taking into account the effect of misalignment, a general scheme to properly design MMs for QD-based spin qubit devices is presented.

In Chapter 5, fast MM-ESR experiments with a GaAs-based double QD are described. Enhanced inhomogeneity in the local magnetic field induced by the MM is exemplified by a large ($\sim$ 100 mT) ESR peak separation. The shortest spin flip time of no longer than 4 nanoseconds is much shorter than T_2^*, several tens of nanoseconds. The maximum Rabi frequency of 127 MHz in this

experiment is the largest ever reported in electrically controlled QD systems.

In Chapter 6, distinct features of fast ESR are analyzed. ESR driving stronger than the Overhauser field fluctuation is evidenced by the phase shift and the decay function of Rabi oscillations. Chevron pattern of ESR spin flip signals is presented, together with simulation results, as another proof of strong driving.

In Chapter 7, direct control of single-spin phase is demonstrated. Electrical gating of the Zeeman field is shown by utilizing the spatial distribution of the MM stray field. This gives a control knob around the z-axis of a single spin, which is not directly accessible with ESR. Above 50 MHz Z gate operation is presented, providing an even faster implementation of small phase rotations than with 100 MHz ESR.

In Chapter 8, an attempt to expand the technique to a triple QD system is described.

Chapter 2

Theory of Quantum Dot Transport

QDs are small, typically nanometer scale, artificial structures in solids. Progress in nanotechnology has made it possible to fabricate QDs in semiconductors with a precise but gate-tunable number of electrons. QDs show many parallels with natural atoms, as the energy levels are quantized due to the confinement of the electrons in all three dimensions. Arising from their larger sizes and lower energy scales, however, QDs show different physical properties and provide better control over individual electrons.

This chapter explains the electronic properties of QDs. The basics of a single QD and laterally defined QDs are reviewed. Then charge configuration in multiple QDs such as double and triple QDs is theoretically discussed.

2.1 Electronic Properties of a Single Quantum Dot

In order to investigate its transport properties, a QD needs to be contacted to reservoirs with tunnel barriers, through which electrons can be exchanged (Fig. 2.1). To tune the electrostatic potential, gate electrodes can be incorporated, which are capacitively coupled to the QD. In such a setup, current-voltage measurements can be conducted while changing the QD properties, such as the number of trapped electrons and the couplings to the reservoirs, by

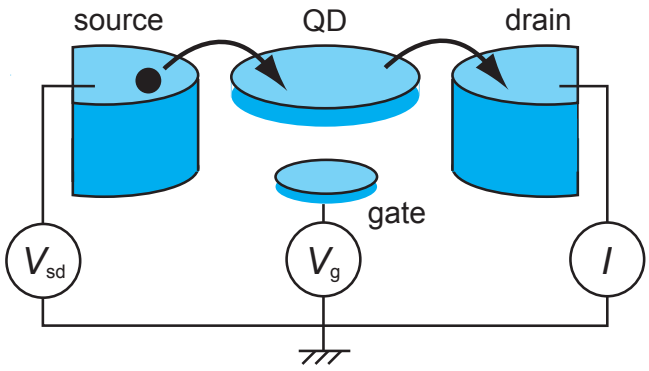

Figure 2.1: Schematics for electrical characterization of a QD. A QD is contacted with two reservoirs, source and drain. Finite bias V_{sd} is applied across the reservoirs and the current through the QD can be measured. In real devices more than one capacitively-coupled gates can be used to facilitate fine tuning of QD parameters.

sweeping the gate voltage. Notably, if properly tuned, currents through a QD oscillate as a function of the gate voltage, a characteristic behavior known as *Coulomb oscillation*. Current suppression at valleys of Coulomb oscillations is called *Coulomb blockade*. The aim of this section is to give a brief theoretical description of these unique phenomena observed in QDs.

2.1.1 The Constant Interaction Model

We introduce the Constant Interaction (CI) model to explain the basic transport features of a single QD [3]. The model approximates the energy level spectra in a single QD based on the following two important assumptions: (1) Coulomb interactions of a trapped electron with all other surrounding electrons, inside and outside the QD, are parameterized by a single constant capacitance C. (2) The non-interacting, single-particle energy level spectrum of the electrons is unchanged by the interactions. The total energy U of a QD with N electrons in the ground state is then given by

$$U(N) = \frac{1}{2C}[-e(N - N_0) + C_S V_S + C_D V_D + C_G V_G]^2 + \sum_{n=1}^{N} E_n(B), \qquad (2.1)$$

where $-e$ is the single electron charge and $N_0 e$ is the amount of charge in the QD that compensates for the positive background charge in the environment. The total capacitance C is given by $C = C_S + C_D + C_G$. The capacitances C_S, C_D, C_G are those of the QD with the source, the drain and the gate electrodes, respectively. V_S, V_D, and V_G are the voltages applied to the source, drain, and gate electrodes, respectively. The terms $C_S V_S$, $C_D V_D$, and $C_G V_G$ represent the charges induced by the voltages that change the electrostatic potential of the QD. The last term in Eq. (2.1) is the sum of the occupied single-particle energy levels, $E_n(B)$, which depend on the confinement potential and the external magnetic field B.

The *electrochemical potential* $\mu(N)$ is defined as the energy difference between the N-electron ground state GS(N) and the $(N-1)$-electron ground state GS($N-1$), i.e. $\mu(N) \equiv U(N) - U(N-1)$. From Eq. (2.1),

$$\mu(N) = \left(N - N_0 - \frac{1}{2}\right) E_C - \frac{E_C}{e}(C_S V_S + C_D V_D + C_G V_G) + E_N, \quad (2.2)$$

where $E_C = e^2/C$ is the *charging energy*. The first two terms are the electrostatic part and the last term is the chemical part. By definition, $\mu(N)$ corresponds to the energy required to add the N-th electron to the QD ground state. The *addition energy* is the difference in the electrochemical potentials between successive ground states and is given by

$$E_{add}(N) \equiv \mu(N+1) - \mu(N) = E_C + \Delta E. \quad (2.3)$$

$E_{add}(N)$ contains the charging energy, $E_C = e^2/C$, and the energy spacing $\Delta E = E_{N+1} - E_N$. $\Delta E = 0$ only when two spin-degenerate electrons are added to the same orbital.

Tunneling through a QD is determined by how electrochemical potentials in the QD are aligned with those of the source, μ_S, and the drain, μ_D. Here the electron temperature is assumed low enough compared with the charging energy E_C and the energy spacing ΔE, i.e. $k_B T \ll E_C, \Delta E$ with k_B the Boltzmann constant. A bias voltage $V_{SD} = V_S - V_D$ across the source and the drain opens an energy window, or a *bias window*, between μ_S and μ_D with a gap of $e|V_{SD}|$. When the QD electrochemical potentials lie within the bias window, electrons

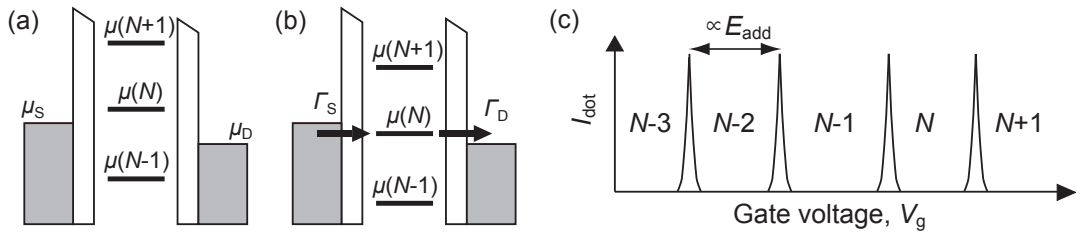

Figure 2.2: Coulomb oscillation. (a) Electrochemical potentials of a single QD in the Coulomb blockade. Tunneling is blocked since there is no level in the bias window. (b) Electrochemical potentials at a Coulomb peak. At Coulomb peaks, a single electron can tunnel from the source into the QD with $N-1$ electrons, and can tunnel out from the QD with N electrons to the drain. (c) $I_{\rm dot}$ oscillation in the low bias regime as a function of gate voltage. Note that the electrochemical potential is shifted proportionally to the gate voltage, while the total energy is changed quadratically. The dependence on the electron number N is also linear. Therefore, the whole *ladder* of the electrochemical potentials can be shifted up and down by the gate voltage while keeping the energy-level separation constant. At the Coulomb peaks of $I_{\rm dot}$, single-electron tunneling takes place since an electrochemical potential exists in the bias window. Between the peaks, on the other hand, the number of electrons in the QD is fixed due to the Coulomb blockade effect. When $I_{\rm dot}$ is completely pinched off in the Coulomb blockade regime, the electron number can be controlled precisely by tuning the gate voltage.

can tunnel via those energy levels. In the following, transport through the QD is categorized into two regimes, depending on the size of the bias window: the low-bias regime, where $|eV_{\rm SD}| \ll E_{\rm C}, \Delta E$ and the high-bias regime, where $|eV_{\rm SD}| > E_{\rm C}$ and/or ΔE.

2.1.2 Coulomb Oscillation

In the low-bias regime at most one level can contribute to the transport. Tunneling is only allowed when an electrochemical potential $\mu(N)$ is in the bias window, i.e. $\mu_{\rm S} \geq \mu(N) \geq \mu_{\rm D}$. Otherwise electrons cannot tunnel through the QD and the number of electrons in the QD is fixed. This is known as Coulomb blockade (Fig. 2.2(a)). Coulomb blockade can be lifted by aligning an electrochemical potential $\mu(N)$ within the bias window, by sweeping the gate voltage. In such configuration, the number of electrons can be both $N-1$ and N, and the current through the QD, $I_{\rm dot}$, shows a peak, which is called the *Coulomb*

peak. Since only one electron can tunnel at a time, QDs are sometimes referred to as *single electron transistors* (SETs). A characteristic oscillatory pattern of I_{dot} as the gate voltage is swept is a common observation in QD transport and is called Coulomb oscillation (Fig. 2.2(c)).

Since μ_{S} and μ_{D} are fixed, $\mu(N, V_{\mathrm{G}}) = \mu(N+1, V_{\mathrm{G}} + \Delta V_{\mathrm{G}})$, with ΔV_{G} denoting the Coulomb peak separation. Together with Eqs. (2.2) and (2.3), E_{add} is shown to be proportional to ΔV_G. Indeed, $\Delta V_{\mathrm{G}} = \frac{C}{eC_{\mathrm{G}}} E_{\mathrm{add}}(N) = \frac{\alpha}{e} E_{\mathrm{add}}(N)$, with α the so-called α-factor defined by C/C_{G}.

2.1.3 Coulomb Diamonds

In the high-bias regime where $|eV_{\mathrm{SD}}| > E_{\mathrm{C}}$ and/or ΔE, the bias window is large enough for multiple levels to participate in the electron transport. To discuss QD transport when excited states are involved, the electrochemical potential, so far limited to transitions between ground states, needs to be generalized. The electrochemical potential for the transition between an $(N-1)$-electron state $|a\rangle$ and an N-electron state $|b\rangle$ can be defined as

$$\mu_{a \leftrightarrow b} = U_b(N) - U_a(N-1), \tag{2.4}$$

where $U_a(N-1)$ and $U_b(N)$ represent the total energies of a QD in the states $|a\rangle$ and $|b\rangle$, respectively. In the following, we assume for simplicity that the source-drain bias voltage V_{SD} is negative (hence $\mu_{\mathrm{S}} > \mu_{\mathrm{D}}$), and the drain reservoir is grounded ($\mu_{\mathrm{D}} = 0$).

As V_{SD} becomes more negative, μ_{S} increases since $\mu_{\mathrm{S}} = -eV_{\mathrm{SD}}$, and the bias window becomes wider. When $|eV_{\mathrm{SD}}| \geq \Delta E$ and both electrochemical potentials for the ground state and excited state are tuned in the bias window, more than one tunnel paths contribute to the transport (Fig. 2.3(a)). In general, increase in the number of QD transport paths results in changes in I_{dot}, with the amount depending on the tunnel couplings of the levels involved with the reservoirs. By further increasing $|V_{\mathrm{SD}}|$, the electrochemical potential for the next ground state also enters the bias window for $|eV_{\mathrm{SD}}| \geq E_{\mathrm{add}}$ (Fig. 2.3(b)). In such a situation, double-electron tunneling occurs and the electron number fluctuates between $N-1$, N, and $N+1$.

Multi-path transport in the high-bias regime allows excited-state spectro-

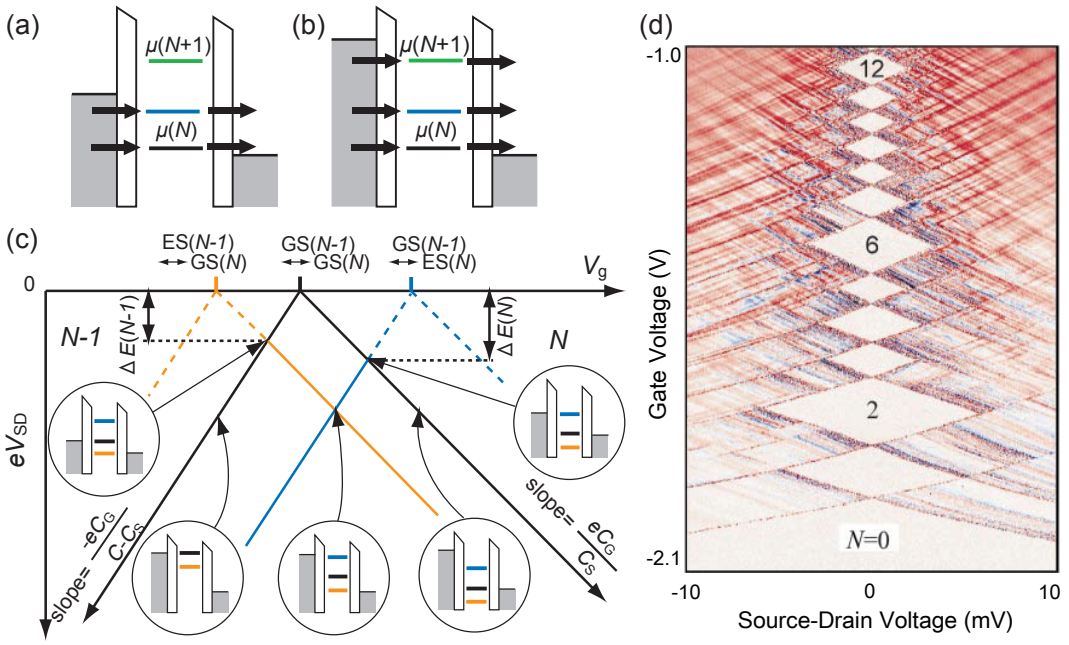

Figure 2.3: QD transport in the high bias regime. (a) Multi-path tunneling. Electrons can tunnel through the excited state when $|eV_{\mathrm{SD}}| \geq \Delta E$. The corresponding electrochemical potential is indicated by the blue line. (b) Double-electron tunneling. It can take place when $|eV_{\mathrm{SD}}| \geq E_{\mathrm{add}}$. (c) The map of I_{dot} as a function of V_{G} and eV_{SD}. Here we focus on transitions between the ground states, GS$(N-1)$ and GS(N), and the excited states ES$(N-1)$ and ES(N) of $(N-1)$ and N electrons. Along the line of $V_{\mathrm{SD}} = 0$ Coulomb oscillation is observed (the low-bias regime). The dot current or Coulomb peak is only observed at the V_{G} where the GS$(N-1) \leftrightarrow$ GS(N) transition takes place, and the QD is otherwise in the Coulomb blockade. When finite V_{SD} is applied, the GS$(N-1) \leftrightarrow$ GS(N) transition outlines a V-shaped region where electron tunneling is possible. Outside of the V-shape region the transport through the QD is Coulomb blockaded, since either GS$(N-1)$ or GS(N) is stabilized. Therefore, other transitions involving the excited states are allowed only in this V-shaped region and the differential conductance $\mathrm{d}I_{\mathrm{dot}}/\mathrm{d}V_{\mathrm{SD}}$ become nonzero only on the solid lines. The slopes of the boundaries of the V-shaped region, $\mathrm{d}(-eV_{\mathrm{SD}})/\mathrm{d}V_{\mathrm{G}}$, are determined by the relative capacitances. For $V_{\mathrm{D}} = 0$, they are $-C_{\mathrm{G}}/(C - C_{\mathrm{S}})$ and $+C_{\mathrm{G}}/C_{\mathrm{S}}$. (d) Differential conductance measured in a vertical QD. Typical Coulomb diamond structures are clearly recognized. Unusually large diamonds are observed for $N = 2$, 6, and 12, which correspond to filled shells [22]. Figure is adopted from [2].

scopy. Since I_{dot} changes when a new transport path enters the bias window, the energy spectrum of excited states can be obtained from the differential conductance measurement. For instance, the level-spacing of an excited state can be evaluated by the eV_{SD} where the excited-state transition line intersects with the boundary of the Coulomb blockade region. The dependence of the electrochemical potentials on V_{G} and eV_{SD} is plotted in Fig. 2.3(c). All electrochemical potentials of the relevant transitions can be calculated using Eq. (2.4). If $|V_{\mathrm{SD}}|$ is large enough for multiple electron tunneling, the V-shaped tunneling regions for different charge transitions overlap each other. The Coulomb blockade region therefore forms a diamond shape in the V_{SD}-V_{G} plane, a so-called *Coulomb diamond*. Figure 2.3 shows typical Coulomb diamonds observed with a vertical QD.

2.2 Lateral Quantum Dots

QDs come in various sizes and materials. The kinds of electrically-accessible QDs include "vertical" QDs [22] and "laterally-defined" QDs [23] in a semiconductor heterostructure, "self-assembled" QDs with nano-gap electrodes [24], InAs nanowire QDs [25] and carbon-nanotube QDs [26]. For the research of spin qubits, lateral QDs are widely adopted, since they offer excellent tunability of tunnel couplings and flexibility in the device design that allows integration into a highly-sensitive electrometer.

Lateral QDs are formed in a clean two-dimensional electron gas in a semiconductor heterostructure (Fig. 2.4). In addition to the vertical confinement at the hetero-junction, electrons are laterally confined by the electrostatic potential of the gate electrodes, which are fabricated on the surface of the semiconductor substrate. This device structure makes it relatively straightforward to fabricate multiple QDs by just adding the defining gates. As the number of gate electrodes can be made larger than that of confined QDs, the lateral QD offers high degrees of freedom in the device tuning. For instance, the gates can be used to tune the tunnel couplings by several orders of magnitude, while keeping the electron number fixed. The ability to independently change QD parameters is crucial for electrical spin manipulations. In this section we briefly explain the basics and the important techniques with lateral QDs.

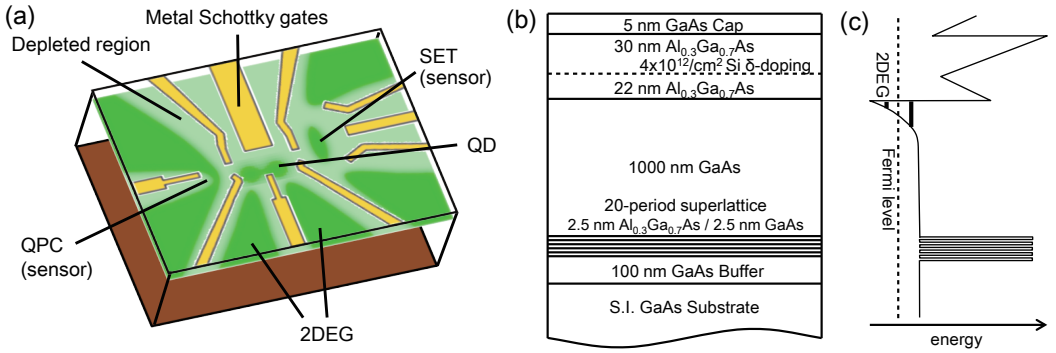

Figure 2.4: Lateral QD and HEMT. (a) Schematic of the lateral QD structure. Lateral QDs are formed in the 2DEG (colored green). Negative voltages on the surface metal Schottky gates (colored yellow) deplete the 2DEG underneath and form the electrostatic potential which traps electrons. Ancillary nanostructures such as a quantum point contact and a single electron transistor can be incorporated as sensors (see §2.2.3). (b) A typical heterostructure of HEMT. The specific parameters are for wafer 090402A that was grown by Hong Lu in the group of A.C. Gossard at U.C. Santa Barbara and is used in the experiments described in Chapters 5, 6 and 7. (c) Schematic of corresponding energy profile of the conduction band. One subband lies below the Fermi level (indicated by the dashed line) in the triangle well and forms the 2DEG at low temperatures.

2.2.1 High Electron Mobility Transistor and Two-Dimensional Electron Gas

Developments in ultra-thin film growth by molecular beam epitaxy have enabled fabrication of quantum wells and heterojunctions with an atomically flat interface between two layers of semiconductors with dissimilar lattice constants [27]. Such heterostructures can be designed to host a two-dimensional electron gas (2DEG), where the electron momentum in the growth direction is quantized by strong confinement in the thin conduction layer formed at the junction.

In the high electron mobility transistor (HEMT) [28], donor electrons are confined in the steep triangular well in the conduction band, formed as a result of the band gap discontinuity at the heterointerface (Figs. 2.4(b),(c)). The doped layer is spatially separated from the 2DEG to suppress electron scattering by the ionized donors, the dominant scattering mechanism at low temperatures. The electron mobility of the HEMT 2DEG can be very high, typically 10^6 cm^2/Vs at liquid Helium temperature. HEMTs with highest mobility are based on a modulation doped heterostructure of GaAs/n-$Al_xGa_{1-x}As$, an alloy between GaAs and AlAs with a larger band gap than GaAs, owing partially to the small lattice mismatch between GaAs and AlAs. Due to suppressed scattering in the HEMT, electron transport is ballistic even on sub-micrometer scales at cryogenic temperatures, making the HEMT an appealing platform for those experiments in low-dimensional electron systems in which ballisticity is important.

2.2.2 Quantum Point Contacts

To fabricate nano-structures in the 2DEG, further confinement of carriers in the lateral directions is necessary. To this end, metal gates with Schottky barriers can be used to locally change the electric potential. The Schottky barrier is a current-rectifying junction formed at the metal-semiconductor interface, with appropriate choices of metal and semiconductor materials. The 2DEG regions beneath the gates can be depleted by application of sufficiently negative voltages on the Schottky gates. This gives *in-situ* tunability of confinement of the electrons in the 2DEG in the lateral directions. The 2DEG can be elec-

trically contacted, on the other hand, by an Ohmic contact, another type of metal-semiconductor interface with no current rectification. For GaAs-based heterostructures, an Ohmic contact can be made, for example, through a mixture of Au and Ge that diffuses to the 2DEG by thermally annealing.

The simplest example of gate defined structures is a quantum point contact (QPC), a quantum one-dimensional channel that is short enough to regard the constriction as a point. A QPC can be formed in the 2DEG by negatively biasing a pair of Schottky gates to deplete regions on two sides of a narrow channel [29]. The conductance G through a QPC is quantized, and described by the one-dimensional Landauer formula without scattering, $G = Ne^2/h$, where N is the number of the occupied one-dimensional subbands [30].

2.2.3 Charge Sensing Techniques

The conductance through a QPC changes drastically from one plateau to the next when the number of the subbands in the bias window is changed one by one. When the gate voltage is tuned at the steep slope between the plateaus, the QPC conductance becomes highly sensitive to the electrostatic environment including arrangement of electrons trapped nearby. In lateral QDs, it is possible to place QPCs in the vicinity of a QD. This enables the measurement of the charge occupation in a QD from the conductance through an adjacent QPC. The change of electron number configuration in a QD modifies the electrochemical potential in the QPC channel, which is detected as a step-like rise in the QPC current or a kink in the current derivative. This charge sensing technique is especially useful when I_{dot} is too small to detect on a realistic timescale, as is often the case with the few-electron multiple QDs.

A proximal SET can be used in place of a QPC for detecting the QD electron number, since the only necessary ingredient is the susceptibility to the surrounding electrostatic potential. Indeed, an SET tuned at the slope of a Coulomb peak has more than an order of magnitude higher sensitivity to the charge rearrangement in the QD [31].

2.3 Charge Stability Diagrams of Double and Triple Quantum Dots

A *charge stability diagram* plots a map of the equilibrium number of electrons in multiple QDs in gate-voltage space. It offers a very powerful tool to understand the electron states in multiple QDs and to identify the regime of interest in the experiments. This section explains the charge stability diagrams of double and triple QDs.

2.3.1 Charge Configuration in a Double Quantum Dot

A double quantum dot (DQD) is a QD array that consists of two single QDs coupled to each other. It is a minimal QD system where inter-dot electron correlations play essential roles.

Charge configuration in a DQD can be fully specified by (N_1, N_2), with $N_{1(2)}$ denoting the number of electrons in QD1(2). Under realistic experimental conditions, the stability diagram of a DQD shows a characteristic *honeycomb* structure, with each hexagon representing a gate-voltage region where the DQD charge configuration is unchanged (Fig. 2.5). Nodes of hexagons are the *triple points*, where three different charge states are energetically degenerate. Since tunneling through a series-coupled DQD involves three charge states, the current is only observed near triple points. In contrast, all charge transition lines are visible in charge sensing measurements as they are sensitive to any change in charge configuration including inter-dot charge exchanges such as $(N+1, M) \leftrightarrow (N, M+1)$.

To investigate the electron states near the triple points in more detail, we apply the CI model to DQDs [32] in a manner similar to §2.1.1. Suppose QD1 and QD2 of a series-coupled DQD are connected to the source and the drain, respectively. The electrochemical potential of QD1, $\mu_1(N_1, N_2) \equiv U(N_1, N_2) - U(N_1 - 1, N_2)$ is given by

$$\begin{aligned} \mu_1(N_1, N_2) &= \left(N_1 - \frac{1}{2}\right) E_{C_1} + N_2 E_{C_m} - \frac{E_{C_1}}{e}(C_S V_S + C_{11} V_{G1} + C_{12} V_{G2}) \\ &\quad + \frac{E_{C_m}}{e}(C_D V_D + C_{22} V_{G2} + C_{21} V_{G1}), \end{aligned} \tag{2.5}$$

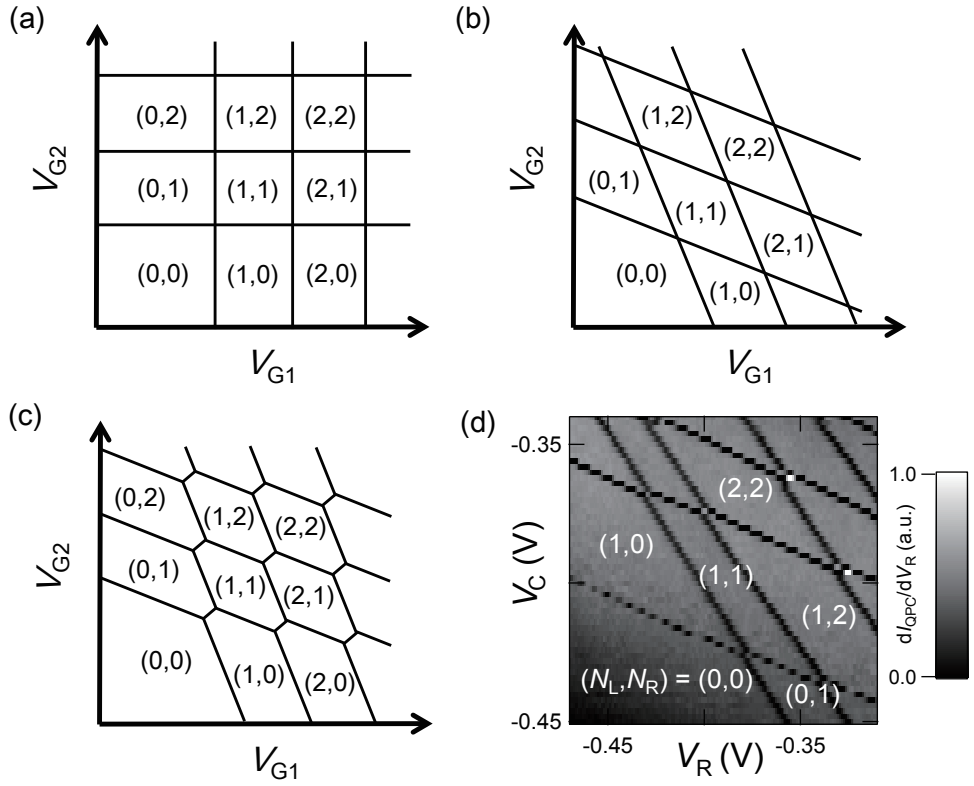

Figure 2.5: DQD stability diagram. (a)-(c) Schematics of charge stability diagrams in a DQD. In (a), QD1 and QD2 are not capacitively coupled to each other, and two gates, G1 and G2, are capacitively coupled to QD1 and QD2, respectively with no cross-coupling between G1(2) and QD2(1). $N_{1(2)}$ is solely determined by the gate voltage $V_{G1(2)}$ as in the single QD case and the charge transition lines are either completely vertical or completely horizontal in the V_{G1}-V_{G2} plane. In (b), cross-capacitive couplings between G1(2) and QD2(1) are taken into account. In (c), the effect of interdot capacitance is further included. Each intersection of charge transition lines in (a) and (b), where four charge states are energetically degenerate, splits into two triple points, whose separation is determined by the capacitive coupling strength between the two QDs. Obtained honeycomb stability diagram well approximates the experimental observation. (d) Measured DQD stability diagram. Plotted is a derivative of current through a proximal QPC as a function of gate voltage. $N_{L(R)}$ is the number of electrons in the left (right) QDs. In the lower left region dark charge transition lines are absent, indicating that the DQD is completely empty. At close inspection inter-dot charge transitions can be seen as bright lines between triple points.

where C_{ij} represents the capacitance between the gate Gj and QDi, and $C_{\mathrm{S}}(C_{\mathrm{D}})$ the capacitance between QD1(2) and the source (drain) reservoir, respectively. E_{C_i} is the charging energy of QDi, and $E_{C_{\mathrm{m}}}$ is the capacitive coupling energy between two QDs and corresponds to the change in the electrochemical potential of a QD when an electron is added to the other QD. The electrochemical potential of QD2, $\mu_2(N_1, N_2)$, is also obtained by interchanging 1 with 2, and $C_{\mathrm{D}}V_{\mathrm{D}}$ with $C_{\mathrm{S}}V_{\mathrm{S}}$ in Eq. (2.5). In the following, two different regimes of DQD transport are separately discussed: the linear transport regime ($|eV_{\mathrm{SD}}| \ll E_{\mathrm{C}}, \Delta E$) and the nonlinear transport regime ($|eV_{\mathrm{SD}}| > E_{\mathrm{C}}$ and/or ΔE).

2.3.1.1 Linear Transport Regime

Figure 2.6(a) shows the charge stability diagram near a pair of neighboring triple points in the linear transport regime. When the inter-dot tunnel coupling t_{c} is much smaller than the inter-dot capacitive coupling, the DQD is in the *weak-coupling* regime, and charge transition lines are observed exactly where the two lowest electrochemical potentials become degenerate.

If the DQD is in the *strong-coupling* regime and the tunnel coupling is not negligible, electrons are not fully localized in either QD. Rather, they occupy the molecular orbitals which distribute over the entire DQD. The bonding and anti-bonding orbitals are superposition states of the single-QD orbitals localized in either QD1 or QD2. Due to hybridization, when the single-QD states of both QDs are aligned, the bonding orbital is lower in energy by $|t_{\mathrm{c}}|$ than the single-QD orbitals, while the anti-bonding orbital is higher by the same amount. The effect of tunnel coupling is suppressed as the energy detuning between the two localized states becomes large as compared to $|t_{\mathrm{c}}|$. This hybridization bends honeycomb lines as depicted in the dashed lines in Fig. 2.6(a).

2.3.1.2 Nonlinear Transport Regime

When the source-drain bias voltage is increased, two different tunneling processes can take place: elastic and inelastic tunneling. In the elastic tunneling process, the initial and final electronic states have the same energy. In contrast, in the inelastic tunneling process, there is an energy mismatch between the initial and final states, which must be compensated by e.g. phonons and photons

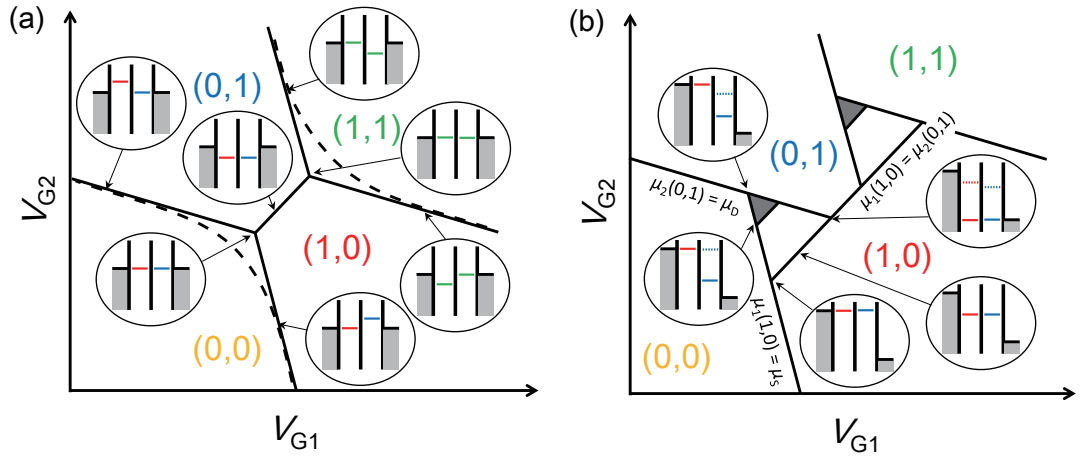

Figure 2.6: Triple points and bias triangles. (a) Triple points in the DQD stability diagram in the linear transport regime. Each line plots the gate voltages at which the DQD electrochemical potential crosses that of the reservoirs. Solid lines are for the weak tunnel coupling case and dashed lines are for the strong tunnel coupling case. Encircled insets show the energy level diagrams at the indicated positions. (b) Bias triangles in the DQD stability diagram in the nonlinear transport regime. When the source-drain bias V_{SD} is applied across the DQD, each triple point evolves into a bias triangle (enclosed with black lines), in which charge transport through the dot is energetically allowed. Out of the triangles the transport is Coulomb blockaded. Here the source-drain bias is negatively applied ($V_{\mathrm{SD}} < 0$), so that the electrochemical potential of the source μ_{S} is higher than that of the drain μ_{D}. In the left bias triangle, electron transport cycle, $(0,0) \rightarrow (1,0) \rightarrow (0,1) \rightarrow (0,0)$, takes place, whereas in the right bias triangle, transport is by the hole cycle, $(1,1) \rightarrow (1,0) \rightarrow (0,1) \rightarrow (1,1)$. Dark gray regions inside the bias triangles indicate where excited states are involved in transport.

for energy conservation. Note that inelastic tunneling is a second-order process and the average number of phonons and photons is usually negligibly small at cryogenic temperatures. Still, inelastic tunneling becomes dominant when there are no aligned levels for elastic processes. In semiconductor QDs, the inelastic process is in principle dominantly mediated by the lattice vibration (phonons)[1].

Transport through a DQD is only observed when three different charge states lie within the bias window. While this condition is only met at triple points when $V_{\mathrm{SD}} = 0$, it is satisfied in triangular regions or *bias triangles* in gate-voltage space as $|V_{\mathrm{SD}}|$ is increased and the bias-window opens wider. Figure 2.6(b) draws an example of the bias triangles in the charge stability diagram in the V_{G1}-V_{G2} plane.

In order to see how the bias triangle is formed and to examine the electron transport inside it, it is useful to introduce *(level) detuning* ε as the energy difference between electrochemical potentials μ_1 and μ_2 of localized states. For the moment, for simplicity we focus on the vicinity of the $(0,0)$-$(1,0)$-$(0,1)$ charge transition and assume the source-drain bias is applied such that the electrochemical potential of the left lead (source) is higher than that of the right lead (drain). The bottom line of the bias triangle which runs parallel to the $(0,1)$-$(1,0)$ boundary is the *zero-detuning line*, on which $\varepsilon = 0$ (i.e. $\mu_1(1,0) = \mu_2(0,1)$). As we go away from the zero-detuning line toward the $(0,1)$ region, the detuning $\varepsilon(= \mu_1(1,0) - \mu_2(0,1))$ becomes larger. If we move parallel to the zero-detuning line in the stability diagram, all chemical potentials of $(1,0)$ and $(0,1)$ states shift by the same amount and ε is fixed. When $\varepsilon \geq |eV_{\mathrm{SD}}|$ the condition of $\mu_{\mathrm{S}} \geq \mu_1(1,0) \geq \mu_2(0,1) \geq \mu_{\mathrm{D}}$ is not fulfilled in any region so the bias triangle is closed at $\varepsilon = |eV_{\mathrm{SD}}|$.

Transport current and time-averaged charge configuration are not constant within the bias triangle. Stripes are often observed which run parallel to the zero-detuning line. Since they originate from elastic transport through excited states, measuring these stripes, in either transport currents or charge sensing signals, allows the energy-level spectroscopy. This bias spectroscopy is a powerful tool, as it also yields the energy scales such as charging energies, energy level

[1] An important exception is when QDs are irradiated with microwaves. Then the emission and absorption of photons are enhanced, leading to *photon-assisted tunneling* (PAT) [33].

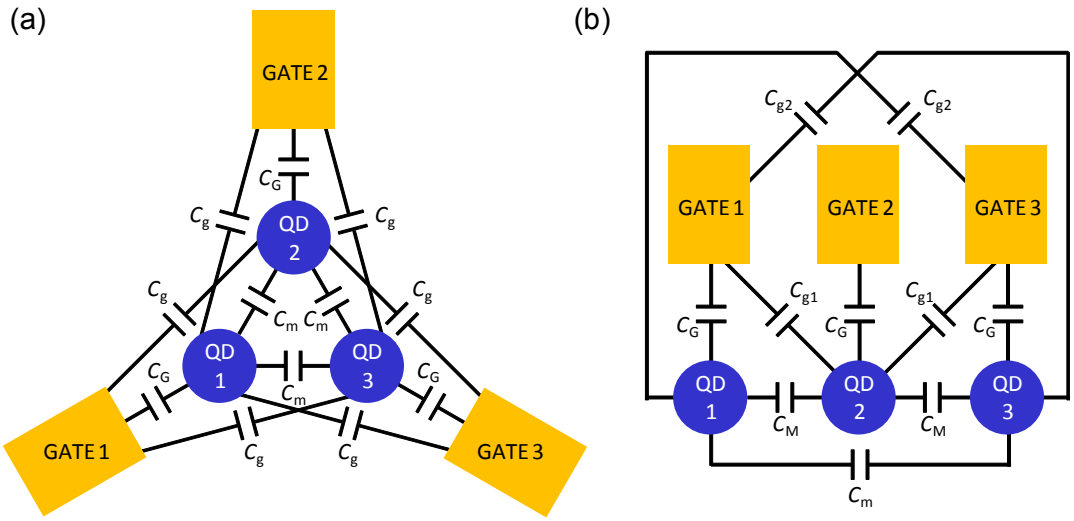

Figure 2.7: Two representative TQD geometries. (a) In the fully symmetric case three QDs form a triangle. (b) In the mirror-symmetric case they form a one-dimensional array.

spacings and electrostatic or tunnel coupling strengths. However, the visibility of the stripes strongly depends on relative tunnel couplings and interaction strengths, necessitating fine-tuning of the QD parameters.

2.3.2 Charge Configuration in a Triple Quantum Dot

A triple QD (TQD) is a set of three coupled QDs. Unlike a DQD, a TQD has a degree of freedom in the relative inter-dot capacitive couplings; relative inter-dot capacitances, and thus the stability diagrams are strongly affected by how the three QDs are arranged (Fig. 2.7). Here only a series-coupled TQD is considered, due to the ease of experimental realization. For simplicity, we further assume that the capacitive couplings are symmetric against interchange of 1 and 3 (Fig. 2.7(b)).

2.3.2.1 Electrostatic Energy of a Triple Quantum Dot

The CI model introduced in §2.1.1 describes the electrostatic energy of the TQD states well enough to reproduce the stability diagrams observed experi-

mentally [34, 35]. The total charge in the i-th QD, Q_i, is given by

$$Q_i = eN_i = \sum_j C_{ij}(V_i - V_{\mathrm{G}j}) + \sum_{j \neq i} C_{\mathrm{m}ij}(V_i - V_j), \tag{2.6}$$

where N_i, V_i and $V_{\mathrm{G}j}$ represent the electron number and the electrical potential of the i-th QD and the gate voltage of the j-th electrode, respectively. C_{ij} is the capacitance between the i-th QD and the j-th electrode, $C_{\mathrm{m}ij}$ the interdot capacitance between the i-th and the j-th QD . Note that in general $C_{\mathrm{m}ij} = C_{\mathrm{m}ji}$. Equation (2.6) forms a system of simultaneous equations with three variables $\vec{Q} = \mathbf{C}\vec{V}_{\mathrm{QD}}$:

$$\begin{pmatrix} Q_1 + \sum_i C_{1i}V_{\mathrm{G}i} \\ Q_2 + \sum_i C_{2i}V_{\mathrm{G}i} \\ Q_3 + \sum_i C_{3i}V_{\mathrm{G}i} \end{pmatrix} = \begin{pmatrix} C_1 & -C_{\mathrm{m}12} & -C_{\mathrm{m}13} \\ -C_{\mathrm{m}21} & C_2 & -C_{\mathrm{m}23} \\ -C_{\mathrm{m}31} & -C_{\mathrm{m}32} & C_3 \end{pmatrix} \begin{pmatrix} V_1 \\ V_2 \\ V_3 \end{pmatrix}, \tag{2.7}$$

with $C_i = \sum_j C_{ij} + \sum_{j \neq i} C_{\mathrm{m}ij}$. $\mathbf{C}$ is simplified in the mirror-symmetric TQD[2] as

$$\mathbf{C} = \begin{pmatrix} C_1 & -C_{\mathrm{M}} & -C_{\mathrm{m}} \\ -C_{\mathrm{M}} & C_2 & -C_{\mathrm{M}} \\ -C_{\mathrm{m}} & -C_{\mathrm{M}} & C_3 \end{pmatrix}. \tag{2.8}$$

The total energy of a TQD can then be written by $U(N_1, N_2, N_3, V_1, V_2, V_3) = \frac{1}{2}\vec{Q} \cdot \vec{V}_{\mathrm{QD}} = \frac{1}{2}\vec{Q} \cdot \mathbf{C}^{-1}\vec{Q}$ and the electrochemical potential in the i-th QD is $\mu_i(N_1, N_2, N_3, V_1, V_2, V_3) = U(N_i + 1) - U(N_i)$.

Stability diagrams plot the Coulomb blockade regions with fixed equilibrium numbers of trapped electrons. The condition for Coulomb blockade in a TQD is that no electron exchange is allowed with the reservoirs or among the QDs. The condition that no extra electron is exchanged with the leads is expressed

[2] Due to symmetry, $C_{\mathrm{G}} = C_{11} = C_{22} = C_{33}$, $C_{\mathrm{g}1} = C_{12} = C_{21} = C_{23} = C_{32}$, $C_{\mathrm{g}2} = C_{13} = C_{31}$, $C_{\mathrm{M}} = C_{\mathrm{m}12} = C_{\mathrm{m}21} = C_{\mathrm{m}23} = C_{\mathrm{m}32}$ and $C_{\mathrm{m}} = C_{\mathrm{m}13} = C_{\mathrm{m}31}$. Therefore $C_1 = C_3 = C_{\mathrm{G}} + C_{\mathrm{g}1} + C_{\mathrm{g}2} + C_{\mathrm{M}} + C_{\mathrm{m}}$ and $C_2 = C_{\mathrm{G}} + 2C_{\mathrm{g}1} + 2C_{\mathrm{M}}$. See Fig. 2.7(b) for visual description.

by a set of inequalities such as[3]

$$\mu_1(N_1, N_2, N_3, V_1, V_2, V_3) \leq 0 \leq \mu_1(N_1 + 1, N_2, N_3, V_1, V_2, V_3),$$

where the electrochemical potentials of the reservoirs are assumed to be in the low-bias regime and ~ 0. The other condition that no intra-TQD transition is allowed is expressed by a set of inequalities such as[4]

$$\mu_1(N_1, N_2, N_3, V_1, V_2, V_3) \leq \mu_2(N_1 - 1, N_2 + 1, N_3, V_1, V_2, V_3),$$
$$\mu_2(N_1, N_2, N_3, V_1, V_2, V_3) \leq \mu_1(N_1 + 1, N_2 - 1, N_3, V_1, V_2, V_3).$$

The Coulomb blockade regions where all the above conditions are met in the gate-voltage space can be numerically calculated for various choices of (N_1, N_2, N_3), given the form of TQD electrochemical potentials. Figure 2.8 shows charge stability diagrams simulated in this manner around the electron numbers $(0, 0, 0)$-$(1, 1, 1)$.

2.3.2.2 Elastic Transport Through a Two-Terminal Triple Quantum Dot

Charge transfer behavior in a multiple QD can be complex as its energy levels become dense and complicated. The charge configuration map of a TQD is essentially three dimensional, making it much less common for level alignment to occur in two dimensional slices of the stability diagram [34, 36, 37]. Fine pa-

[3] To be specific, the other inequalities are as follows:

$$\mu_2(N_1, N_2, N_3, V_1, V_2, V_3) \leq 0 \leq \mu_2(N_1, N_2 + 1, N_3, V_1, V_2, V_3),$$
$$\mu_3(N_1, N_2, N_3, V_1, V_2, V_3) \leq 0 \leq \mu_3(N_1, N_2, N_3 + 1, V_1, V_2, V_3).$$

[4] The other inequalities that prohibit transitions between QD2 and QD3 and between QD1 and QD3 are given as follows:

$$\mu_2(N_1, N_2, N_3, V_1, V_2, V_3) \leq \mu_3(N_1, N_2 - 1, N_3 + 1, V_1, V_2, V_3),$$
$$\mu_3(N_1, N_2, N_3, V_1, V_2, V_3) \leq \mu_1(N_1 + 1, N_2, N_3 - 1, V_1, V_2, V_3),$$
$$\mu_1(N_1, N_2, N_3, V_1, V_2, V_3) \leq \mu_3(N_1 - 1, N_2, N_3 + 1, V_1, V_2, V_3),$$
$$\mu_3(N_1, N_2, N_3, V_1, V_2, V_3) \leq \mu_2(N_1, N_2 + 1, N_3 - 1, V_1, V_2, V_3).$$

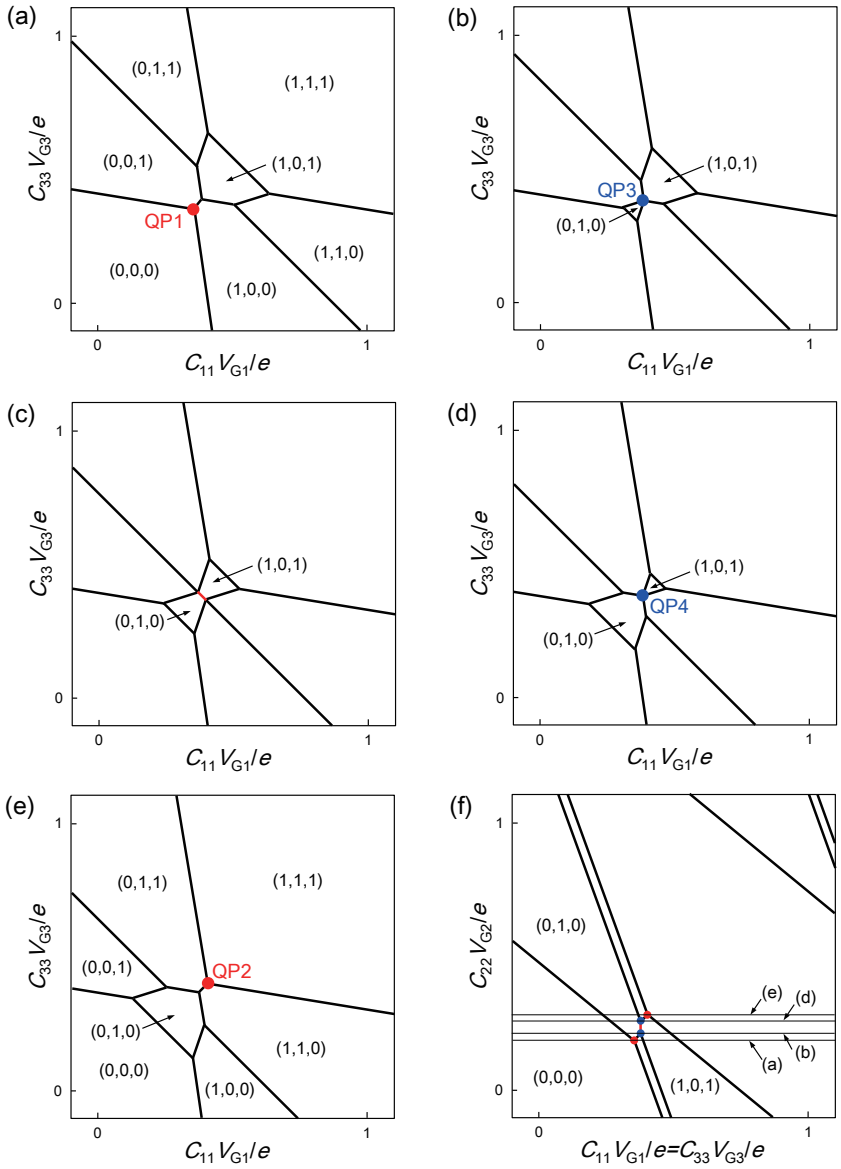

Figure 2.8: Numerically calculated charge stability diagrams of the mirror-symmetric TQD. Each gate voltage V_{Gi} is normalized by e/C_{ii}. Calculated for $C_G = 20C_m$ and $C_g = 5C_m$. Diagrams (a)-(e) are plotted as a function of V_{G_1} and V_{G_3} for different V_{G_2}. Diagram (f) gives a map when V_{G1} and V_{G3} are changed simultaneously and symmetrically while V_{G2} is swept continuously. Four quadruple points are indicated in (a), (b), (d) and (e). Figures are adopted from [35].

rameter tuning is thus required to observe finite currents through TQD devices contacted with leads at both ends[5].

A TQD analogue to a triple point in DQDs is a *quadruple point*, where four TQD electronic configurations are degenerate. In Figs. 2.8(a), (b), (d) and (e), four quadruple points QP1 to QP4 are recognized. At these quadruple points, one-by-one electron tunneling is allowed[6]. Along the red solid lines in Figs. 2.8(c) and (f), the regions of the charge states $(0,1,0)$ and $(1,0,1)$ sit next to each other. There the charge transition between these states can be caused by the quantum cellular automata (QCA) co-tunneling processes [39], in which an electron entering QD1(3) kicks the QD2 electron to QD3(1). Since this QCA process involves a change in the total electron number, an effective current is observed through the TQD. Therefore, transport currents can flow at four quadruple points and on the QCA line in the charge stability diagrams [34,37].

[5]It is experimentally possible to fabricate and measure three-terminal TQDs. Such devices can be seen as a pair of DQDs in primary approximation and the condition to observe transport currents is much less severe [35, 38].

[6]The tunneling sequence at each quadruple point is as follows:

$$\begin{aligned}
\text{QP1} &: (0,0,0) \longleftrightarrow (1,0,0) \longleftrightarrow (0,1,0) \longleftrightarrow (0,0,1) \\
\text{QP2} &: (0,1,1) \longleftrightarrow (1,0,1) \longleftrightarrow (1,1,0) \longleftrightarrow (1,1,1) \\
\text{QP3} &: (1,0,0) \longleftrightarrow (0,1,0) \longleftrightarrow (0,0,1) \longleftrightarrow (1,0,1) \\
\text{QP4} &: (1,1,0) \longleftrightarrow (1,0,1) \longleftrightarrow (0,1,1) \longleftrightarrow (0,1,0).
\end{aligned}$$

Chapter 3

Spin Qubits in Quantum Dots

Electron spins are the canonical example of a quantum mechanical two-level system. They are promising candidates for qubits, because the spin is not strongly affected by the environment and the charge degree of freedom offers electrical knobs for manipulating the spin system [40–42]. Coherent operation of single electron spins in QDs has been intensively studied since the seminal proposal of QD-based quantum computers [6]. Three implementations of QD-based spin computers, single-spin, two-spin and three-spin qubits[1], have been realized experimentally since then [17, 45, 46].

This chapter reviews the main achievements in the field of quantum computing with QD spins, with a primary focus on single-spin qubits, the simplest implementation. Preceding experiments demonstrating prerequisites for quantum computing [12] are partially reviewed, including the initialization and readout of single spins, single-qubit operations, control of two-qubit entanglement and measurement of coherence times.

3.1 Spin States in Quantum Dots

Understanding energy levels of spin states is essential to initialize, readout and control single spins electrically. Here we theoretically discuss the spin states

[1] In the community jargon, these implementations, proposed independently [6, 43, 44], are named Loss-DiVincenzo (LD), singlet-triplet (ST) and exchange-only (EO) qubits, respectively.

in an array of singly-occupied QDs, which are particularly useful to implement qubits.

3.1.1 Single-Electron Spin States

In non-magnetic semiconductors, spins interact only weakly and are treated as non-interacting, independent quantum systems to first-order approximation. However, the Landé g-factor deviates considerably from that of the free electron (≈ 2) due mainly to enhanced spin-orbit interaction [47]. Confinement in a QD can further modify the effective g-factor [48]. The Zeeman Hamiltonian of a single spin in a QD under a magnetic field $\boldsymbol{B}$ is then simply given by

$$\mathcal{H}_{\text{lab, Z}} = \frac{g\mu_{\text{B}}}{2}\boldsymbol{B}\cdot\boldsymbol{\sigma}, \tag{3.1}$$

with g, the Landé g-factor, as a parameter, where μ_{B} is the Bohr magneton and σ_i are the Pauli matrices. Up and down spin eigenstates, aligned to the direction of $\boldsymbol{B}$, are split by the Zeeman energy $E_{\text{Z}} = |g|\mu_{\text{B}}|\boldsymbol{B}|$. In the laboratory frame the spin precesses at the Larmor frequency $f_{\text{L}} = |g|\mu_{\text{B}}|\boldsymbol{B}|/h$, with Planck's constant h.

To define qubits, it is convenient to take a reference frame rotating at an angular frequency $\omega \sim \omega_{\text{L}}(= 2\pi f_{\text{L}})$. A superposition spin state $|\varphi\rangle_{\text{ref}}$ in the rotating frame can be expressed as $|\varphi\rangle_{\text{ref}} = \exp\left(\frac{i\omega t}{2}\sigma_z\right)|\varphi\rangle_{\text{lab}}$, where σ_z is the Pauli z matrix and $|\varphi\rangle_{\text{lab}}$ is the spin state in the laboratory frame. By simply substituting for $|\varphi\rangle_{\text{lab}}$ in the Schrödinger equation in the original frame, the Hamiltonian that describes the time evolution in the reference frame is obtained as,

$$\mathcal{H}_{\text{ref}} = \mathrm{e}^{\frac{i\omega t}{2}\sigma_z}\mathcal{H}_{\text{lab}}\mathrm{e}^{-\frac{i\omega t}{2}\sigma_z} - \frac{\hbar\omega}{2}\sigma_z. \tag{3.2}$$

Notably when $\omega = \omega_{\text{L}}$, $\mathcal{H}_{\text{ref}} = 0$ in the reference frame, and the spin is at rest. Figure 3.1 shows the Bloch sphere of a single spin, a graphical representation of the state of the two level system, in the original and reference frames [9].

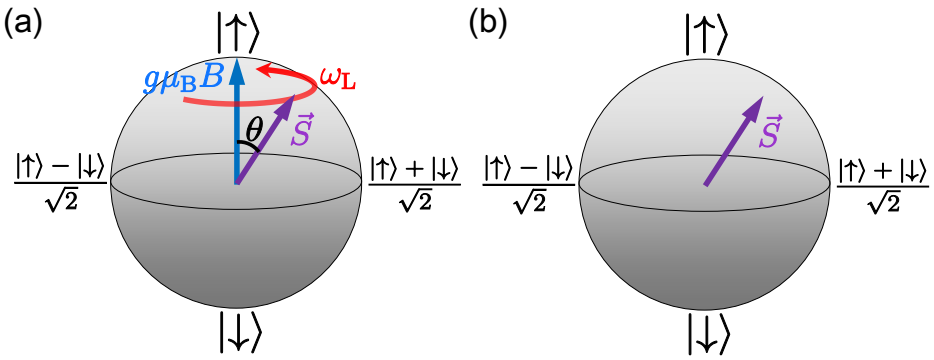

Figure 3.1: The Bloch sphere of a single spin. A pure spin state can be represented by a Bloch vector pointing to the surface of the sphere. The inclination from the z-axis θ is determined such that the up-spin probability $P_{|\uparrow\rangle} = \cos^2\theta$, while the azimuthal angle, as for a pure spin state, corresponds to the relative phase of up- and down-spin states. The direction of the field is taken as z. (a) In the laboratory frame, the spin precesses under a magnetic field. (b) In the reference frame rotating at the spin precession frequency, spin appears static.

3.1.2 Two-Electron Spin States

Understanding two-electron spin states and interactions between single spins are essential for entanglement control and two-qubit operation. Since spins are not coupled to electric fields directly, electrical control of spin-spin interactions is only possible when they are correlated with the charge degrees of freedom. Such correlation is strongly enhanced at the charge degeneracy of $(1,1)$-$(2,0)$ (or equivalently $(1,1)$-$(0,2)$) in a DQD [17,49]. It is therefore crucial to understand energy levels away from the $(1,1)$ Coulomb blockade regime, where two qubits are well encoded.

To discuss spin states in the vicinity of $(1,1)$-$(2,0)$ transition, it is convenient to introduce the *level detuning*, ε, as the difference of electrical potentials between QD1 and QD2 (Fig. 3.2(a)). When ε is sufficiently large to stabilize the $(2,0)$ charge occupancies, the ground state becomes the singlet, $|\mathrm{S}_{(2,0)}\rangle = \left(|\uparrow_1\downarrow_1\rangle - |\downarrow_1\uparrow_1\rangle\right)/\sqrt{2}$, since Pauli's exclusion forces symmetric spins to occupy different orbitals in QD1. The localized singlet-triplet energy difference, E_{ST}, is typically much larger than the interdot tunnel coupling, t_c, and the level detunings of interest. Given that the tunneling process preserves

spin, hybridization with $(2,0)$ states is exclusively allowed for the singlet[2], $|\mathrm{S}\rangle = \left(|\uparrow_1\downarrow_2\rangle - |\downarrow_1\uparrow_2\rangle\right)/\sqrt{2}$. The Hamiltonian that describes the tunnel coupling is then given by

$$\mathcal{H}_\mathrm{T} = -\varepsilon\,|\mathrm{S}_{(2,0)}\rangle\langle\mathrm{S}_{(2,0)}| + \sqrt{2}t_\mathrm{c}\left(|\mathrm{S}_{(2,0)}\rangle\langle\mathrm{S}| + |\mathrm{S}\rangle\langle\mathrm{S}_{(2,0)}|\right). \tag{3.3}$$

At negative detunings, the virtual tunneling to $|\mathrm{S}_{(2,0)}\rangle$ lowers the energy of $|\mathrm{S}\rangle$ by the effective exchange energy J. From Eq. (3.3),

$$J(\varepsilon) = \sqrt{\varepsilon^2 + 8{t_\mathrm{c}}^2}. \tag{3.4}$$

When the levels are sufficiently detuned ($\varepsilon \ll t_\mathrm{c}$), the admixture with $|\mathrm{S}_{(2,0)}\rangle$ is suppressed and Eq. (3.3) simplifies to the Heisenberg Hamiltonian, $J\vec{S}_1 \cdot \vec{S}_2$.

In the $(1,1)$ Coulomb blockade regime, the effective system Hamiltonian in the laboratory frame is then approximated by

$$\begin{aligned}\mathcal{H} = &-J(\varepsilon)\,|\mathrm{S}\rangle\langle\mathrm{S}| + \Delta_\mathrm{Z}\left(|\uparrow_1\downarrow_2\rangle\langle\uparrow_1\downarrow_2| - |\downarrow_1\uparrow_2\rangle\langle\downarrow_1\uparrow_2|\right)\\ &+E_{\mathrm{Z},0}\left(|\mathrm{T}_+\rangle\langle\mathrm{T}_+| - |\mathrm{T}_-\rangle\langle\mathrm{T}_-|\right).\end{aligned} \tag{3.5}$$

Here $E_{\mathrm{Z},0}$ is the average Zeeman energy and Δ_Z is the difference in the (local) Zeeman energy between the dots. If the g-factors are the same, $\Delta_\mathrm{Z} = g\mu_\mathrm{B}\Delta B_\mathrm{Z}$, where ΔB_Z is difference of the local magnetic field along the quantization z-axis. $|\mathrm{T}_+\rangle = |\uparrow_1\uparrow_2\rangle$ and $|\mathrm{T}_-\rangle = |\downarrow_1\downarrow_2\rangle$ are the $(1,1)$ triplet states with parallel spins. These triplets with nonzero z-component S_z of the total spin are Zeeman split under sufficiently large magnetic fields to define spin qubits. In the remaining $|\uparrow\downarrow\rangle$-$|\downarrow\uparrow\rangle$ subspace, J and Δ_Z compete with each other (Fig. 3.3).

3.1.3 Three-Electron Spin States

Three spins in a series-coupled singly-occupied TQD are coupled by nearest-neighbor exchange interactions, J_{12} (J_{23}) between QD1(2) and QD2(3). Since they originate from virtual inter-dot tunneling of singlet-like states, J_{12} and J_{23} are enhanced as the TQD is tuned toward the $(2,0,1)$ and $(1,0,2)$ charge state,

[2]Note that the orbital part of the wavefunction is omitted. The singlet and the triplets with $(1,1)$ charge occupancies have different orbital wavefunctions with the opposite symmetry under exchange.

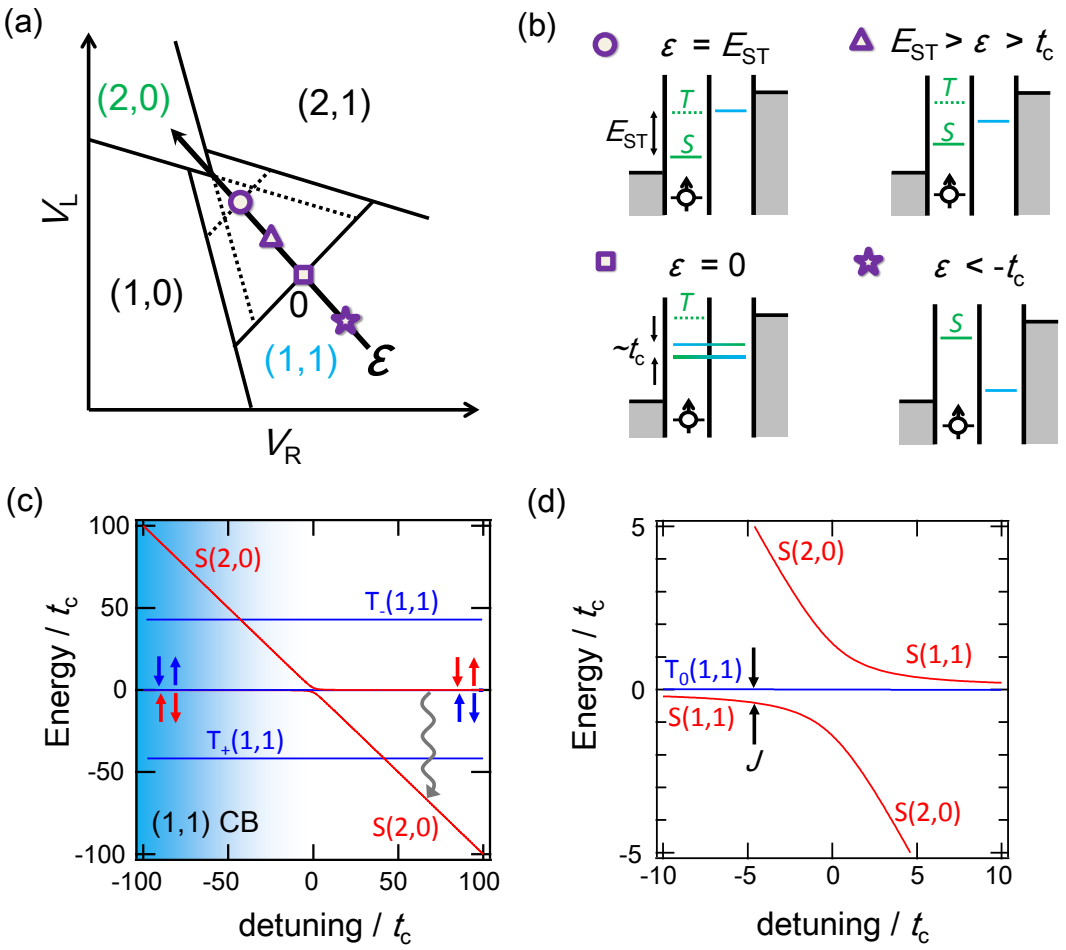

Figure 3.2: Two-electron spin energy levels and the level detuning. (a) DQD stability diagram with a large source-drain bias. The level detuning (ε) axis is indicated in the diagram. (b) Schematics of electrochemical potentials (relative to the $(1,0)$ state) for the $(1,0) \rightarrow (1,1) \rightarrow (2,0)$ transport cycle at various points along the detuning axis indicated in (a). For $\varepsilon \lesssim -t_c$ the $(1,1)$ states are stabilized. For $\varepsilon \gtrsim t_c$ the $(2,0)$ is the lowest level in the bias window. (c) Energy levels as a function of level detuning. Away from the $(1,1)$ charge boundary ($\varepsilon \sim 0$), J approaches 0, so $|\uparrow\downarrow\rangle$ and $|\downarrow\uparrow\rangle$ become eigenstates due to finite interdot difference in the Zeeman energy. The splitting between the triplet states (T_+ and T_-) is equal to twice the Zeeman energy. Note that the sign of $g\mu_B B_0$ is negative here so that the T_+ is lower in energy. (d) Energy levels near zero-detuning. When $\varepsilon = 0$, two singlet states anti-cross, with the size of the splitting equal to $2\sqrt{2}t_c$. Slightly away from $\varepsilon = 0$, the eigenstates are $|S\rangle$ and $|T_0\rangle$. $|S\rangle$ is lower in energy by the exchange interaction, $J(\varepsilon)$.

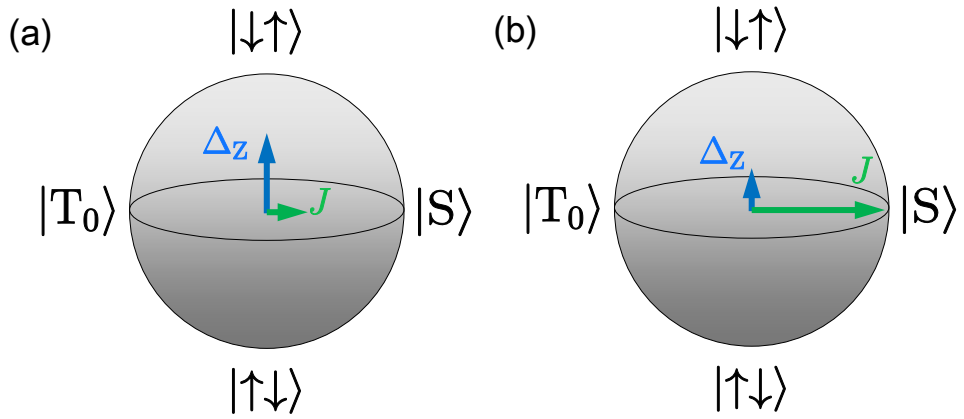

Figure 3.3: Bloch sphere representation of the $S_z = 0$ subspace. (a) When the local Zeeman energy difference (Δ_Z) is much larger than the exchange energy (J), the eigenstates are $|\uparrow\downarrow\rangle$ and $|\downarrow\uparrow\rangle$. (b) In the opposite limit, the eigenstates are $|S\rangle$ and $|T_0\rangle = (|\uparrow_1\downarrow_2\rangle + |\downarrow_1\uparrow_2\rangle)/\sqrt{2}$.

respectively. The eigenstates are four quadruplets[3] with $S = 3/2$, and four doublets[4] with $S = 1/2$, under the same Zeeman energies among QDs [50]. Away from the energy degeneracy points, the biggest correction to these eigenstates of exchange-coupling Hamiltonian comes from the local Zeeman energy differences, $\Delta_{Z,12}$ and $\Delta_{Z,23}$ between QD1(2) and QD2(3), which couple two doublet states and a quadruplet state with the same spin projection S_z [46, 51, 52]. In the middle of the $(1, 1, 1)$ Coulomb blockade region where J_{12} and J_{23} are sup-

[3]Explicitly, the four quadruplets $|Q_{S_z}\rangle$ are

$$\begin{aligned}
|Q_{+3/2}\rangle &= |\uparrow\uparrow\uparrow\rangle\,, \\
|Q_{+1/2}\rangle &= |\uparrow\uparrow\downarrow\rangle + |\uparrow\downarrow\uparrow\rangle + |\downarrow\uparrow\uparrow\rangle\,, \\
|Q_{-1/2}\rangle &= |\downarrow\downarrow\uparrow\rangle + |\downarrow\uparrow\downarrow\rangle + |\uparrow\downarrow\downarrow\rangle\,, \\
|Q_{-3/2}\rangle &= |\downarrow\downarrow\downarrow\rangle\,,
\end{aligned}$$

with eigenenergies $E(Q_{S_z}) = g\mu_B B_0 S_z$. Normalization factors are omitted for clarity.

[4]The four doublets $|\Delta^{\pm}_{S_z}\rangle$ are

$$\begin{aligned}
|\Delta^{\pm}_{+1/2}\rangle &= (J_{12} - J_{23} \pm J_\Sigma)\,|\uparrow\uparrow\downarrow\rangle + (J_{23} \mp J_\Sigma)\,|\uparrow\downarrow\uparrow\rangle - J_{12}\,|\downarrow\uparrow\uparrow\rangle\,, \\
|\Delta^{\pm}_{-1/2}\rangle &= (J_{12} - J_{23} \pm J_\Sigma)\,|\downarrow\downarrow\uparrow\rangle + (J_{23} \mp J_\Sigma)\,|\downarrow\uparrow\downarrow\rangle - J_{12}\,|\uparrow\downarrow\downarrow\rangle\,,
\end{aligned}$$

where $J_\Sigma = \sqrt{{J_{12}}^2 + {J_{23}}^2 - J_{12}J_{23}}$ with eigenenergies $E(\Delta^{\pm}_{S_z}) = -(J_{12} + J_{23} \mp J_\Sigma)/2 + g\mu_B B_0 S_z$. Normalization factors are again omitted for clarity.

pressed, $\Delta_{Z,12}$ and $\Delta_{Z,23}$ dominate and therefore the eigenstates and eigenenergies are defined by the Zeeman energy.

3.2 Qubit Readout

Single-spin detection is technically challenging in general, since the magnetic moment of a single spin is very small. However, in QDs, it can be performed relatively easily, for instance by combining spin-to-charge conversion and charge readout. Here representative qubit readout techniques are reviewed and discussed.

3.2.1 Energy-Selective Readout

In energy-selective spin readout, the QD electrochemical potentials are tuned so that only one of the two Zeeman-split sublevels is energetically higher than the Fermi level in the reservoir. When the Zeeman energy is larger than the thermal energy $k_B T_e$ in the reservoirs (T_e is the electron temperature), only the electron with the higher energy spin can tunnel out, and the one with the opposite spin remains trapped. This single-electron tunneling process can be detected, for example by monitoring a charge sensor (see §2.2.3). In ref. [5] single-shot readout of a single spin trapped in a singe QD is realized in this manner. Moreover, in ref. [53] independent single-shot readout of two spins in a DQD is demonstrated, and the correlations between two spins are probed.

Possible drawbacks of this scheme are that it requires either sufficiently high Zeeman energy or low electron temperature and that it is inevitably destructive.

3.2.2 Pauli Spin Blockade

Since spin is generally preserved in the tunneling process, there are some cases where the spin selection rule governs the electron transport through a QD. One prominent example is the Pauli spin blockade (PSB), the phenomena that the electron transport is blocked due to the Pauli exclusion principle. It was first observed in a vertical GaAs DQD [54], and later in many DQD systems [14, 55–57].

The mechanism of the PSB is as follows. Let us focus for simplicity[5] on the detuning range $E_{\mathrm{ST}} > \varepsilon > 0$ in the electron transport cycle $(1,0) \to (1,1) \to (2,0) \to (1,0)$ (see Fig. 3.2). If in the $(1,0) \to (1,1)$ transition a $(1,1)$ singlet state is formed, the electron in QD2 can tunnel to QD1, forming the $(2,0)$ singlet state. Then the system can return to the initial $(1,0)$ charge configuration, completing a cycle. If, on the other hand, one of the $(1,1)$ triplet states is formed in the $(1,0) \to (1,1)$ process, inter-dot tunneling is prohibited, since $(2,0)$ triplet states are higher in energy due to the Pauli exclusion. The electron in QD2 cannot tunnel back to the reservoir, either. Although the T_0 state can be mixed relatively quickly with the $(1,1)$ singlet due to the Overhauser field (see §3.5), the decay time of T_+ and T_- is in the order of milliseconds if they are sufficiently Zeeman lifted. Therefore, once a $(1,1)$ triplet with parallel spins is formed, the system is stuck in the $(1,1)$ charge configuration and the transport in this region is totally suppressed.

Detecting a current or charge configuration in the PSB region gives a measure of finding probability of anti-parallel spins. By waiting longer than the decay time in the same region, the spin state is initialized in either T_+ or T_-, since they are the only states that cannot escape quickly. Therefore, the PSB effect is widely used in the proof-of-principle spin-qubit experiments, to initialize as well as to readout the single-spin qubit state. Furthermore, a distinction between the parallel spin states is also possible with a ramp pulse which is adiabatic with respect to t_{c}. By gradually changing ε from $(1,1)$ to $(2,0)$ region, the ground and excited state defined by local Zeeman energies are mapped to $(2,0)$ singlet and T_0, respectively [17, 58].

3.3 Electron Spin Resonance

Single spin rotations, or single-qubit operations of a single-spin qubit, are commonly performed via electron spin resonance (ESR). This section first describes a generic theory of ESR and then several schemes for realizing ESR of single spins in QDs.

[5] PSB is commonly observed where transitions such as $(2M+1, 2N+1) \to (2M+2, 2N)$ are involved.

3.3.1 Theory of Electron Spin Resonance

ESR is a magnetic resonance where electron spins are flipped under field excitation consistent with the Zeeman energy, say from $|\uparrow\rangle$ to $|\downarrow\rangle$. Such vertical spin rotations require a control magnetic field that is perpendicular to the static magnetic field $B_0 \parallel \hat{z}$, applied to define the qubit (see Eq. (3.1)). However, the Larmor precession tends to average out the effect of most interactions, static or time-varying, in directions other than z, that work on timescales longer than the precession period. Such an averaging effect is canceled in the reference frame rotating at the Larmor frequency (see §3.1.1). This indicates that spin flips can be caused by a perpendicular magnetic field rotating synchronously with spin, even with the amplitude $\ll B_0$. Moreover, the rotating magnetic field can be replaced by an experimentally-accessible oscillating magnetic field, which is a superposition of two counter-rotating fields.

From the above considerations, we apply a magnetic field oscillating in the x direction at a frequency $\omega/2\pi(\approx f_{\mathrm{L}})$ with an amplitude B_{ac}. The time-dependent Hamiltonian of the electron spin is

$$\mathcal{H}_{\mathrm{lab}} = \frac{g\mu_{\mathrm{B}}B_0}{2}\sigma_z + \frac{g\mu_{\mathrm{B}}B_{\mathrm{ac}}}{2}\cos(\omega t+\varphi)\sigma_x, \tag{3.6}$$

where σ_i are the Pauli matrices and φ is the phase of the applied field at $t = 0$. In the reference frame rotating at the frequency $\omega/2\pi$, the spin's time evolution becomes much simpler and clearer. From Eq. (3.2), the corresponding Hamiltonian is

$$\mathcal{H}_{\mathrm{ref}} \;=\; -\frac{\hbar\delta}{2}\sigma_z + \hbar\omega_{\mathrm{R}}\cos(\omega t+\varphi)\left[\cos(\omega t)\sigma_x - \sin(\omega t)\sigma_y\right], \tag{3.7}$$

where $\omega_{\mathrm{R}} = g\mu_{\mathrm{B}}B_{\mathrm{ac}}/2\hbar$, $\delta/2\pi = (\omega-\omega_{\mathrm{L}})/2\pi$ is the frequency detuning with $\omega_{\mathrm{L}} = 2\pi f_{\mathrm{L}}$.

When $|\omega_{\mathrm{R}}| \ll |\omega|$, which is the case in the regime of experimental interest, terms in Eq. (3.7) that oscillate at 2ω cannot contribute much to spin evolution [59]. This is because their effect, only present on a timescale $2\pi/\omega_{\mathrm{R}}$, is averaged by their own rotation with respect to the spin. The so-called rotating wave approximation neglects these two terms of counter-rotating fields. The

effective Hamiltonian is then described as,

$$\mathcal{H}_{\mathrm{ref}} \approx -\frac{\hbar\delta}{2}\sigma_z + \frac{\hbar\omega_{\mathrm{R}}}{2}\left[(\cos\varphi)\,\sigma_x + (\sin\varphi)\,\sigma_y\right] \equiv \mathcal{H}_{\mathrm{ESR}}. \tag{3.8}$$

Under $\mathcal{H}_{\mathrm{ESR}}$, spin rotates around $(\omega_{\mathrm{R}}\cos\varphi)\hat{x} + (\omega_{\mathrm{R}}\sin\varphi)\hat{y} - \delta\hat{z}$ at a frequency $\sqrt{{\omega_{\mathrm{R}}}^2 + \delta^2}/2\pi$ in the reference frame (Fig. 3.4). In particular, in the ESR resonance condition of $\delta = 0$ i.e. $\omega = \omega_{\mathrm{L}}$, spin will flip completely, at the Rabi frequency $\omega_{\mathrm{R}}/2\pi$. ESR suffices for arbitrary single-spin rotations, since the rotation axis can be changed arbitrarily in the xy plane by choice of the initial phase of the field φ [60, 61].

It is of experimental interest to capture the coherent time evolution of spin under ESR drive. Suppose the initial spin state is $|\uparrow\rangle$, the probability of finding spin in $|\downarrow\rangle$ at a time t is given by the Rabi formula,

$$P_{\mathrm{flip}} = \frac{{\omega_{\mathrm{R}}}^2}{2{\Omega_{\mathrm{R}}}^2}\left[1 - \cos(\Omega_{\mathrm{R}}t)\right], \tag{3.9}$$

where $\Omega_{\mathrm{R}}/2\pi = \sqrt{{\omega_{\mathrm{R}}}^2 + \delta^2}/2\pi$ is the generalized Rabi frequency. At complete resonance, Eq. (3.9) simplifies to $\frac{1}{2}\left[1 - \cos(\omega_{\mathrm{R}}t)\right]$, yielding an ideal Rabi oscillation. Figure 3.4(c) shows a characteristic chevron pattern in the 2-dimensional plot of the spin flip probability as a function of time and the frequency detuning from resonance.

3.3.2 Micro-Magnet Electron Spin Resonance

ESR requires an oscillating magnetic field perpendicular to a static magnetic field. The main experimental challenge is how to feed a high-frequency effective magnetic field to the QDs at cryogenic temperatures. This favors the use of electric fields in place of magnetic fields, as they are more localized and free from the Joule heating, which inevitably accompanies a.c. current injection. However, unlike magnetic fields, electric fields do not directly couple to spin. Therefore, some mediating mechanism is necessary to drive ESR electrically [62]. One way of realizing such mediation is to impose a slanting magnetic field by proximal micro-magnets (MMs) [20, 21] (Fig. 3.5(a)). This technique is also advantageous for scaling, as the MMs designed in the right manner can

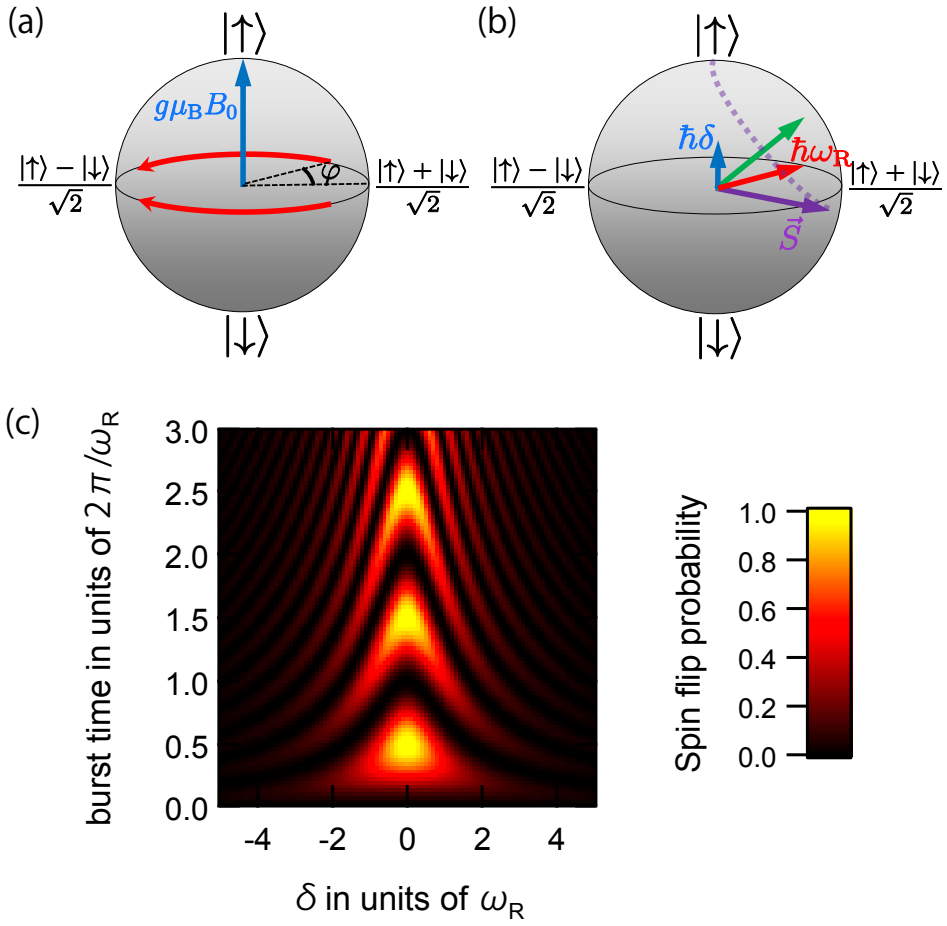

Figure 3.4: Electron spin resonance. (a) An oscillatory magnetic field can be decomposed into two counter-rotating magnetic fields. In the laboratory frame time evolution of spin under ESR drive is mutation: the S_z component changes slowly during rapid precession. (b) In the reference frame rotating at the frequency of the applied field, the field becomes static. The remaining effect of the external field B_0 in the z direction is $\hbar\delta$ in energy. The rotation axis and speed is given by the vector sum of these contributions. (c) Chevron pattern of spin flip probability. The vertical axis is the evolution time or equivalently the duration of ESR excitation. The horizontal axis is $(2\pi\times)$ the frequency detuning normalized by $(2\pi\times)$ the ESR Rabi frequency. At resonance, the probability oscillates from 0 to 1. A slightly off-resonant magnetic field rotates spin only imperfectly with a shorter oscillation period.

make the resonance frequencies different from dot to dot [63] (Fig. 3.5(b),(c)).

Suppose a time-dependent electric field $\boldsymbol{E}(t)$ is applied to the electron confined in a QD with a harmonic potential $V(\boldsymbol{r}) = m^*{\omega_0}^2(y^2+z^2)/2$ and magnetic field distribution $\boldsymbol{B}(\boldsymbol{r})$ [20, 64]. Here, m^* is the effective mass of an electron. The Hamiltonian is written as

$$\mathcal{H}_{\rm lab} = \frac{\boldsymbol{p}^2}{2m^*} + V(\boldsymbol{r}) + e\boldsymbol{E}(t)\cdot\boldsymbol{r} + \frac{1}{2}g\mu_{\rm B}\boldsymbol{B}(\boldsymbol{r})\cdot\boldsymbol{\sigma}. \tag{3.10}$$

Consider a local magnetic field whose x component is slanted in the z direction: $\boldsymbol{B}(x,z) = (B_0+b_{\rm sl}x)\hat{z}+(B_x+b_{\rm sl}z)\hat{x}$. Here B_0 is the external magnetic field and $b_{\rm sl}x\hat{z}$ is added to satisfy Maxwell's equations. Such magnetic field distribution can be obtained experimentally for instance by placing a MM on top of a lateral QD. The term $b_{\rm sl}x\hat{z}$ can be neglected assuming strong confinement in the x direction. Since B_x is much smaller than B_0, it only slightly modifies the quantization axis. A crucial role is played by the term $b_{\rm sl}z\hat{x}$, which mixes the spin and charge degrees of freedom via the last term in Eq. (3.10).

When a microwave is applied in the z direction at a frequency of $\omega/2\pi$, Eq. (3.10) can be reorganized as follows:

$$\begin{aligned}
\mathcal{H}_{\rm lab} &= \mathcal{H}_0 + \mathcal{H}_{\rm mix} + \mathcal{H}_{\rm exc}(t) && (3.11)\\
\mathcal{H}_0 &= \frac{\boldsymbol{p}^2}{2m^*} + V(\boldsymbol{r}) + \frac{g\mu_{\rm B}B_0}{2}\sigma_z && (3.12)\\
\mathcal{H}_{\rm mix} &= \frac{g\mu_{\rm B}b_{\rm sl}z}{2}\sigma_x && (3.13)\\
\mathcal{H}_{\rm exc}(t) &= eE_{\rm ac}\sin(\omega t)z. && (3.14)
\end{aligned}$$

$\mathcal{H}_0$ does not mix the spin and orbital degrees of freedom. Then the eigenstates, $|m,n;\sigma_z\rangle$, and eigenenergies, $\epsilon_{m,n;\sigma_x}$, of $\mathcal{H}_0$ can be expressed as $\langle y,z|m,n;\sigma_z\rangle = \phi_m(y)\phi_n(z)\psi_{\sigma_z}$ and $\epsilon_{m,n;\sigma_z} = \hbar\omega_0\,(m+n+1) + \frac{g\mu_{\rm B}B_0}{2}\sigma_z$, respectively, where $\phi_m(y)$ and $\phi_n(z)$ are the orbital eigenstates in the harmonic potential, and ψ_{σ_z} is a spinor. The perturbation of $\mathcal{H}_{\rm mix}$ mixes spins with orbitals. The hybridized two lowest levels can be regarded as pseudo-spins $|\sigma_{\rm p}\rangle$. By calculating the eigenstates and eignenergies of $\mathcal{H}_0+\mathcal{H}_{\rm mix}$ up to first order in the characteristic

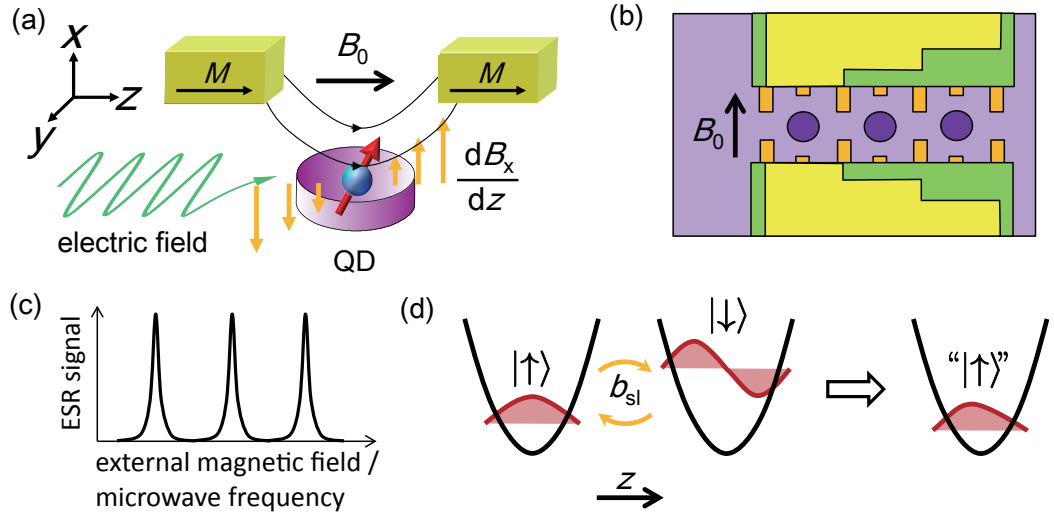

Figure 3.5: ESR with a MM. (a) Device configuration for MM-ESR. The MM is placed on top of the QD, and magnetized by the external field ($\parallel z$). It is so designed that the out-of-plane (x-) component of the stray field is slanted at the QD position. The slanting field, $b_{\rm sl} = {\rm d}B_x/{\rm d}z$, couples the spin states with the orbital states. A high-frequency electric field is applied in the z direction to drive ESR. A classical view of the scheme is that spin feels an oscillatory magnetic field perpendicular to the external field when the time-varying electric field shakes the QD electron in the slanting field. (b) A QD array integrated with a MM. QDs, metal gates, an insulating layer and a MM are colored in purple, orange, green and yellow, respectively. A properly-designed MM produces large differences of the z-component of the stray field between the neighboring dots, making ESR conditions different from dot to dot. (c) Expected ESR spectra from a QD array. The horizontal axis is the external magnetic field, or the microwave frequency. The peak spacings are given by interdot differences of the z-component of the MM field. When peaks are separate from each other, a single spin can be rotated in an addressable manner, i.e. without flipping other spins. (d) Formation of a qubit state. An "up" state of pseudo-spin is a hybridized state of spin-up in the orbital ground state and spin-down in the orbital excited states. Here only the first excited state, which has the largest contribution among the excited states, is drawn for simplicity.

coupling energy $E_{\rm sl} \equiv g\mu_{\rm B} b_{\rm sl}\sqrt{\hbar/m^*\omega_0}$, we obtain

$$|\sigma_{\rm p}\rangle = |0,0;\sigma_z\rangle - \sum_{n>0} \frac{\frac{g\mu_{\rm B}}{2} b_{\rm sl} \langle 0,n|z|0,0\rangle}{n\hbar\omega_0 - g\mu_{\rm B}B_0\sigma_z} |0,n;-\sigma_z\rangle \,. \tag{3.15}$$

There is no renormalizaion of the eigenenergies in leading order of $E_{\rm sl}$, since $\langle m,n|z|m,n\rangle = 0$ from confinement symmetry.

Now we can include the effect of the oscillatory electric field onto the pseudo-spin $|\sigma_{\rm p}\rangle$. The diagonal elements of $\mathcal{H}_{\rm exc}$ are 0 up to first order in $E_{\rm sl}$, due to the confinement symmetry and the linearity of the slanting magnetic field. The non-diagonal elements can be calculated as $\langle -\sigma_{\rm p}|\mathcal{H}_{\rm exc}|\sigma_{\rm p}\rangle = \frac{g\mu_{\rm B}B_{\rm ac}}{2}\sin(\omega t) + \mathcal{O}(E_{\rm sl})^2$, where the amplitude of the effective magnetic field is,

$$B_{\rm ac} = -\sum_{n>0} \frac{2n\hbar\omega_0 b_{\rm sl} e E_{\rm ac}}{(n\hbar\omega_0)^2 - (g\mu_{\rm B}B_0)^2} |\langle 0,0|z|0,n\rangle|^2 \approx -\frac{eE_{\rm ac}b_{\rm sl}}{m^*{\omega_0}^2}. \tag{3.16}$$

The effective Hamiltonian of the pseudo-spin system in the slanting magnetic field is, up to leading order of $E_{\rm sl}$,

$$\mathcal{H}_{\rm lab} = \hbar\omega_0\sigma_{\rm p0} + \frac{g\mu_{\rm B}B_0}{2}\sigma_{{\rm p}z} + \frac{g\mu_{\rm B}B_{\rm ac}}{2}\sin(\omega t)\sigma_{{\rm p}x}, \tag{3.17}$$

with $\sigma_{{\rm p}i}$ the Pauli matrices of the pseudo-spin. This coincides with the ESR Hamiltonian given in Eq. (3.6) up to the overall energy shift, indicating that ESR can be electrically driven in a slanting magnetic field.

3.3.3 Comparison with Other Techniques

Single ESR in QDs has been achieved in several ways other than MM-ESR. Magnetic drive is the scheme adopted in the first demonstration, where a.c. current is injected to an on-chip coil [45]. The spin-orbit interaction (SOI) provides indirect coupling necessary for electrical spin control, which is favorable in terms of addressability and the Joule heating problem [65]. Although in GaAs, the Rabi frequency of SOI-mediated ESR is limited to a few MHz due to the weak SOI [66], it greatly improves in materials with stronger SOI such as InAs [61] and InSb [67]. The hyperfine interaction can also mediate electrically driven ESR, with no coherent oscillations [68]. Table 3.1 summarizes spin flip

Table 3.1: Spin flip time T_π and phase coherence times of single ESR in QDs

ESR method	T_π	${T_2}^*$	${T_2}^{\text{echo}}$
Micro-coil ESR in GaAs QDs [45]	54 ns	37 ns [60]	400 ns [60]
SOI-ESR in GaAs QDs [66]	110 ns		
MM-ESR in GaAs QDs [69]	33 ns		
SOI-ESR in InAs QDs [61]	8.6 ns	8 ns	50 ns
SOI-ESR in InSb QDs [67]	4.8 ns	8 ns	34 ns

times and phase coherence times of single ESR in QDs.

3.4 Two-Qubit Operation

The simplest two-qubit gate implementation in the single-spin qubit system is to use the exchange interaction between spins in neighboring dots [6, 70]. It is readily seen that the exchange term $-J\left|\mathrm{S}\right\rangle\left\langle\mathrm{S}\right|$ in Eq. (3.5) swaps spin states by rewriting it as $\frac{J}{2}\left(\left|\uparrow\downarrow\right\rangle\left\langle\downarrow\uparrow\right| + \left|\downarrow\uparrow\right\rangle\left\langle\uparrow\downarrow\right| + \left|\mathrm{T}_+\right\rangle\left\langle\mathrm{T}_+\right| + \left|\mathrm{T}_-\right\rangle\left\langle\mathrm{T}_-\right|\right)$, ignoring the global shift in energy. From a viewpoint of qubit control it is crucial that $J(\varepsilon)$ can be switched by the gate voltage (see Eq. (3.4)). The SWAP operation can be performed by starting deep in the Coulomb blockade regime with $J \to 0$ and activating the exchange interaction at some detuning ε_E for a time $t_\mathrm{SWAP} = \pi\hbar/J(\varepsilon_\mathrm{E})$. By reducing the interaction time by half the $\sqrt{\mathrm{SWAP}}$ gate is obtained, which is a maximally entangling gate.

To perform the SWAP gates, it is required that $J(\varepsilon_\mathrm{E})$ can be made much larger than the local Zeeman energy difference Δ_Z (see §3.1.2). At the same time, non-zero Δ_Z is a must for addressable ESR rotations (see §3.3.2). By properly tuning the interdot tunnel coupling, $J(\varepsilon_\mathrm{E})/\Delta_\mathrm{Z}$ can be made $\gg 1$, and above-GHz SWAP rotations have been demonstrated in GaAs lateral QDs [17]. In the opposite limit where $J(\varepsilon_\mathrm{E})/\Delta_\mathrm{Z} \ll 1$, the natural two-qubit gate evolves from $\sqrt{\mathrm{SWAP}}$ to the controlled-phase (CPHASE), another maximally entangling gate [6, 71]. In this regime the change in $J(\varepsilon)$ (from 0 to $J(\varepsilon_\mathrm{E})$) does not change the system eigenstates from $\left|\mathrm{T}_+\right\rangle, \left|\uparrow\downarrow\right\rangle, \left|\downarrow\uparrow\right\rangle, \left|\mathrm{T}_-\right\rangle$ but shifts the eigenenergies of two anti-prallel spin states with finite singlet components. The phase accumulation rate, which is proportional to energy, depends on the relative spin

orientation when J is turned on.

Figure 3.6 illustrates a two-qubit experiment in a GaAs lateral DQD [72]. In this experiment, the combination of an exchange operation and two single-spin ESR rotations produces partially entangled states. The degree of entanglement of the output state is simulated using the concurrence $\mathcal{C}$ as a measure. $\mathcal{C} = 1$ for maximally entangled qubits, and $\mathcal{C} = 0$ for uncorrelated qubits.

3.5 Sources of Decoherence

All qubits interact, if only very weakly, with their environments, which leads to information loss [73]. Such loss of qubit information can be basically categorized into two general types [9,59]. The first type is energy relaxation where the qubit gradually evolves toward thermodynamic equilibrium, transferring energy to the environment. The characteristic time, T_1, is called the *energy relaxation time*. The second is decoherence, where the qubit loses phase information through interactions with the environment, while preserving its energy. The time constant of this phase randomization process, T_2, is called the (*intrinsic*) *phase coherence time*. Phase information is lost more quickly when the average is taken over ensembles in an inhomogeneous environment. T_2^*, the *ensemble phase coherence time*, gives the decay time of the ensemble qubit phase.

Using the density matrix formalism, the density matrix ρ_q of a qubit interacting with its environment $\mathcal{E}$ is given by taking a partial trace of the whole density matrix ρ_tot over those degrees of freedom in $\mathcal{E}$: $\rho_\mathrm{q} = \mathrm{Tr}_\mathcal{E}[\rho_\mathrm{tot}]$ [9]. Using the *Bloch vector* $\boldsymbol{v}_\mathrm{q}$, which is defined by $\rho_\mathrm{q} = \frac{1}{2}(\sigma_0 + \boldsymbol{v}_\mathrm{q} \cdot \boldsymbol{\sigma})$, the Bloch sphere is extended for general states, with the surface and the interior corresponding to *pure* and *mixed states*, respectively[6]. The coherence decay of a qubit can be represented as the decay of the off-diagonal elements of ρ_q. If the noise is white, Markovian, the coherence is expected to decay single exponentially, $\langle\uparrow|\,\rho_\mathrm{q}(t)\,|\downarrow\rangle \propto \mathrm{e}^{-t/T_2^*}$. If the Markovian noise has predominantly low frequency components, the coherence decay will be Gaussian: $\langle\uparrow|\,\rho_\mathrm{q}(t)\,|\downarrow\rangle \propto \mathrm{e}^{-(t/T_2^*)^2}$.

[6]For instance, immediately after initialization, the qubit is a pure state; all qubit information is there, the state can be represented by a quantum state, and $\mathrm{Tr}\left[{\rho_\mathrm{q}}^2\right] = 1$ so that $|\boldsymbol{v}_\mathrm{q}| = 1$. If the qubit evolves into a mixed state via interactions, or in other words qubit information is partially spread with the surrounding system, statistical treatment makes $\mathrm{Tr}\left[{\rho_\mathrm{q}}^2\right] < 1$ and $|\boldsymbol{v}_\mathrm{q}| < 1$.

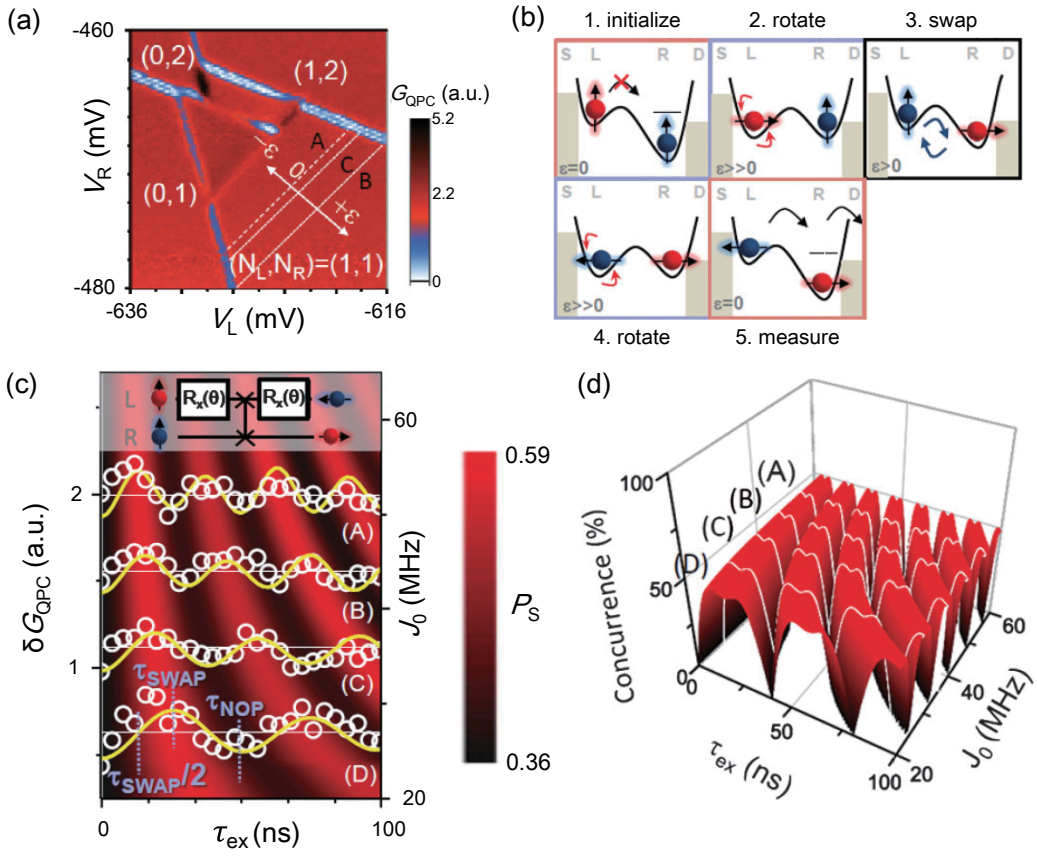

Figure 3.6: Entanglement control experiment via exchange interaction. (a) Stability diagram of the relevant device. The experiment is performed in the vicinity of the $(1,1)$-$(0,2)$ boundary. (b) Cycle of the two-qubit gate operation. S, D, L and R mean source, drain, left, and right QDs, respectively. After PSB initialization in either T_+ or T_- (on line A indicated in (a)), the left spin is rotated by $3\pi/2$ in $(1,1)$ Coulomb blockade by ESR (on line B). Then the exchange interaction is turned on for a time τ_{ex} by moving closer to $(1,1)$-$(0,2)$ (on line C), followed by an ESR $\pi/2$-rotation on the left spin in $(1,1)$ Coulomb blockade. The probability of finding anti-parallel spins is subsequently measured in the PSB region. The ideal final state for an initial state of $|T_+\rangle$ is $(\frac{i}{2}\sin\alpha_{ex}-\cos\alpha_{ex})|T_+\rangle+\frac{i}{2}\sin\alpha_{ex}|T_-\rangle-\frac{1}{\sqrt{2}}\sin\alpha_{ex}|S\rangle$, with $\alpha_{ex}=J\tau_{ex}/\hbar$. Two ESR rotation angles are chosen such that the final state has no T_0 component for an initially T_- case as well. (c) Result of the two-qubit gate operation. $\Delta_Z/J_0=0.69$, 0.73, 0.78, and 0.77, respectively for traces (A)-(D). Signals take maximums (minimums) for τ_{ex} equal to an odd (even) multiple of $\pi\hbar/J_0$, when the exchange process approximates SWAP (no) operation. Here J_0 is defined by the oscillation period. The color plot shows calculated singlet probability P_S as a function of J_0 and τ_{ex}. (d) Simulated concurrence. $\mathcal{C}$ is maximized to 0.5 when $\tau_{ex}=(n+\frac{1}{2})\pi\hbar/J_0$, with $n=0,1,2\ldots$ Figures are adopted from [72].

Relaxation and decoherence can be caused by any type of fluctuation: the electrical noise in the control circuit, background moving charges, fluctuating magnetic impurities, lattice vibrations and nuclear spin fluctuations. Qubit coherence is strongly affected by the spectrum and dynamics of relevant fluctuations and the system Hamiltonian (e.g. control field) [74]. For instance, dephasing of exchange operations is dominated by the voltage noise, to which spin is otherwise immune [49, 75, 76]. For an electron spin isolated in GaAs QDs, the most important interactions with the environment are the hyperfine coupling, which limits T_2^*, and the SOI+phonon coupling, which causes qubit relaxation [8, 13, 49, 77]. This section explains these dominant sources of relaxation and decoherence of the electron spins in GaAs-based QDs.

3.5.1 Spin-Orbit Interaction in Quantum Dots

There are two main sources of the SOI for electrons in a 2DEG formed in III-V semiconductors. The first one is the Dresselhaus term [78], which is present in crystals with bulk inversion asymmetry (BIA). The second one is the Rashba term [79], which results from the structural inversion asymmetry (SIA), or asymmetry of confining potentials, for example at a heterointerface [80]. Due to the SOI, the eigenstates become admixtures of spin and orbital states [77]. The two lowest pseudo-spin states are

$$|\sigma_z\rangle_{\mathrm{p}} = |0,0;\sigma_z\rangle + \sum_{(m,n)\neq(0,0)} \frac{\langle m,n;-\sigma_z|\,\mathcal{H}_{\mathrm{SO}}\,|0,0;\sigma_z\rangle}{E_{0,0}-E_{m,n}-E_{\mathrm{Z}}\sigma_z}\,|m,n;-\sigma_z\rangle\,, \quad (3.18)$$

where $\mathcal{H}_{\mathrm{SO}}$ is the spin-orbit Hamiltonian, and m and n are the quantum numbers to characterize the orbitals in the QD. Unlike pure spin states, these pseudo-spin states are susceptible to the electrical noise, produced predominantly by phonons. Since only phonons with a specific energy can contribute from energy conservation, the relaxation time is

$$\frac{1}{T_1} = \frac{2\pi}{\hbar}\left[{}_{\mathrm{p}}\langle\uparrow|\,\mathcal{H}_{\mathrm{e,ph}}\,|\downarrow\rangle_{\mathrm{p}}\right]^2 D_{\mathrm{ph}}(E_{\mathrm{Z,p}}), \quad (3.19)$$

where $D_{\mathrm{ph}}(E)$ is the phonon density of states, $E_{\mathrm{Z,p}}$ is the Zeeman energy of the pseudo-spin, and $\mathcal{H}_{\mathrm{e,ph}}$ is the electron-phonon coupling Hamiltonian.

T_1 depends on the phonon density of states at the energy splitting of the pseudo-spin due to conservation of energy. Due to small energy scales, the effect of piezoelectric phonons dominates over that of deformation potential phonons and optical phonons. An elaborate calculation of the $E_{\mathrm{Z,p}}$ dependence of all elements predicts that $T_1 \propto B^{-5}$ in the low temperature limit [77]. Experimentally measured values for T_1 between Zeeman sublevels in a one-electron GaAs QD range from 120 μs at 14 T to 170 ms at 1.75 T, with the expected B^{-5} dependence [5, 8, 81]. In leading order in $\mathcal{H}_{\mathrm{SO}}$, there is no pure phase randomization, such that in fact $T_2 = 2T_1$ [82].

3.5.2 Interaction with Nuclear Spins

Due to its orbital spread, an electron spin in a QD interacts with abundant nuclear spins in the host material, unless the nuclei are spinless (see Fig. 3.7(a)). The complex interplay between a single electron spin and the nuclear spin bath is known as the central spin problem [83, 84]. Since the electron wave function is non-zero at the nucleus, the Hamiltonian of hyperfine interactions is given by the Fermi contact hyperfine interaction,

$$\mathcal{H}_{\mathrm{HF}} = \sum_{k}^{N} A_k \boldsymbol{I}_k \cdot \boldsymbol{S}, \tag{3.20}$$

where $\boldsymbol{I}_k$ and $\boldsymbol{S}$ are the spin operators for the k-th nuclear spin and the electron spin, respectively. The coupling strength A_k between the k-th nuclear spin and the electron spin is k-dependent, due to inhomogeneous overlap of the electron and the nucleus wave functions. The dynamics of nuclear-nuclear flipflop, mediated by the hyperfine interaction, then becomes a complex many-body problem. A useful semiclassical description is to treat the effect of collective nuclear spins as an effective magnetic field,

$$\mathcal{H}_{\mathrm{HF}} = \left(\sum_{k}^{N} A_k \boldsymbol{I}_k \right) \cdot \boldsymbol{S} = g\mu_{\mathrm{B}} \boldsymbol{B}_{\mathrm{N}} \cdot \boldsymbol{S}, \tag{3.21}$$

where $\boldsymbol{B}_N$ is the *Overhauser field*, the effective nuclear field seen by electron spins due to nuclear spins.

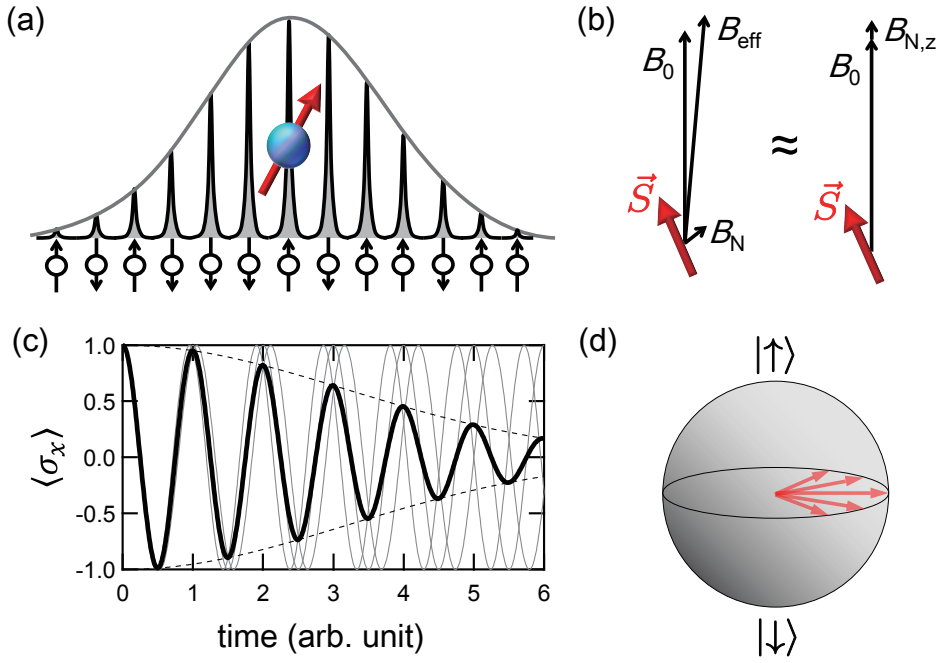

Figure 3.7: Effect of the hyperfine interaction. (a) Electron wave function overlap. One electron spin interacts with lots of nuclear spins in a semiconductor QD. The coupling strength with each nucleus is inhomogeneous, proportional to the overlap squared between the nucleus and the electron wave function. (b) Correction due to the Overhauser field. Longitudinal Overhauser field $B_{\text{N},z}$ adds directly to the external field B_0. Transverse components $B_{\text{N},x}$ and $B_{\text{N},y}$, in contrast, only change the total effective field in second order when $B_0 \gg |\boldsymbol{B}_{\text{N}}|$. The Larmor frequency is modified as $f_{\text{L}} = |g|\mu_B(B_0 + B_{\text{N},z})/h$. (c) Dephasing of an ensemble spin. Gray lines show $\langle\sigma_x\rangle$ (the amplitudes of the x component) of the electron spins initialized in $(|\uparrow\rangle + |\downarrow\rangle)/\sqrt{2}$, under free precession about $(B_0 + B_{\text{N},z})\hat{z}$ for three different values of $B_{\text{N},z}/B_0 = -0.05,\ 0,\ +0.05$. The solid black line is $\langle\sigma_x\rangle$ of an ensemble of spins, initially $(|\uparrow\rangle + |\downarrow\rangle)/\sqrt{2}$, under Gaussian distributed $B_{\text{N},z}$. The standard deviation $\sqrt{\langle(B_{\text{N},z})^2\rangle}/B_0 = 0.05$. Broken lines indicate a Gaussian decay of the envelope, and of the phase coherence. (d) Schematics of dephasing in the Bloch sphere. In the spin reference frame, spin precesses in an uncontrollable manner, at a rate proportional to the longitudinal Overhauser field $B_{\text{N},z}$. The ensemble spin Bloch vector evolves inwards, indicating loss of coherence. In this process, qubit energy is preserved, and only the phase information is lost.

In GaAs-based QDs, all natural isotopes of Ga and As, ^{69}Ga, ^{71}Ga and ^{75}As are spin 3/2, and $|\boldsymbol{B}_{\rm N}|_{\rm max} \sim 5$ T when the nuclear spins are fully polarized [85]. This magnitude is independent of N given the host material. Under typical experimental conditions, nuclear spins are in thermodynamic equilibrium, as their Zeeman energies are much smaller than the thermal energy even at cryogenic temperatures. The Boltzmann distribution then gives (almost) zero average nuclear polarization. From the central-limit theorem the statistical fluctuation about the average follows the Gaussian distribution with a standard deviation $\sqrt{\langle|\boldsymbol{B}_{\rm N}|^2\rangle} \sim |\boldsymbol{B}_{\rm N}|_{\rm max}/\sqrt{N}$. In GaAs QDs, $N \simeq 10^6$ and the nuclear field fluctuation is typically a few mT [14, 17].

The effective magnetic field the electron spin feels is a sum of the external field $\boldsymbol{B}_0$ ($\parallel \hat{z}$) and the Overhauser field: $\boldsymbol{B}_{\rm eff} = \boldsymbol{B}_0 + \boldsymbol{B}_{\rm N}$. For $|B_0| \gg |\boldsymbol{B}_{\rm N}|$, the contribution of the transverse components becomes negligible, and $\boldsymbol{B}_{\rm eff} \approx (B_0 + B_{{\rm N},z})\hat{z}$ (Fig. 3.7(b)). Time-ensemble average over fluctuations of $B_{{\rm N},z}$ results in dephasing (Fig. 3.7(c)). Assuming frozen $B_{{\rm N},z}$ following a Gaussian distribution, the spin coherence decay is Gaussian with a characteristic time [86]

$$T_2^* = \frac{\hbar\sqrt{2}}{|g|\mu_{\rm B}\sqrt{\langle(B_{{\rm N},z})^2\rangle}}. \tag{3.22}$$

In GaAs QDs with $g \approx -0.4$, $\sqrt{\langle(B_{{\rm N},z})^2\rangle} = 1$ mT corresponds to T_2^* as short as 40 ns. Corrections to Markovian spin dynamics and the usual exponential decay of coherence due to hyperfine interaction are extensively discussed in ref. [87].

In systems coupled to a bath with a long memory time, including the electron spin interacting with nuclear spins, T_2^* does not reflect the intrinsic coherence of the system, i.e. $T_2 \gg T_2^*$. A better characterization of the lower bound on T_2 is provided by echo measurements such as Hahn echo and the Carr-Purcell-Meiboom-Gill (CPMG) decoupling, which partially cancel the dynamics caused by low frequency fluctuations [59]. The phase coherence time can be extended by echo pulses up to 100 μs ($= T_2^{\rm echo}$) for electron spin qubits coupled to a nuclear bath in GaAs QDs [60, 88]. This is more than three orders of magnitude longer than the typical operation time in this system, 1 - 100 ns.

Preparation of less fluctuating nuclear environment will considerably extend T_2^* and increase the quantum gate accuracy. The hyperfine interaction offers a

control knob of the nuclear bath via the electron spin; it mediates electron-nuclear flip-flops and generates dynamic nuclear polarization (DNP) under asymmetric spin pumping rates [84]. Under most conditions, however, DNP is small because pumping is suppressed due to the Zeeman energy mismatch between the nuclear and electron spins. Still, DNP can be observed in electron transport in the PSB region including S-T_+ and/or S-T_- degeneracy points, as hysteretic, oscillatory and bistable leakage current behavior [14, 89–91]. In a similar manner, spin transfer into the nuclear bath can be controlled by adiabatic passage across the S-T_+ degeneracy point [58, 92, 93]. ESR can drive DNP away from degeneracy points, compensating the energy cost for electron-nuclear flip-flops by a resonant a.c. excitation [68, 94, 95]. Observed complex interplay between slow nuclear spin dynamics and fast electron spin dynamics has triggered a large amount of theoretical work on explanations for observation and proposals for suppressing fluctuations [87, 96–102].

Chapter 4

Optimization of Micro-Magnet Designs for Spin-Qubit Quantum-Dot Devices

Single electron spins in QDs integrated with MMs are appealing as a scalable quantum computing architecture, where arbitrary quantum gates can be electrically performed. To fully explore the potential of the MM technique, here we optimize the MM design for spin control. We first simulate the MM field in the preceding experiments on spin control with MMs and clarify requirements for high-fidelity rotations via ESR. We then examine closely the misalignment effects which were not attentively treated previously, and propose a design scheme that realizes a befitting MM stray field in the presence of realistic fabrication errors. We further discuss uses of the inhomogeneous MM fields for other types of qubit operations.

4.1 Introduction

Single-qubit manipulations of single-spin qubits are commonly performed by ESR. ESR can be driven by effective oscillating magnetic fields, whose frequency is consistent with the electron's Zeeman energy. Rotations via ESR of a single electron spin have been realized in several ways in GaAs-based lateral QDs [21, 45, 66, 68]. For practical purposes, electrical drive is favorable, which

however requires some indirect coupling between spin and electric fields [62]. A slanting magnetic field induced by proximal MMs offers such a driving mechanism (MM-ESR) [20, 21], which can coherently rotate spins at above 10 MHz in GaAs QDs [69]. This technique is highly scalable [63] and is applicable to QDs fabricated in materials with longer electron spin coherence times, e.g. nuclear-spin-free semiconductors [103].

In MM-ESR, two properties of the magnetic field are mainly utilized: a gradient of the magnetic field component normal to the spin quantization axis, b_{sl}, and a difference in the Zeeman field between QDs, ΔB_{Z} (see §3.3.2). The slanting field b_{sl} hybridizes the electron's spin and orbital degrees of freedom and allows electrically driven ESR. The local Zeeman field difference ΔB_{Z}, on the other hand, yields different resonance frequencies from dot to dot and allows access to a single spin without flipping others. The values of these magnetic field properties, b_{sl} and ΔB_{Z}, are heavily dependent on the MM shape, device geometry and QD positions. Therefore, MM shapes need to be tailored so that the stray field suffices for spin-qubit experiments [63, 104].

4.2 Field Simulation of Previous Micro-Magnet Designs

In order to refine MM-ESR performance, various MM designs have been employed in previous GaAs DQD devices for MM-ESR [21, 72, 105] (Fig. 4.1). In each device two ESR peaks, corresponding to left and right spins, are observed with a separation larger than the nuclear field fluctuations, which demonstrates control addressability in this scheme. Our interest after these proof-of-principle experiments is how much stray field can be induced by MMs and how efficiently spins can be controlled with this technique.

ΔB_{Z} gives a readily-accessible measure of inhomogeneous MM fields, as it can be directly extracted from the ESR peak spectra. The exact values of b_{sl}, on the other hand, are somewhat more difficult to evaluate experimentally. Although the value of the ESR Rabi frequency f_{R} is reflected in the ESR peak height [69, 106] or can be measured directly from time-resolved ESR experiments, it alone does not allow us to extract b_{sl} directly. This is because f_{R} is

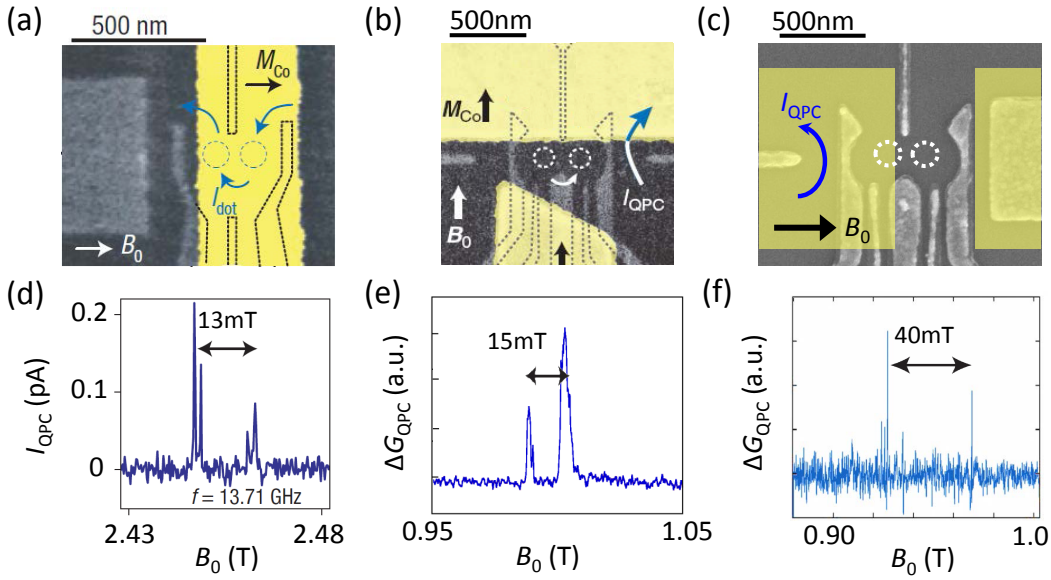

Figure 4.1: Previous MM-ESR experiments. (a)-(c) Scanning electron micrographs of GaAs DQD devices with Co MMs on top adopted from ref. [21] (a), ref. [72] (b), and ref. [105] (c). These DQDs are defined by negatively biasing Schottky metal gates deposited on a GaAs/AlGaAs HEMT wafer. The 2DEG is 90 nm below the substrate surface. A $\sim$ 100 nm thick Co ferromagnet (shown in bright yellow) is deposited on a $\sim$100 nm thick insulating Calixarene layer and are magnetized under an in-plane external magnetic field, $B_0 \gtrsim 1$ T, much larger than the coercive field. The direction of the external field is indicated by an arrow. Lift of spin blockade is detected by measuring either a transport current through a DQD ((a)) or a QPC ((b),(c)). (d)-(f) ESR spectra measured in these devices. Spins are rotated under a.c. gate-voltage excitation when the excitation frequency matched their Larmor frequency.

proportional to both $b_{\rm sl}$ and $E_{\rm ac}$, the amplitude of the microwave field. From Eq. (3.16), in MM-ESR

$$f_{\rm R} \approx \frac{|g|\mu_{\rm B} e E_{\rm ac} b_{\rm sl}}{2m^* {\omega_0}^2} = \frac{|g|\mu_{\rm B}\hbar^2 e E_{\rm ac} b_{\rm sl}}{2m^* {\Delta_{\rm ST}}^2}. \tag{4.1}$$

$\Delta_{\rm ST}$ can be evaluated relatively easily from bias spectroscopy (see §2.3.1). The only unknown parameter $E_{\rm ac}$ other than $b_{\rm sl}$ cannot simply deduced from the microwave power at the source and the line attenuation due to frequency-dependent transmission property of the feed line inside a dilution refrigerator in the experiments. Instead, it can be evaluated for instance from PAT measurements [33, 66]. However, it is a bit involved and performed only in the first MM-ESR device [21, 69].

We therefore numerically simulate MM field properties, $b_{\rm sl}$ and $\Delta B_{\rm Z}$, of the MMs employed in the previous MM-ESR experiments[1]. In the simulation we assume that the MM is magnetized uniformly in the direction of the in-plane external field ($\parallel \hat{z}$). To fully simulate real experimental conditions, we allow for a 75 nm misalignment of the MM pattern with respect to the QDs in both lateral directions. Such MM-QD misalignment is possibly present in the real devices due to imperfect overlay in the fabrication process, and errors in the QD confinement potential simulation (QDs may not be formed exactly at the expected positions). Table 4.1 compares simulated and observed values of $b_{\rm sl}$ and $\Delta B_{\rm Z}$. Two figures for each entry of simulated values are maximum and minimum in the presence of MM-QD misalignment. Throughout this work, we assume that the inter-dot distance is 150 nm and the Co magnetization is 1.8 T in the simulation. Other device-dependent parameters are the same as in the real experiments (specified in the table note).

Agreement with experimental observation supports the validity of our simulation. Evident from the table is that small displacement on the order of 75 nm can largely spoil MM field properties. We also learn that different MMs show different misalignment susceptibility. These results strongly suggest that in designing MMs the effect of MM-QD misalignment, so far treated only lightly, should be taken into account properly. Even in the presence of displacement,

[1]For MM field calculations we use Mathematica Radia package available at http://www.esrf.fr/.

Table 4.1: Simulated and observed MM field properties of MMs employed in previous MM-ESR experiments and those of the proposed design.

	simulation [a]			observation	
	larger b_{sl} [mT/nm]	smaller b_{sl} [mT/nm]	ΔB_{Z} [mT]	b_{sl} [b] [mT/nm]	ΔB_{Z} [mT]
ref. [21] [c]	0.51, 0.46	0.50, 0.0	61, −9.2	0.8	13 ± 2
ref. [72] [d]	0.67, 0.51	0.62, 0.48	11, 6.3	–	15 ± 5
ref. [105] [e]	0.62, 0.48	0.48, −0.15	84, 31	–	40 ± 5
this work [f]	1.53, 1.11	1.46, 0.90	48, 21	–	80 ± 20

[a] Maximum and minimum values within the 150 nm × 150 nm region, centered at the designed QD position.

[b] In most experiments b_{sl} is not extracted (at least directly) from experimental results. This is because its extraction requires another type of experiment to evaluate E_{ac} (see the main text).

[c-f] The thickness of the Co MM is 70, 160, 160, 250 nm and the vertical distance between the bottom of the MM and the 2DEG constituting QDs is 170, 170, 210, 140 nm for c, d, e and f, respectively.

all MMs are shown to roughly satisfy a set of conditions $b_{\mathrm{sl}} \gtrsim 0.4$ mT/nm and $\Delta B_{\mathrm{Z}} \gtrsim 10$ mT in the simulation. Together with the experimental outcomes (Figs. 4.1(d)-(f)), we conclude that this is a sufficient condition to observe and discern individual ESR peaks in GaAs QDs.

4.3 Required MM Field Properties

Realizing faster ESR rotations is a key to quantum computation in this system, since single-qubit gates are by far the most time-consuming operations in the universal gate set. $f_{\mathrm{R}} > 50$ MHz would be necessary to perform even a small number of ESR π pulses within T_2^*, a few tens of ns [60]. Then the condition for implementing nontrivial quantum circuits would be severer than the above condition for ESR detection in the following ways.

First, larger b_{sl} is necessary. From Eq. (4.1), $f_{\mathrm{R}} > 50$ MHz corresponds to $b_{\mathrm{sl}} \gtrsim 0.8$ mT/nm if we plug in typical values in GaAs QDs: $g = -0.40$, $E_{\mathrm{ac}} = 5$ μV/nm, $m^* = 0.067 m_0$ and $\Delta = 0.5$ meV, where m_0 is the mass of a free electron [66, 69]. We note that the upper bound on E_{ac} is set by photon-

assisted-tunneling (PAT), which leads to state leakage [21,33]. Therefore, there could be room for further improvement in this aspect by refining QD gate designs, microwave frequency and so on.

Secondly, larger ΔB_{Z} is needed as well for addressable single-spin control, if ESR rotations become faster. Indeed, from simple analysis, the required ΔB_{Z} gets larger proportionally to f_{R} in the strong driving regime where $f_{\mathrm{R}} \gg 1/T_2^*$. The reason is that the resonance peak is broadened by nature under strong drive [59,106]. In the weak driving limit, ESR spectral width is predominantly broadened by the statistical fluctuations of the Overhauser field. Assuming that fluctuations follow the Gaussian distribution and the nuclear spin dynamics is sufficiently slow, a full width at half-maximum (FWHM) of inhomogeneously broadened ESR spectra would be

$$\delta f_{\mathrm{ESR}}^* = 2\sqrt{2\ln 2}|g|\mu_{\mathrm{B}}\sqrt{\langle (B_{\mathrm{N},z})^2\rangle}/h. \tag{4.2}$$

From Eq. (3.22), one would expect that $\delta f_{\mathrm{ESR}}^* = 4\sqrt{\ln 2}\pi/T_2^*$. However, in reality, ESR linewidths observed experimentally are typically wider even for small f_{R}, due to DNP [45, 97, 98]. In the strong driving regime, we have to take into account the fact that spins can be rotated even if the excitation frequency is slightly detuned from resonance. From the Rabi formula (Eq. (3.9)), the maximum spin flip probability for frequency detuning δf_{ac} is given by a Lorentzian profile, ${f_{\mathrm{R}}}^2/\left({f_{\mathrm{R}}}^2 + {\delta f_{\mathrm{ac}}}^2\right)$, which alone yields the FWHM of the ESR spectrum, $\delta f_{\mathrm{ESR}} = 2f_{\mathrm{R}}$. Combination of these contributions gives the so-called Voigt profile [100], with the FWHM width approximated as [107]

$$\delta f_{\mathrm{ESR}} \approx 1.07 f_{\mathrm{R}} + \sqrt{0.858{f_{\mathrm{R}}}^2 + {\delta f_{\mathrm{ESR}}^*}^2}. \tag{4.3}$$

The above expression is valid only when the assumption of Gaussian broadening by nuclear spins holds. In the limit of strongly driven ESR, however, δf_{ESR} is expected to be $\approx 2f_{\mathrm{R}}$, irrespective of the actual dynamics of the nuclear bath. Supposing Rabi frequencies are more or less the same in all QDs, fast yet addressable ESR is only possible when $|g|\mu_{\mathrm{B}}\Delta B_{\mathrm{Z}} > 2f_{\mathrm{R}}$. This corresponds to $\Delta B_{\mathrm{Z}} > 18$ mT for $f_{\mathrm{R}} = 50$ MHz in GaAs QDs with $|g| = 0.40$.

Third, MMs should be tolerant of a finite relative misalignment. MM-QD

misalignment is practically inevitable in real devices; it can arise from overlay fabrication errors and inaccurate estimation of QD positions. This distance is difficult to reduce, especially for a multi-qubit system, typically below 50-100 nm even with the state-of-the-art semiconductor processing technology. Its effect must be taken into serious consideration since as seen from Table 4.1, this amount of displacement can spoil the MM properties. This may not be surprising given that small dimensions of MMs tend to produce a fine spatial distribution of the stray field.

4.4 Novel Micro-Magnet Design

In what follows, we optimize the MM design to meet all requirements for implementing quantum circuits in GaAs QDs clarified above:

$$\begin{aligned} &\text{(i)} \quad b_{\mathrm{sl}} \gtrsim 0.8 \text{ mT/nm} \\ &\text{(ii)} \quad \Delta B_{\mathrm{Z}} > 18 \text{ mT} \\ &\text{(iii)} \quad \text{75 nm misalignment robustness, i.e. conditions (i) and (ii)} \\ &\qquad\quad \text{are satisfied in the presence of 75 nm MM-QD misalignment.} \end{aligned} \tag{4.4}$$

4.4.1 Classification of Micro-Magnet Designs

There are two general types of simple MMs, a *single MM* and a *paired MM* (Fig. 4.2(a)). The shape of a single MM can be specified by a length $l_{\mathrm{MM}}(y)$ measured in the magnetization direction ($\parallel \hat{z}$), as a function of y. The design of a paired MM can be specified likewise by a gap opening $d_{\mathrm{gap}}(y)$. When $d_{\mathrm{gap}}(y) = l_{\mathrm{MM}}(y)$, these MMs produce the same stray fields with the opposite sign except near the edge. They can be considered equivalent as far as MM field properties in the core region are concerned. Therefore, in the following we mainly discuss the design of a paired MM only, with a notion in mind that the same discussion can in principle be directly applied to an equivalent single MM. We note that the sign of the stray field can make a difference if SOI comes in. SOI can add to or partially cancel the effective slanting field that mediates MM-ESR [21]. Only with a paired MM, can we fully utilize both Rashba and Dresselhaus contributions in GaAs QDs by applying a.c. electric fields along

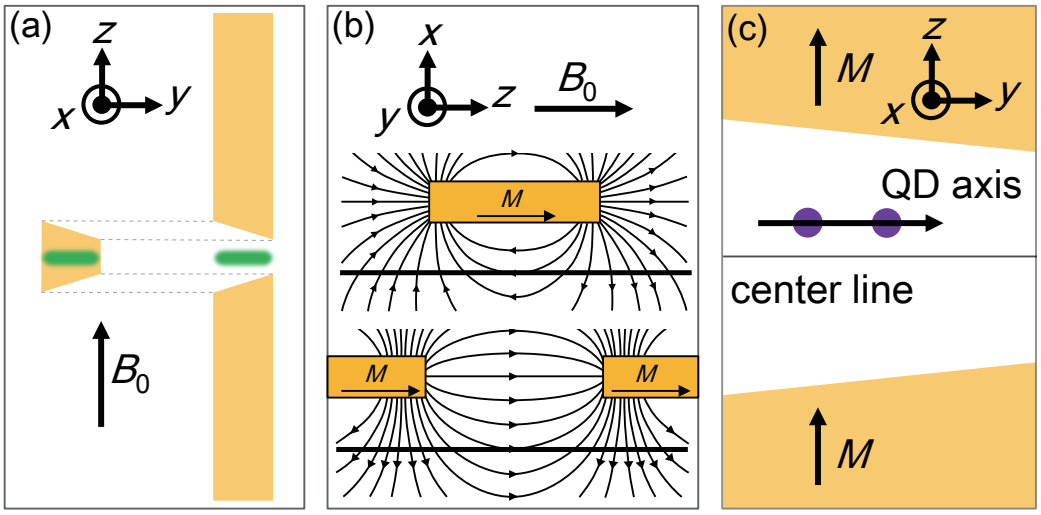

Figure 4.2: Equivalent MMs and axis definition. (a) Top views of two equivalent MMs, a single MM (left) and a paired MM (right). The region where b_{sl} is large (in the 2DEG plane) is schematically highlighted in green. (b) Schematics of magnetic lines of force around MMs. A single MM and a paired MM yield equivalent but opposite fields. (c) Definition of the QD axis and the MM center line, shown in a zoom-in image of the core region of a paired MM. QD positions are shown by purple dots and a MM is colored orange. The QD axis is defined by a line that connects QDs. The MM center line defines the mirror-symmetry center of the MM. Here the perpendicular configuration is adopted for explanation (see the main text).

the [110] crystal axis [63].

MM designs can be divided further into two types with respect to the angle of the magnetization axis and the QD axis (see Fig. 4.2(c) for definition). In the first type of MMs these axes are aligned, as in Figs. 4.1(a) and (c), which we denote as the *parallel configuration*. In this configuration, ΔB_{Z} can be obtained by positioning a MM slightly off the DQD center. It is relatively easy to make ΔB_{Z} large, by simply shifting the MM position. In the other type, the axes are normal to each other as in Fig. 4.1(b), which we denote as the *perpendicular configuration*. In this configuration, tapered MMs whose $d_{\mathrm{gap}}(y)$ linearly varies as a function of y are conventionally used to produce sufficiently large ΔB_{Z} [35, 63, 72].

4.4.2 Misalignment-Robust Slanting Field

For b_{sl} to be robust against misalignment, the perpendicular configuration proves favorable. More specifically, the tolerance of b_{sl} is large when the QD axis is on top of the MM center line. This is simply because in most relevant cases b_{sl} decays monotonously as a function of the distance from the MM center line. In the parallel configuration, the QDs are placed on average at least half the inter-dot distance away from the MM gap center.

To learn more about misalignment robustness of b_{sl}, we analyze the spatial distribution of b_{sl} induced by a paired MM with a constant gap width. In general, b_{sl} is much more susceptible to displacement in the magnetization direction than in the other direction. Figure 4.3 shows the gap dependence of b_{sl} field distribution in the magnetization direction produced by a parallel, paired MM. From the contour plot we see that there is an optimal range of MM gap width to maximize the guaranteed b_{sl} in the presence of misalignment. A smaller gap will make b_{sl} more susceptible to misalignment, whereas a larger gap will weaken b_{sl} at the gap center. This appropriate range of gap width is typically 250 - 400 nm for realistic device parameters and for 75 nm misalignment.

Tapering MMs is a convention to obtain finite ΔB_{Z} in the perpendicular configuration, as mentioned before. The simulation reveals, however, that this can harm b_{sl} robustness if not properly done. This can be understood by applying the notion of the appropriate range of gap width, introduced above for parallel MMs, to tapered ones: if the gap width exceeds the range, b_{sl} will become either small or displacement-sensitive. The problem is that ΔB_{Z} cannot be large enough if the change of the gap width is limited within the range. The tapered-MM method does not seem to simultaneously satisfy the condition for misalignment-robust b_{sl} and that for sufficiently large ΔB_{Z}.

4.4.3 Bridge Structure

So far we have seen the following relationships between MM design and the field properties. A (nearly) constant gap width is favorable for large, robust b_{sl}. However, to obtain ΔB_{Z} with almost parallel MMs, only the parallel configuration can be used, which makes b_{sl} small at least at one of the QD positions (Fig. 4.4(a)). By contrast, if the gap is strongly tapered to achieve sufficiently

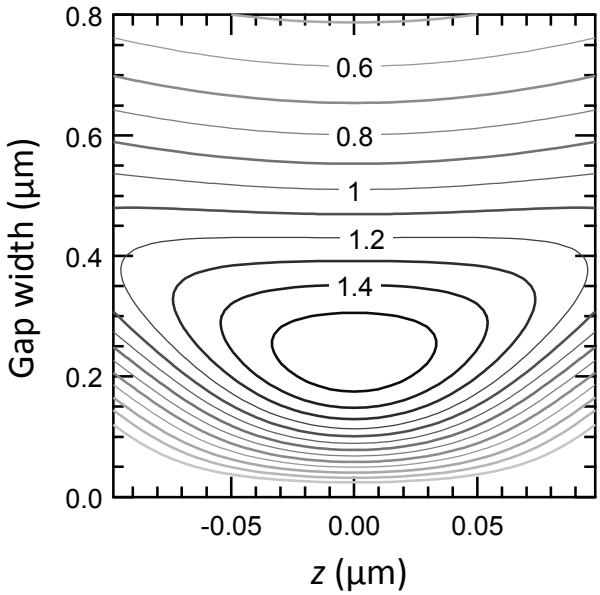

Figure 4.3: Contour plot of b_{sl} by a paired MM with a parallel gap. Unit of the labels is mT/nm. Calculation is done for a 250 nm thick, 1 μm wide Co MM, deposited 140 nm above the 2DEG. z is the direction of magnetization. For this parameter set, by choosing a gap width from the range of approximately 250 - 400 nm, $b_{\mathrm{sl}} > 1.2$ mT/nm even in the presence of 75 nm misalignment in the magnetization direction. Gaps smaller than ~ 250 nm will make b_{sl} susceptible to 75 nm misalignment. On the other hand, gaps larger than ~ 400 nm will produce smaller b_{sl} even at the gap center.

large ΔB_Z in the perpendicular configuration, b_{sl} will be prone to misalignment (Fig. 4.4(b)).

This dilemma can be lifted if there is a way to provide ΔB_Z even with a constant gap width. Here we propose a *bridged MM* as such a mechanism. A bridged MM consists of two parts: a parallel, paired MM which produces large, robust b_{sl}, and a bridge MM on one side that connects the parallel MM pair and induces a large inhomogeneous Zeeman field (Fig. 4.4(c)). A bridge part of MM can be considered also as an effectively "negative" gap as it creates the Zeeman field as well as the slanting field opposite to that induced by the rest with a "positive" gap. This change in sign causes an abrupt change of

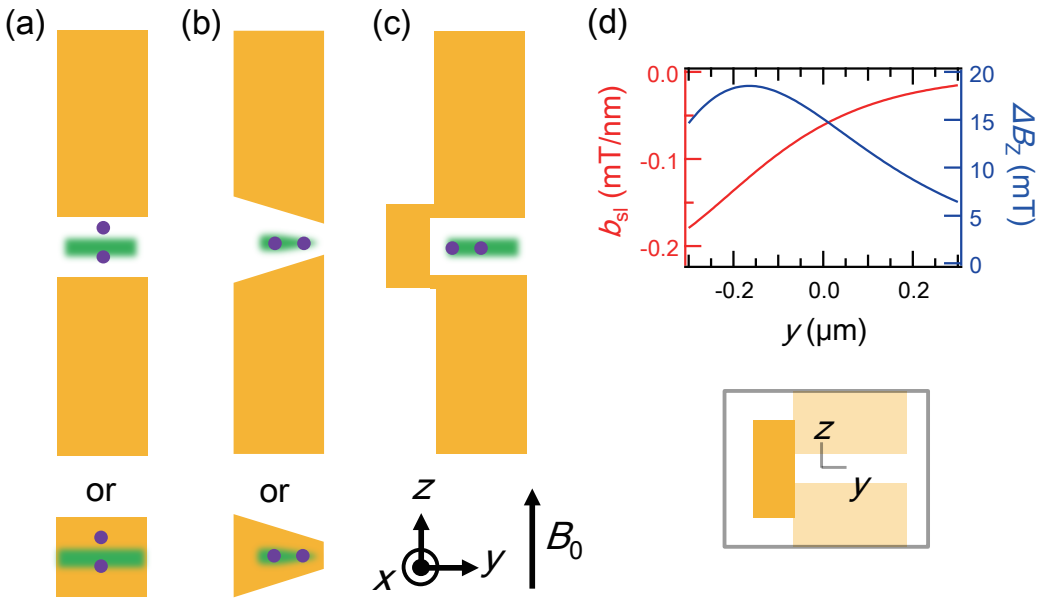

Figure 4.4: Various MM design schemes and a MM bridge. (a) Parallel MMs. QDs have to be arranged in the parallel configuration for ΔB_Z. (b) Tapered MMs. QDs can be arranged in the perpendicular configuration. (c) A bridged MM. Parallel MM pairs are linked on one side by a rectangular MM. QDs are supposed to be arranged in the perpendicular configuration. (d) Simulated field property arising from a bridge part alone. $|b_{sl}|$ and ΔB_Z are plotted as a function of y of the QD position, and of the DQD center, respectively. In the range of $|y| < 150$ nm where the QDs are located, decrease in the total $|b_{sl}|$ decays < 0.12 mT/nm ($= 15\%$ of the required value). In the range of $|y| < 75$ nm where the DQD center is located, $\Delta B_Z > 12$ mT ($= 67\%$ of the required value). The inset schematically shows the bridge part in dark orange.

the Zeeman field distribution and hence large ΔB_{Z} can be produced among QDs. Since ΔB_{Z} decays slower as a function of distance, putting a bridge MM does not influence b_{sl} severely while supplying enough ΔB_{Z}, if properly done (Fig. 4.4(d)).

Figure 4.5(a) shows the optimized MM design for specific device parameters. The constant gap of a split-pair part is chosen to maximize the minimum b_{sl} within 75 nm from the MM center line, so that b_{sl} becomes misalignment-proof by design. The position and the size of the bridge are chosen to keep $\Delta B_{\mathrm{Z}} >$ 18 mT in the presence of 75 nm misalignment with care taken not to spoil b_{sl} too badly. Figures 4.5(c) and (d) show the simulated spatial distribution of the magnetic field properties. Within a 150 nm $\times$ 150 nm area, b_{sl} is larger than 0.9 mT/nm for both QDs and ΔB_{Z} is larger than 19 mT, meaning that the set of conditions for realizing fast addressable ESR rotations, Eq. (4.4), is satisfied with this MM design.

4.5 Other Types of Qubit Operations

The MM technique offers many other electrical control knobs of spin other than MM-ESR. One such example is a single-step phase rotation by the spatial distribution of the Zeeman field within a single QD, δB_{Z}. This is theoretically discussed in more detail and experimentally demonstrated in Chapter 7. Another example is a CPHASE gate via ΔB_{Z} as discussed in §3.4. We would like to note that bridged MMs can be also designed to supply ΔB_{Z} exceeding 50 mT by tuning the bridge position. This brings a single-step CPHASE operating at $\sim$20 MHz within experimental reach in GaAs QDs [71]. ΔB_{Z} can also be used for single-spin readout with PAT [108]. Possible uses of the MM field properties in spin-qubit experiments are summarized in Table 4.5.

Throughout this chapter we implicitly assume that ESR rotations are performed at all QDs, but this is not truly mandatory. Another approach is also possible, in which fast ESR rotations are performed in only some of the QDs (e.g. every other QDs) and single-qubit gates in other QDs are implemented by combining high-fidelity SWAP operations. This may well be worth consideration since SWAP gates generally operate much faster and it is much less demanding if large b_{sl} is required in only some of the QDs. However, one must

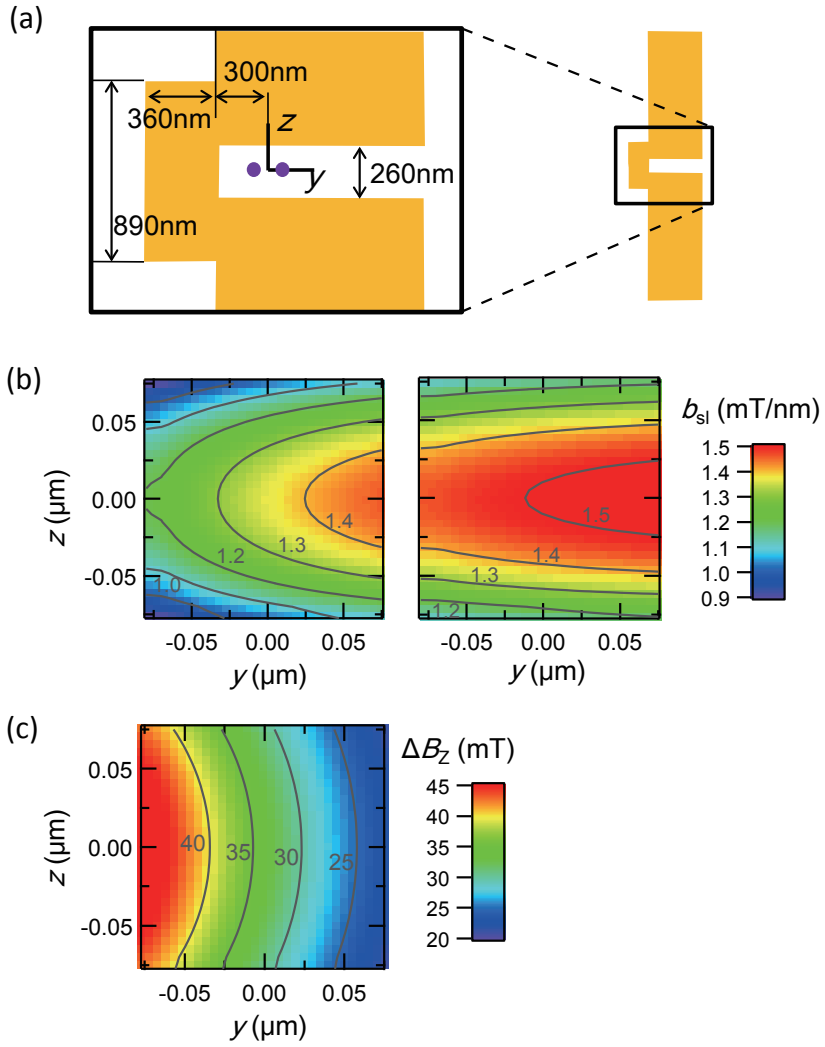

Figure 4.5: Proposed MM. (a) Design of a bridged MM optimized for a 250 nm thick Co MM deposited 140 nm above the 2DEG. (b) Spatial distribution of b_{sl} near the left and right QDs. b_{sl} is smaller at the left QD position, as it is partially canceled by the bridge part. (c) Spatial distribution of ΔB_Z as a function of MM-QD misalignment. The bridge part as well as the absence of the parallel split part produces ΔB_Z, which as a result is larger on the left side.

Table 4.2: Properties of MM-induced inhomogeneous magnetic fields that can be utilized for spin-qubit experiments

Magnetic field resources	Operation
Slanting magnetic field, $b_{\mathrm{sl}} = \mathrm{d}B_x/\mathrm{d}z$	ESR (X, Y gates)
Intradot Zeeman field difference, δB_{Z}	Single-step Z gate
Interdot Zeeman field difference, ΔB_{Z}	ESR addressability
	Single-step CPHASE
	Spin-selective PAT readout

be reminded that in this approach dynamical decoupling pulses [9, 59, 88, 109] cannot be applied simultaneously on all qubits, and dephasing rates can change for different operations. To conclude which approach is better in real experiments would involve evaluation of gate fidelity and process tomography [9, 48], which are not fully performed in this system yet.

4.6 Summary

In this chapter, requirements on MM stray fields for high-fidelity spin manipulations are discussed, and a novel design scheme to satisfy them is presented. It is shown that misalignment robust b_{sl} and ΔB_{Z} can be produced by employing a parallel MM and a bridge MM, respectively. Proposed bridged MM produces $b_{\mathrm{sl}} > 0.9$ mT/nm and $\Delta B_{\mathrm{Z}} > 19$ mT for realistic device parameters even when the MM is 75 nm misaligned. This MM design is expected to facilitate fast addressable ESR ($\gtrsim 50$ MHz) and other quantum gates requiring multiple ESR pulses. The MM field property can further be enhanced by bringing the MM closer to the QDs as well as by using a material with stronger magnetization than Co.

In the experiments described in the following Chapters 5, 6, 7 and 8, MMs of the proposed design are incorporated to DQD and TQD devices. The effectiveness of the bridged-MM design is validated also in these experiments.

Chapter 5

Single Electron Spin Resonance in a Large Inhomogeneous Magnetic Field

Electron spin in QDs [6] is a promising candidate for implementing qubits in a quantum computer [40–42] owing to its long coherence time [60, 88, 110] and potential for scalability. Experiments based on GaAs quantum dots have so far realized two fundamental building blocks for universal quantum gates: defining spin-1/2 qubits via single electron-spin-resonance (ESR) [21,45,66,68], and controlling the entanglement through inter-dot exchange coupling [53, 72]. In contrast to a large, tunable Heisenberg interaction between neighboring spins [17], however, it remains a big technical challenge to obtain strong magnetic fields to manipulate single spins within the time-ensemble phase coherence time (T_2^*). Here we demonstrate that strongly inhomogeneous magnetic fields induced by a tailored micro-magnet (MM) can realize fast arbitrary single-spin rotations up to 127 MHz, with a fidelity exceeding 95 %.

5.1 Introduction

In the system of single-spin qubits with QDs, ESR rotations that, at present, are comparably slow with respect to the dephasing present a severe limitation on the number of single-qubit gates in implementing quantum circuits. This

is in the first place because large a.c. magnetic fields are difficult to produce locally on chip in a dilution refrigerator. This problem can be overcome by coupling the gate-driven electron motion with an inhomogeneous magnetic field that is produced for example by a proximal MM (we refer to this technique as MM-ESR henceforth) [20, 21]. From simulation (see Chapter 4), it is expected that by properly preparing MMs a Rabi frequency f_{R} as large as 50 MHz (corresponding to 20 mT a.c. magnetic field) is readily achievable in GaAs QDs. This would greatly improve the single-qubit gate fidelity $\mathcal{F}$ (so far $\mathcal{F} = 73\%$ is reported with $f_{\mathrm{R}} \approx 10$ MHz in GaAs QDs in ref. [45]) and therefore the ease of demonstrating small-scale quantum circuits, including CNOT and state tomography as important examples.

MM-induced inhomogeneous magnetic fields are also appealing as sources of other qubit operations such as electrical gating of spin rotations [111] (see also Chapter 7), one-step CPHASE [71] and nondestructive multiple spin readout [108].

5.2 Device and Setup

5.2.1 Device Design

Figures 5.1(a) and (b) illustrate the DQD device structure used in the experiment. The MM is designed such that both in- and out-of-plane components of the stray field are largely slanted while their gradients depend only moderately on geometrical misalignment of the QD and MM of ~ 75 nm, which is inevitable in real devices. In the numerical simulation we see that the slanting field that mediates MM-ESR, $b_{\mathrm{sl}} \equiv \partial B_x/\partial z \approx 1.2$ mT/nm while $\partial B_z/\partial y \approx 0.3$ mT/nm, and $\partial B_z/\partial z \approx 1.0$ mT/nm (Figs. 5.1(b) and (c)). In MM-ESR f_{R} is proportional to the product of the magnetic field gradient b_{sl} and the amplitude of the a.c. electric field E_{ac} that oscillates an electron inside the QD, as seen from Eq. (4.1). Therefore, to maximize f_{R}, both b_{sl} and E_{ac} need to be large. To obtain large inhomogeneous magnetic fields, we employ an AlGaAs/GaAs HEMT wafer with a shallow 2DEG (57 nm below the surface) and reduce the distance between the MM and QDs. In addition, the thickness of the Co MM (250 nm) is more than twice as thick as those in previous MM-ESR devices [21, 72]. In

order to make $E_{\rm ac}$ as large as possible, the two QDs are "parallel"-coupled to gate electrode C, to which a microwave (MW) is applied. This is because for the two QDs "tandem"-coupled to the MW gate the photon-assisted-tunneling (PAT) [33] imposes a severe upper limit on $E_{\rm ac}$ [32, 112].

5.2.2 Measurement Setup

On gate C, both sinusoidal MW (a few GHz) and square, pump-and-probe pulse are applied, which are generated from different instruments, Agilent E83650B and Tektronix AWG520, respectively. MW from E83650B is switched with a commercial PIN switch that is synchronously triggered by AWG520, and combined with the pump-and-probe pulse from AWG520 at room temperature. E83650B is operated in the pulse modulation mode if high switching isolation ($>$ 30 dB from PIN switch alone) is necessary under strongly driven ESR. After passing through SMA coaxial lines inside the dilution refrigerator with 3×3 dB attenuators, the high-frequency pulse is added to the d.c. gate voltage with a commercial, 50 Ω-matched bias-tee at the mixing chamber plate. The device is connected via bonding wires to an order-made chip carrier with two coplanar-wave guides inside a home-made sample holder with two sliding contacts. During cool down positive voltages are applied on the surface gates and at the base temperature $\sim$ 100 mK the MM is negatively biased (as a global top gate) to reduce charge noise [113, 114].

To improve the signal-to-noise ratio, a lock-in trans-conductance technique is used throughout experiment. A 216 Hz voltage excitation is applied to the gate R, and the moulated current through a nearby QPC, $I_{\rm QPC}$, is homodyne-detected with a lock-in amplifier to obtain charge sensing signals proportional to the QPC current derivative, $\mathrm{d}I_{\rm QPC}/\mathrm{d}V_{\rm R}$. The R gate is chosen since in terms of dynamic reserve of the lock-in signal, it is better to make the gate lever-arm to the relevant transition (in our case the inter-dot tunneling) large compared with that to the QPC channel. We note that in this experiment due to instability of the device the trans-conductance signal is not stable enough to extract the absolute charge configuration probability.

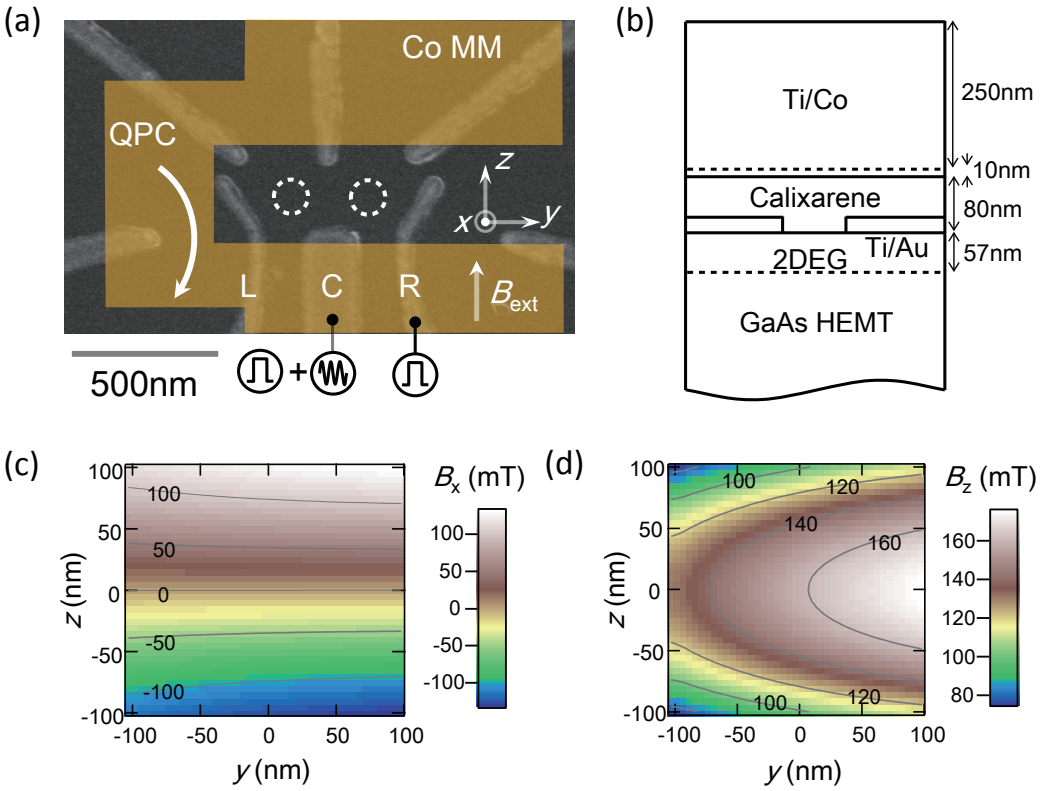

Figure 5.1: Device structure and simulated stray fields. (a) Scanning electron micrograph image of a similar device. The coordinate system used in the main text is also shown. The y-axis is along the coupling direction of the QDs and the x-axis is normal to the 2DEG plane. The shape of a Co MM is drawn in orange. We choose the z-axis along the crystallographic direction of [110] because the spin-orbit interaction then provides a local a.c. magnetic field to be added to b_{sl} for the ESR rotation [63]. High frequency pulses are applied on gates C and R and MW is irradiated solely on C. Both the external magnetic field and the a.c. electric field are applied in the z direction. (b) Layer structure of the QD device. The Co MM and the wafer surface are separated by $\sim$ 90 nm by an insulator (Calixarene) and a Ti adhesive layer. (c) Numerically simulated distribution of the x component of the stray field. The origin of the QD plane is taken at the center of the two QDs. (d) Numerically simulated distribution of the z component of the stray field, or the local Zeeman field.

5.3 Continuous-Wave ESR Measurements

5.3.1 Observation of a Large ESR Peak Separation

To detect spin signals, the device is tuned to the Pauli spin blockade (PSB) regime near the (1,1)-(2,0) charge boundary (see §3.2.2). We here apply a source-drain bias $V_{\mathrm{SD}} = 0.5$ mV (the chemical potential of the right lead is energetically higher than that of the left). Since we measure the derivative of the QPC current, $\mathrm{d}I_{\mathrm{QPC}}/\mathrm{d}V_{\mathrm{R}}$, PSB manifests itself as the disappearance of the charge transition line at zero level-detuning, where $\varepsilon = 0$ [115]. At zero external magnetic field, B_{ext}, and with the exchange coupling small enough, PSB is lifted by nuclear fluctuation [14]. All three (1,1) triplet states, $|\mathrm{T}_0\rangle$, $|\mathrm{T}_+\rangle$ and $|\mathrm{T}_-\rangle$, are admixed with the (1,1) singlet $|\mathrm{S}\rangle$ by inter-dot difference of the Overhauser field; for instance, $|\mathrm{T}_0\rangle = (|\uparrow\downarrow\rangle + |\downarrow\uparrow\rangle)/\sqrt{2}$ evolves into $|\mathrm{S}\rangle = (|\uparrow\downarrow\rangle - |\downarrow\uparrow\rangle)/\sqrt{2}$ due to its z component, while $|\mathrm{T}_+\rangle = |\uparrow\uparrow\rangle$ and $|\mathrm{T}_-\rangle = |\downarrow\downarrow\rangle$ evolve into $|\mathrm{S}\rangle$ due to its in-plane components. In this condition, charge transport through the DQD makes the time-average charge configuration inside the bias triangles different from (1,1), making the zero-detuning line visible in the stability diagram (Fig. 5.2(a)). When B_{ext} is much larger than the nuclear field, the triplet states with parallel spins, $|\mathrm{T}_+\rangle$ and $|\mathrm{T}_-\rangle$, are split off in energy and the admixing with $|\mathrm{S}\rangle$ becomes negligible. Since these (1,1) triplets cannot tunnel to (2,0) states due to the Pauli exclusion principle, the transport is stuck in the (1,1) charge state for a long time. Then the time-average charge configuration in the bias triangles is almost (1,1), resulting in an invisible zero-detuning line (Fig. 5.2(b)).

After tuning to the PSB region, we apply MW to gate C under a large B_{ext} (> 0.5 T in most cases, but 50 mT is sufficient for PSB and MM-ESR depending on DQD parameters) to drive MM-ESR. ESR takes place when the MW frequency f_{MW} is equivalent to the electron Zeeman energy, $hf_{\mathrm{MW}} = |g|\mu_{\mathrm{B}}(B_{\mathrm{ext}} + B_{\mathrm{MM},z})$ with $B_{\mathrm{MM},z}$ the local Zeeman field induced by the MM. We rely on the PSB effect to detect ESR: the blockade is only lifted by ESR, to generate a transition of the charge state to the (2,0) state. This change of charge configuration is detected by monitoring $\mathrm{d}I_{\mathrm{QPC}}/\mathrm{d}V_{\mathrm{R}}$ at $\varepsilon = 0$.

Figure 5.3 shows the observed ESR signals ($\propto \mathrm{d}I_{\mathrm{QPC}}/\mathrm{d}V_{\mathrm{R}}$ at $\varepsilon = 0$) under

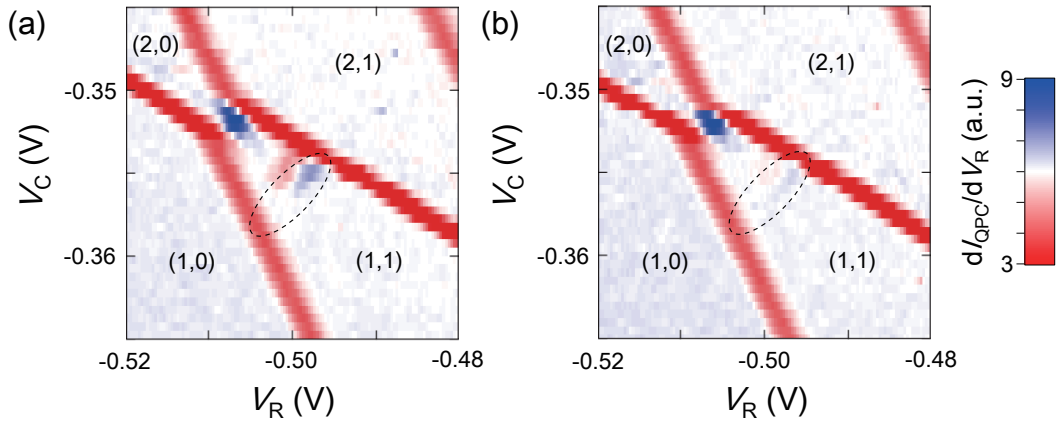

Figure 5.2: Observation of PSB. (a) Stability diagram at $B_{\text{ext}} = 0$. We sweep the voltage of gate R, V_{R}, and that of gate C, V_{C}, to facilitate pump-and-probe measurements described later (these are the only gates to which high-frequency pulses can be applied in our setup). The zero detuning line is bright as the transport inside the bias triangle is not blocked. Signal is stronger for the hole transport cycle, related to the QPC sensitivity ratio of the left and right dots, and the ratio of tunneling rates (see Appendix B for further discussion on device tuning and expected signals). (b) Stability diagram at $B_{\text{ext}} = 0.5$ T, in the same gate-voltage condition as (a). The zero detuning line disappears due to thick center tunneling barrier, indicating that the Zeeman-split parallel spin states are stuck in the (1,1) charge configuration.

continuous-wave (CW) MW excitation when f_{MW} is swept and B_{ext} is stepped. Two ESR peaks are clearly observed at two different f_{MW} separated by $\approx$ 440 MHz, which corresponds to ≈ 80 mT. Based on the MM field distribution, the peak at lower (higher) frequency is attributed to the ESR signal from the left (right) spin. Since these peaks are almost parallel we attribute this separation to the local Zeeman field induced by the MM, not the difference of g-factor [116]. Indeed, from fitting we obtain almost the same g-factors, $|g| = 0.331 \pm 0.004$ for the left spin and $|g| = 0.334 \pm 0.004$ for the right spin. The peak separation is larger by more than a factor of 5 than that observed in the previous MM-ESR experiments, indicating enhancement of the field inhomogeneity ($\partial B_z/\partial y$) by roughly the same amount. Assuming a typical value of 100 nm for the inter-dot distance, we get $\partial B_z/\partial y \sim 0.8\,\mathrm{mT/nm}$, which is consistent with the calculation. We note that this large peak separation allows independent manipulation of the two spins even when $f_{\mathrm{R}} > 120$ MHz.

5.3.2 Peak Broadening

We observe broadening of the Rabi resonance with MW power in the CW-ESR measurement (see §4.3 for a detailed theoretical description). The ESR peak widths extracted from fitting to the Voigt function grow linearly with the square root of MW power P_{MW}, indicating that $f_{\mathrm{R}} \propto \sqrt{P_{\mathrm{MW}}}$ in this range (Fig. 5.4). We evaluate the ESR peak width using the approximation of the FWHM of the Voigt profile (Eq. (4.3)) and assuming $f_{\mathrm{R}} \propto \sqrt{P_{\mathrm{MW}}}$, and derive the standard deviation $\sqrt{\langle (B_{\mathrm{N},z})^2 \rangle}$ of a Gaussian profile due to inhomogeneous broadening by extrapolating P_{MW} to 0 as shown in Fig. 5.4. We extract $\sqrt{\langle (B_{\mathrm{N},z})^2 \rangle} = 3.1$ mT, which corresponds to T_2^* of 16 ns (calculated for $|g| = 0.33$), consistent with previous measurements [17, 60]. We speculate however that this is a relatively poor lower bound on T_2^* (when B_{ext} is fixed as is the case with most spin-qubit experiments): B_{ext} sweep can pump dynamic nuclear polarization (DNP), which is evident in this data set as a shift in the peak center. DNP seems to be pronounced under CW excitation, although B_{ext} is swept downwards to suppress DNP pumping [94, 95, 97, 99].

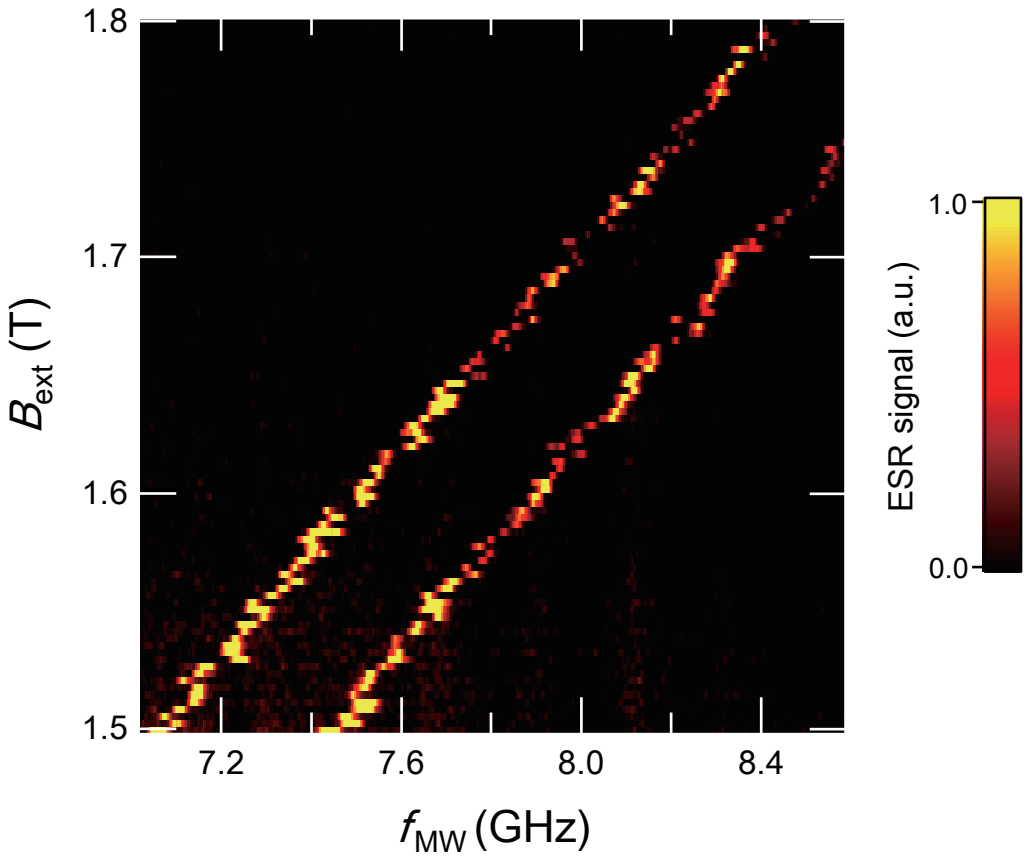

Figure 5.3: Color map of ESR signal as a function of f_{MW} and B_{ext}.

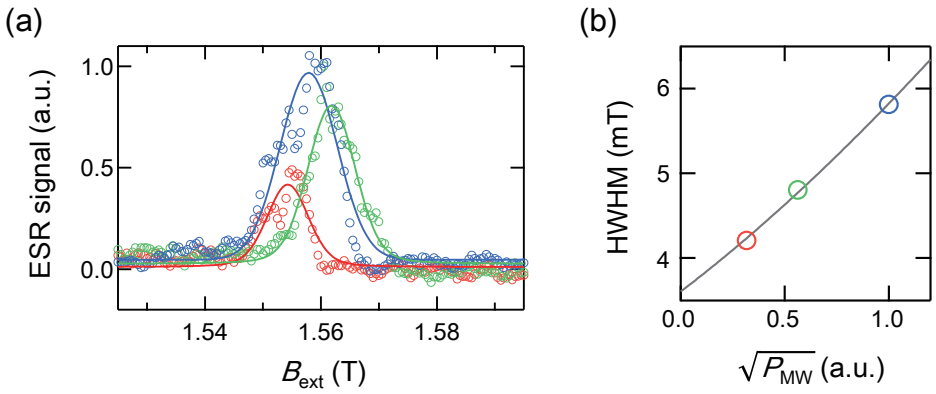

Figure 5.4: Broadening of CW ESR spectrum. (a) P_{MW} dependence of CW ESR spectrum. Each trace is an average over 5 magnetic field sweeps. Peak width as well as peak height increases with P_{MW}, which is stepped by 5 dBm in the order of red, green, blue. (b) P_{MW} dependence of ESR peak width, half-width at half maximum (HWHM). Each data point is plotted in the same color as in (a). The solid line is a fit by a function that approximates HWHM of the Voigt profile.

5.4 Time-Resolved ESR Measurements

5.4.1 Fast Rabi Oscillation

To demonstrate that driven spin rotations are coherent, we next measure the time evolution of the spin state under ESR drive, using a pump-and-probe technique. From here we focus on one of the two ESR peaks, corresponding to the right spin. First, we wait at $\varepsilon = 0$ sufficiently long to initialize the two spins in the parallel configuration, $|\uparrow\uparrow\rangle$ or $|\downarrow\downarrow\rangle$, via PSB. Without loss of generality we will henceforth assume that the initial spin state is $|\uparrow\uparrow\rangle$ for brevity. We then apply a burst of resonant MW for a time t_{MW} at $\varepsilon \sim -0.5$ meV in the (1,1) Coulomb blockade. The right spin rotates ideally about the x-axis of the Bloch sphere to $|\uparrow\downarrow\rangle$ when t_{MW} is an odd multiple of the π-flip time, $t_\pi = 1/(2f_{\mathrm{R}})$. When t_{MW} is an even multiple of t_π, the spin will flip back to $|\uparrow\uparrow\rangle$. Finally we move to $\varepsilon = 0$ and measure $\mathrm{d}I_{\mathrm{QPC}}/\mathrm{d}V_{\mathrm{R}}$, whose change is proportional to the flipping probability of the right spin. Coherent Rabi oscillations observed in the $\mathrm{d}I_{\mathrm{QPC}}/\mathrm{d}V_{\mathrm{R}}$ signal as a function of t_{MW} are plotted in Fig. 5.5(a).

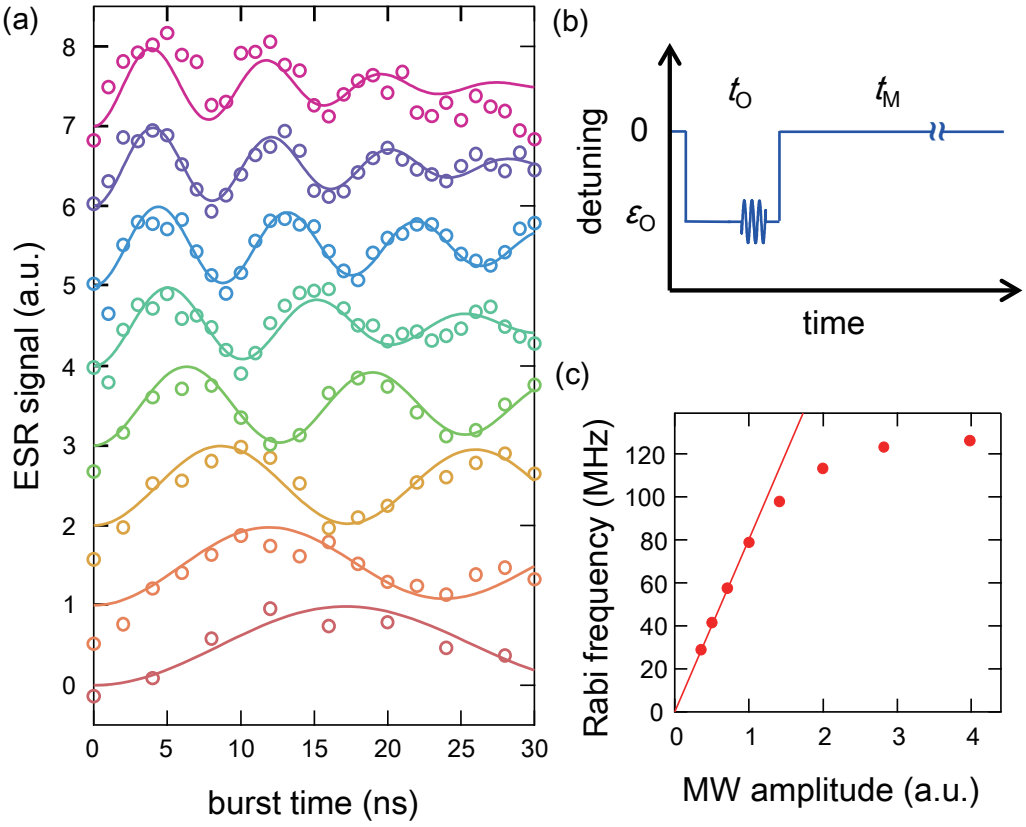

Figure 5.5: Fast Rabi oscillations. (a) Rabi oscillations measured at $B_{\text{ext}} = 0.51$ T with $f_{\text{MW}} = 3.0$ GHz. MW power is stepped by 3 dB from bottom trace to top. Traces are offset for clarity. Solid lines are fit to Eq. (5.1). (b) Pulse sequence for observation of Rabi oscillation. Spin is pumped with MW in the Coulomb blockade at a detuning $\varepsilon_O \approx -0.5$ mV, and then probed at $\varepsilon = 0$. Dwell time at $\varepsilon = \varepsilon_O$ is $t_O = 2$ μs, and dwell time at $\varepsilon = 0$ is $t_M = 80$ μs. (c) Rabi frequency vs $\sqrt{P_{\text{MW}}}$. Solid line is a guide to the eye for linear dependence.

To extract f_{R}, Rabi oscillation signals are fit to

$$P_{\mathrm{flip}}(t_{\mathrm{MW}}) = C + A\ \mathrm{e}^{-\left(t_{\mathrm{MW}}/T_{2,\mathrm{R}}\right)^2} \cos(2\pi f_{\mathrm{R}} t_{\mathrm{MW}}) \tag{5.1}$$

with f_{R} and $T_{2,\mathrm{R}}$ as fitting parameters. f_{R} increases linearly up to ~ 100 MHz with the square root of MW power P_{MW} and then progressively saturates to the value of $f_{\mathrm{R}} \sim 130$ MHz (Fig. 5.5(c)). The highest f_{R} achieved in this experiment is 127 MHz with $t_\pi = 3.9$ ns, which is the fastest spin flip ever reported in electrically-controlled semiconductor QDs (Table 3.1). We note that the spin-orbit interaction (SOI) can drive the Rabi oscillation with $f_{\mathrm{R}} \propto E_{\mathrm{ac}} \times B_{\mathrm{ext}}$ [61,65–67]. However, we speculate that the high speed Rabi oscillation obtained here is mostly due to the MM-induced inhomogeneous field, since in GaAs the SOI mechanism is not so efficient (ref. [66] reports $f_{\mathrm{R}} \sim 4.7$ MHz of SOI-ESR with $E_{\mathrm{ac}} \sim 4\ \mu$V/nm and $B_{\mathrm{ext}} \sim 3$ T). In the present device b_{sl} is estimated to be roughly 3 times larger than in the previous report. Another factor of 3 to account for the 10-fold enhancement of f_{R} can be attributed to at least 3-fold larger E_{ac} as a result of the parallel-coupled configuration (in ref. [69] where tandem-coupled configuration is used, E_{ac} is estimated to be 1.4 μV/nm).

We estimate the fidelity $\mathcal{F}$ of the initial π-flip from the ESR signal level. Here we define the fidelity between an intended state $|\psi\rangle$ and the output density matrix ρ as $\mathcal{F} = \mathrm{Tr}\left[\rho\,|\psi\rangle\,\langle\psi|\right]$ [9,117]. In our case, $|\psi\rangle = |\downarrow\rangle$ and ρ is the density matrix of the right spin after π-flip, so $\mathcal{F}$ is simply given by $P_{\mathrm{flip}}(t_\pi)$. Since our measurement does not yield the absolute probability, we normalize traces such that $A = C = 1/2$ in Eq. (5.1) and convert the signal to P_{flip}. Then, for the 123 MHz Rabi oscillation with $t_\pi = 4.1$ ns, we obtain $\mathcal{F} = 96.6$ %. We note that this conversion works only when the settling probability $P_{\mathrm{flip}}(t_{\mathrm{MW}} = \infty)$ is 1/2. This assumption is only valid for sufficiently large f_{R}, as will be explained below [15, 74]. When spin feels fluctuating nuclear fields with the distribution function $D_{\mathrm{N}}(\delta_\omega)$, which detune f_{MW} from the Larmor frequency f_{L} by $\delta_\omega/2\pi = f_{\mathrm{MW}} - f_{\mathrm{L}}$, the spin flip probability is given as

$$P_{\mathrm{flip}}(t_{\mathrm{MW}}) = \int_{-\infty}^{\infty} \mathrm{d}\delta_\omega D_{\mathrm{N}}(\delta_\omega) P_{\mathrm{flip}}(t_{\mathrm{MW}}; \delta_\omega), \tag{5.2}$$

where from the Rabi formula (Eq. (3.9)),

$$P_{\mathrm{flip}}(t;\delta_\omega) = \frac{{\omega_\mathrm{R}}^2}{2({\omega_\mathrm{R}}^2+{\delta_\omega}^2)}\left[1-\cos\left(t\sqrt{{\omega_\mathrm{R}}^2+{\delta_\omega}^2}\right)\right]. \tag{5.3}$$

The distribution function $D_\mathrm{N}(\delta_\omega)$ is well approximated by a Gaussian with standard deviation σ centered at $\delta_\omega = 0$, for a large number of random, unpolarized nuclear spins (due to the central-limit theorem):

$$D_\mathrm{N}(\delta_\omega) = D(\delta_\omega;\sigma) = \frac{1}{\sqrt{2\pi}\sigma}\mathrm{e}^{-{\delta_\omega}^2/(2\sigma^2)}. \tag{5.4}$$

Then we obtain

$$\begin{aligned} P_{\mathrm{flip}}(t_\mathrm{MW}=\infty) &= \int_{-\infty}^{\infty}\mathrm{d}\delta_\omega \frac{1}{\sqrt{2\pi}\sigma}\mathrm{e}^{-{\delta_\omega}^2/(2\sigma^2)}\frac{{\omega_\mathrm{R}}^2}{2({\omega_\mathrm{R}}^2+{\delta_\omega}^2)} \\ &= \sqrt{\frac{\pi}{8}}\frac{\omega_\mathrm{R}}{\sigma}\mathrm{e}^{\ {\omega_\mathrm{R}}^2/(2\sigma^2)}\mathrm{Erf}\left(\frac{\omega_\mathrm{R}}{\sqrt{2}\sigma}\right) \qquad (5.5) \\ &= \frac{1}{2}-\frac{1}{2}\left(\frac{\sigma}{\omega_\mathrm{R}}\right)^2+\mathcal{O}\left(\frac{\sigma}{\omega_\mathrm{R}}\right)^3, \qquad (5.6) \end{aligned}$$

where $\mathrm{Erf}(x)$ is the error function. From Eq. (5.6), when $\omega_\mathrm{R}/\sigma > 7$, the deviation from 50 % decreases to < 1 %. Given the typical value of $\sigma/2\pi = 7.0$ MHz [15], for $f_\mathrm{R} > 50$ MHz we can assume that $P_{\mathrm{flip}}(\infty) = 0.5$.

5.4.2 Discussions

5.4.2.1 Origin of Saturation

The knowledge of what causes f_R to saturate (Fig. 5.5(c)) would be useful for further improvement of MM-ESR. Saturation implies that at least one of the assumptions made in derivation of Eq. (3.17) is invalid under strong E_ac. However, the strength of E_ac is difficult to quantify exactly. While it would be possible to measure the amplitude of the MW that arrives at the gate, for instance by applying a square pulse, the conversion factor between the modulation of the MW gate voltage and the strength of E_ac is not accurately known. The PAT process would give a rough indication but in our device it is not observed presumably because our dots are parallel-coupled to the MW

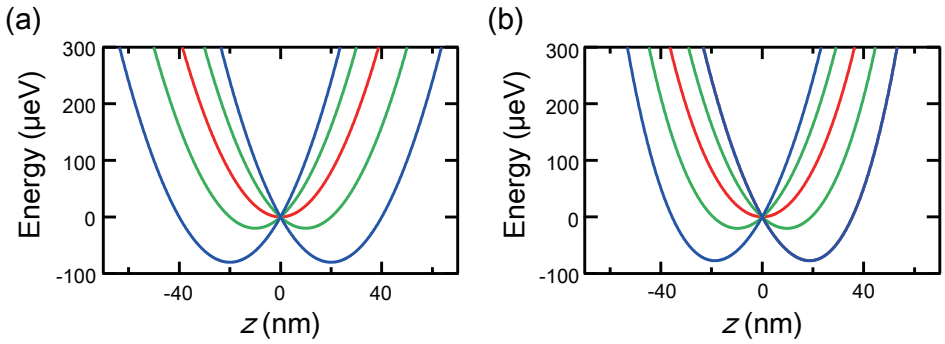

Figure 5.6: Harmonicity of QD confinement. (a) Harmonic QD confinement. The red trace shows the harmonic potential with orbital energy spacing of 500 μeV in the absence of MW irradiation, while the green and blue traces are under the MW with the amplitude of 4 μV/nm and 8 μV/nm, respectively. The potential shape does not change in the presence of MW irradiation. (b) Hard-wall confinement. Under MW irradiation the potential becomes asymmetric if a small quartic component is added.

gate. We therefore roughly estimate the order of E_{ac} from Eq. (4.1). Given $\Delta_{\mathrm{ST}} \sim 0.5$ meV, $f_{\mathrm{R}} \sim 100$ MHz and $b_{\mathrm{sl}} \sim 1$ mT/nm, and by assuming that the lateral confinement is symmetric, $E_{\mathrm{ac}} \sim 8$ μV/nm.

One likely scenario that explains the saturation behavior is the anharmonicity of the in-plane QD confinement [118]. Linear response to E_{ac} is a special property of the harmonic potential. For instance, if the confinement potential has a hard wall, the dot becomes less sensitive to large E_{ac}, which can explain the observed saturation behavior (Fig. 5.6). However, the anharmonicity of the potential would be difficult to quantify or control experimentally.

Another possible cause of saturation is decrease of b_{sl} under large displacement. From $E_{\mathrm{ac}} \sim 8$ μV/nm and $\Delta_{\mathrm{ST}} \sim 0.5$ meV, we expect the amplitude of displacement to be ~ 20 nm. This only accounts for 10 - 20% decrease of b_{sl} from field simulation, which is insufficient to reproduce the observed strong saturation of f_{R}.

5.4.2.2 Damping Mechanism and Coherence

In Fig. 5.5(a), it seems as if the Rabi oscillation decays faster as f_{R} gets larger. This is in contradiction with the naive expectation that the stronger ESR drive

will protect spin more securely from the low-frequency noise. One likely explanation is population leakage to non-qubit states due to photon mediated process, or PAT [66]. Under MW irradiation, a voltage drop $V_{\rm ac}\cos(2\pi f_{\rm MW}t)$ across a tunnel barrier modifies the tunnel rate, and the probability that an electron absorbs or emits n photons of energy $hf_{\rm MW}$ is described by $|J_n(eV_{\rm ac}/hf_{\rm MW})|^2$, with $J_n(\alpha)$ being the nth-order Bessel function of the first kind [32]. Thus a single-electron state with the energy E splits into a set of states with $E+nhf_{\rm MW}$ ($n=0,\pm1,\pm2,\dots$) in the presence of a classical, oscillating electric field. $J_n(\alpha)$ is very small for $\alpha \ll |n|$ (i.e. when $eV_{\rm ac} \ll |n|hf_{\rm MW}$), but starts to increase around $\alpha \approx |n|$. In the present experiment $f_{\rm MW} = 3$ GHz, and the single-photon energy $hf_{\rm MW} \sim 12$ μeV. Spin-blocked (1,1) triplets are energetically away from both (2,0) triplets and the Fermi level of the left reservoir by $\gtrsim 500$ μeV. Thus to lift PSB $n \gtrsim 40$ photons are required, and this process is usually suppressed. However, under very strong electric field, $eV_{\rm ac} \gtrsim$ 500 μeV, spin-independent tunneling is allowed, resulting in decrease of ESR signal which increases with $t_{\rm MW}$. Indeed, the highest $V_{\rm ac}$ (for $f_{\rm R} \sim 100$ MHz) is estimated to be ~ 800 μeV, based on the estimated value of $E_{\rm ac} \sim 8$ μV/nm and a rough approximation that the voltage drops linearly over the distance of ~ 100 nm between the two dot centers or between the dot center and the reservoir. Therefore, the PAT process can be relevant to the enhanced decay of Rabi oscillations.

It is expected that the decay envelope of Rabi oscillations contains information about the underlying noise spectrum [119, 120]. In our case, qubit leakage due to PAT would yield a single-exponential decay, while hyperfine-induced dephasing would result in a quadratic, Gaussian initial decay [121]. We therefore compare fitting qualities by single- and double- exponential decay functions (Fig. 5.7(a)). Unfortunately, however, our data is not large enough to conclusively determine the decay envelope.

We further characterize spin coherence under free evolution in a large inhomogeneous MM field [122], using the following echo pulse sequence. First an ESR $\pi/2$ pulse is applied and the spin experiences free induction decay for a dwell time t_1. Then spin is flipped by π and the phase is refocused for a rephasing time t_2. Finally a $3\pi/2$ pulse rotates spin ideally into a flipped state. Figure 5.7(b) plots the echo amplitude, as a function of the difference in dephasing and rephasing times. As the dwell time difference increases, the echo

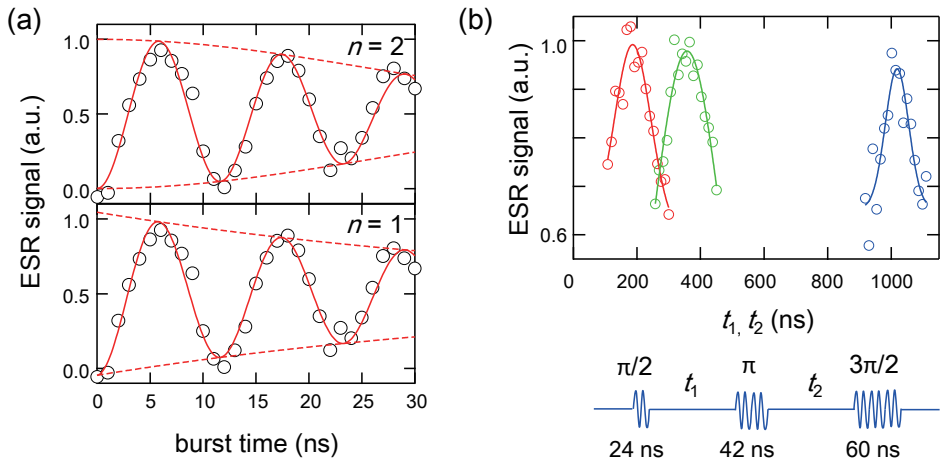

Figure 5.7: Phase coherence of driven and static spins. (a) Fitting of an 86 MHz Rabi oscillation by single- and double-exponential decays, $C + A\ \mathrm{e}^{-\left(t_{\mathrm{MW}}/T_{2,\mathrm{R}}\right)^n} \cos(2\pi f_{\mathrm{R}} t_{\mathrm{MW}})$. (b) Echo signals plotted as a function of t_1 and t_2. Red, green and blue traces are for t_2 =180, 330 and 990 ns, respectively. t_1 is swept around t_2.

signal decreases on a characteristic time scale T_2^* [60]. The best-fit width of a Gaussian with adjustable height and width gives $T_2^* = 94$ ns on average, which (although slightly longer) basically agrees with the previously reported value of $T_2^* = 37$ ns in GaAs QDs without a MM [60].

5.5 Summary

In this chapter, we realize ESR of single electron spins in a semiconductor QD in a strongly inhomogeneous magnetic field induced by a MM which is tailored for electrical spin manipulations. We observe two clear ESR peaks with an unprecedentedly large ESR peak separation of 80 mT or 440 MHz, which implies 5-fold enhancement of an inhomogeneous MM field. We demonstrate the Rabi frequency exceeding 120 MHz with a spin-flip fidelity above 95 %. The Rabi frequency saturates for strong electric fields (estimated amplitude of $\sim 8\ \mu$V/nm), possibly because of small anharmonicity of QD lateral confinement. We observe no indication of enhanced spin dephasing in a free evolution

condition, with $T_2^* = 94$ ns extracted from partially-refocused echo measurements. For the largest Rabi frequencies, coherent oscillations could be damped by PAT. However, the dominant dephasing mechanism in a driven condition is not determined conclusively in the present experiment. Observation of coherent oscillations for longer time, which probably involves improvement in measurement stability, will be illustrative to this end. The demonstrated speed-up of single-qubit gates will facilitate full qubit tomography and quantum error correction in this spin-qubit system. We anticipate that our scheme can bring 200 MHz ESR gates within experimental reach by using a thinner insulator to further reduce the distance between the MM and QDs.

Chapter 6

Distinct Features in Fast Rabi Oscillations

We study distinct single-electron-spin dynamics coupled to a nuclear-spin bath, when strongly driven by ESR. Unlike in previous experimental reports, our coherent oscillations show no "universal" $\pi/4$ phase shift and the decay is exponential within the first few Rabi periods. These findings contradict the long-time behavior expected for a non-Markovian, non-dissipative bath and indicate that we are in the strong driving regime, where the Rabi field is much larger than the coupling to the nuclear bath. This is further evidenced by observation of a "chevron" interference pattern in the time-spectral domain. The improved control of the coupled electron-nuclear system is an important step toward quantum computing using electron spins as qubits. Furthermore, recovery of exponential coherence decay will be beneficial for error-correction schemes which usually do not account for non-exponential decays.

6.1 Introduction

Coherence of an electron-spin qubit formed in semiconductor QDs is affected predominantly by nuclear spins in the host material. The hyperfine coupling leads to spin decoherence with a characteristic time T_2^* of the order of tens of nanoseconds when time averaged over experimental runs. The dynamical behavior strongly depends on the nuclear-spin dynamics. Both Markovian [123]

and non-Markovian [87] decoherence dynamics are predicted in different situations of time and energy scales. Just as with free induction decay, the driven spin coherence is strongly influenced by the nuclear spins. Theory predicts that interaction with a quasi-static bath results in a fast initial decay of the oscillation envelope followed by a power-law decay, and non-trivial phase shifts [74]. Indeed, these features are observed in all previous works on single-ESR in electrically controlled semiconductor QDs [15,61,66,67,69,72]. Coherent oscillations in these experiments are well fitted by

$$P_{\mathrm{flip}}(t) = P_{\mathrm{flip}}(\infty) + A'\, t^{-d} \cos(2\pi f_{\mathrm{R}} t + \phi), \tag{6.1}$$

where $d \sim 0.5$ and the overall phase shift ϕ is $\sim \pi/4$ universally, i.e. independently of many of the parameters of the bath.

We report that fast Rabi oscillations (with the Rabi frequency $f_{\mathrm{R}} \gtrsim 40$ MHz in GaAs QDs) show unconventional characteristics. In the regime of interest in spin-qubit experiments, i.e. at least up to $\sim 6\pi$ rotations, they are poorly fit by the conventional expression (Eq. (6.1)) but are well represented instead by an exponentially decaying envelope with no oscillation phase shift (Eq. (5.1)). We compare these experimental results with numerical simulations in the static limit of a nuclear-spin bath. To gain more insight, we probe the dynamics of an electron spin driven by ESR in the presence of frequency detuning. When f_{R} is sufficiently large, expected chevron patterns are recognized in the map of spin flip probability in the time-frequency domain, which are otherwise averaged out by nuclear fluctuations.

6.2 Fast and Slow Rabi Expressions

6.2.1 Model in the Static Bath Limit

To drive fast spin flips, we use a MM-ESR technique; a burst of MW with the angular frequency ω is applied along the external magnetic field B_{ext} ($\parallel \hat{z}$) in the MM's stray magnetic field, whose x-component is slanted at the position of the QD. The Fermi contact hyperfine interaction between the electron spin $\boldsymbol{S}$ and the surrounding nuclear spins is effectively described by $g\mu_{\mathrm{B}}\boldsymbol{B}_{\mathrm{N}}\cdot\boldsymbol{S}$, where $\boldsymbol{B}_{\mathrm{N}}$ is

the so-called Overhauser field (effective magnetic field for an electron spin due to the nuclear-spin bath). The Landé g-factor g is ~ -0.33 in our GaAs QDs. For a large number of nuclear spins ($N \sim 10^6$ in GaAs QDs) $B_{\mathrm{N},\alpha}$ ($\alpha = x, y, z$) is Gaussian distributed (due to the central-limit theorem) [13, 86]. A large static $B_{\mathrm{ext}} \sim 0.5$ T, together with the z-component of the MM stray field $B_{\mathrm{M},z}$, produces a Zeeman splitting $g\mu_{\mathrm{B}}(B_{\mathrm{ext}} + B_{\mathrm{M},z}) = \hbar\omega_{\mathrm{L}}$ (ω_{L} is the Larmor precession frequency). Due to Zeeman energy mismatch between nuclear- and electron-spins, we may neglect the transverse terms of the Overhauser field that give rise to electron-nuclear-spin flip-flops and $B_{\mathrm{N},z}$ shifts the resonance angular frequency by $\omega_{\mathrm{N}} = g\mu_{\mathrm{B}}B_{\mathrm{N},z}/\hbar$. Although our measurements are performed in a DQD with one electron in each dot, the relevant dynamics is that of a single electron spin, since the Larmor precession frequency $f_{\mathrm{L}}(= \omega_{\mathrm{L}}/2\pi)$ is well separated between the two dots (~ 400 MHz $\gg f_{\mathrm{R}}$) and the exchange coupling is suppressed by large level-detuning ($|\varepsilon| \sim 500$ μeV) during ESR excitation.

Thus our experimental settings can be modeled by the following Hamiltonian of a single spin,

$$\mathcal{H}_{\mathrm{lab}}(t) = \frac{\hbar(\omega_{\mathrm{L}} + \omega_{\mathrm{N}})}{2}\sigma_z + \frac{\hbar\omega_{\mathrm{R}}}{2}\cos(\omega t)\sigma_x, \tag{6.2}$$

where σ_α ($\alpha = x, z$) are the Pauli matrices and $\omega_{\mathrm{R}} = 2\pi f_{\mathrm{R}}$. Using the rotating wave approximation, which is valid for $|\omega_{\mathrm{R}}| \ll |\omega_{\mathrm{L}} + \omega_{\mathrm{N}}|$, the effective Hamiltonian in the frame rotating at ω is simplified to

$$\mathcal{H}_{\mathrm{ref}}(t) = \frac{\hbar\delta_\omega}{2}\sigma_z + \frac{\hbar\omega_{\mathrm{R}}}{2}\sigma_x, \tag{6.3}$$

where the angular frequency detuning $\delta_\omega = \omega_{\mathrm{L}} + \omega_{\mathrm{N}} - \omega$.

Nuclear-spin dynamics is typically very slow because the nuclear spins are only weakly dipole-coupled with each other and the bath itself is coupled very weakly to its dissipative environment such as phonons. The correlation time of the fluctuations in the nuclear-spin system is typically $\gg 1$ μs [124, 125] and is much longer than the timescale for electron-spin dynamics considered here (up to 800 ns). Therefore, we assume that δ_ω is frozen during a single electron-spin time evolution, but fluctuates between experimental runs. The distribution function of δ_ω is also Gaussian following that of the Overhauser field. Under

the resonance condition (that is, $\langle\delta_\omega\rangle = 0$), the standard deviation of δ_ω is given by $\sigma = g\mu_\mathrm{B}\sqrt{\langle(B_{\mathrm{N},z} - \langle B_{\mathrm{N},z}\rangle)^2\rangle}/\hbar$. Then, the probability of flipping the target spin is given by Eq. (5.2).

6.2.2 Different Regimes of the Rabi Oscillation

The spin flip probability $P_\mathrm{flip}(t_\mathrm{MW})$ under resonant ESR excitation can be decomposed to a time-independent term $P_\mathrm{flip}(\infty)$ and a time-dependent term $\tilde{P}_\mathrm{flip}(t_\mathrm{MW})$:

$$P_\mathrm{flip}(t_\mathrm{MW}) = P_\mathrm{flip}(\infty) - \tilde{P}_\mathrm{flip}(t_\mathrm{MW}). \tag{6.4}$$

When we assume that the Overhauser field fluctuates following a Gaussian distribution (Eq. (5.4)) but is static during each spin-manipulation process, from Eq. (5.3), $P_\mathrm{flip}(\infty)$ is given in Eq. (5.5) and $\tilde{P}_\mathrm{flip}(t)$ reads

$$\tilde{P}_\mathrm{flip}(t) = \int_0^\infty \mathrm{d}\delta_\omega \frac{\mathrm{e}^{-{\delta_\omega}^2/(2\sigma^2)}}{\sqrt{2\pi}\sigma} \frac{{\omega_\mathrm{R}}^2}{{\omega_\mathrm{R}}^2 + {\delta_\omega}^2} \mathrm{Re}\left[\mathrm{e}^{it\sqrt{{\omega_\mathrm{R}}^2+{\delta_\omega}^2}}\right]. \tag{6.5}$$

To capture the oscillation form, it is convenient to introduce dimensionless parameters, $\tau = \omega_\mathrm{R} t$ and $\gamma = \omega_\mathrm{R}/\sigma$. We change the variable from δ_ω to x such that $x = \left(\sqrt{{\omega_\mathrm{R}}^2 + {\delta_\omega}^2} - \omega\right)/\sigma$. Noting that $\delta_\omega = \sigma\sqrt{x(x+2\gamma)}$ and $\mathrm{d}\delta_\omega/\mathrm{d}x = \sigma(x+\gamma)/\sqrt{x(x+2\gamma)}$,

$$\tilde{P}_\mathrm{flip}(\tau) = \frac{\gamma^2}{\sqrt{2\pi}} \int_0^\infty \mathrm{d}x \frac{\mathrm{Re}\left[\exp\left(-\frac{x^2}{2} - \gamma x + \frac{i\tau x}{\gamma}\right)\mathrm{e}^{i\tau}\right]}{\sqrt{x(x+2\gamma)}(x+\gamma)}. \tag{6.6}$$

We introduce another parameter $\lambda = \gamma - i\tau/\gamma$ $(= \sqrt{\gamma^2 + (\tau/\gamma)^2}\mathrm{e}^{i\arctan(\gamma^2/\tau)})$, and expand the kernel of the integral only to the lowest order of x using the stationary phase approximation [15, 74, 121],

$$\begin{aligned}\tilde{P}_\mathrm{flip}(\tau) &\approx \frac{1}{2}\sqrt{\frac{\gamma}{\pi}} \int_0^\infty \mathrm{d}x \frac{\mathrm{Re}\left[\mathrm{e}^{-\lambda x + i\tau}\right]}{\sqrt{x}} = \frac{\sqrt{\gamma}}{2}\mathrm{Re}\left[\mathrm{e}^{i\tau}/\sqrt{\lambda}\right] \\ &= \frac{\cos\left(\tau + \frac{1}{2}\arctan(\gamma^2/\tau)\right)}{2\sqrt[4]{1 + (\tau/\gamma^2)^2}}.\end{aligned} \tag{6.7}$$

In the weak driving regime with $\gamma \lesssim 1$, this approximation is valid for $\tau/\gamma \gg$

1, because only $x \lesssim \gamma/\tau$ can contribute to the integral in Eq. (6.6). Otherwise the integrand function oscillates rapidly as a function of x and averages to zero, as a result of large susceptibility of electron spin dynamics to nuclear fluctuations. From Eq. (6.7), in the weak driving limit $\gamma^2 \ll \tau$, we obtain

$$\tilde{P}_{\text{flip}}(\tau) \approx \frac{\gamma}{2\sqrt{\tau}} \cos\left(\tau + \frac{\pi}{4}\right). \tag{6.8}$$

This expression is equivalent to Eq. (6.1). In this regime, coherent oscillation is damped rapidly even before the first spin flip time t_π, followed by a relatively slow damping.

By contrast, in the strong driving regime where $\gamma \gg 1$, the approximation becomes valid for all range of τ. This is due to the exponential cutoff at $x \gtrsim 2/\gamma$, which essentially arises from increased immunity of electron spin dynamics to nuclear fluctuations. From Eq. (6.7), we obtain the expression for $\gamma \gg 1$,

$$\tilde{P}_{\text{flip}}(\tau) \approx \frac{1}{2} \mathrm{e}^{-(\tau/2\gamma^2)^2} \cos(\tau). \tag{6.9}$$

This expression is equivalent to Eq. (5.1). In this regime, the initial phase shift vanishes and the initial Gaussian (quadratic) decay lasts for $\tau \sim \gamma^2$.

To check the validity of these expressions for "slow" and "fast" Rabi oscillations, we numerically compare them with the exact calculation. Figure 6.1(a) plots the simulated Rabi oscillations $P_{\text{flip}}(\tau)$ obtained from Eqs. (6.6) and (5.5). For $\gamma \lesssim 2$, besides reduced maximum spin flip probability, the oscillation phase is shifted by $\sim \pi/4$, as expected from the slow Rabi expression, Eq. (6.8). For $\gamma \gtrsim 4$, this phase shift vanishes and the spin flip probability for $\tau = 1/2$ (π-rotation) approaches 1. In this regime the fast Rabi expression, Eq. (6.9), well describes the oscillation (Fig. 6.1(c)).

6.2.3 Fitting of the Real Data

The slow Rabi expression (Eq. (6.1)) is featured by a rapid damping before the first spin flip, followed by a relatively slow decay of oscillation and an initial phase shift $\sim \pi/4$. These features are commonly observed in previous ESR experiments with semiconductor QDs but are absent in the Rabi oscillations with $f_{\text{R}} \gtrsim 40$ MHz observed here. These oscillations are well fit, for at least up to

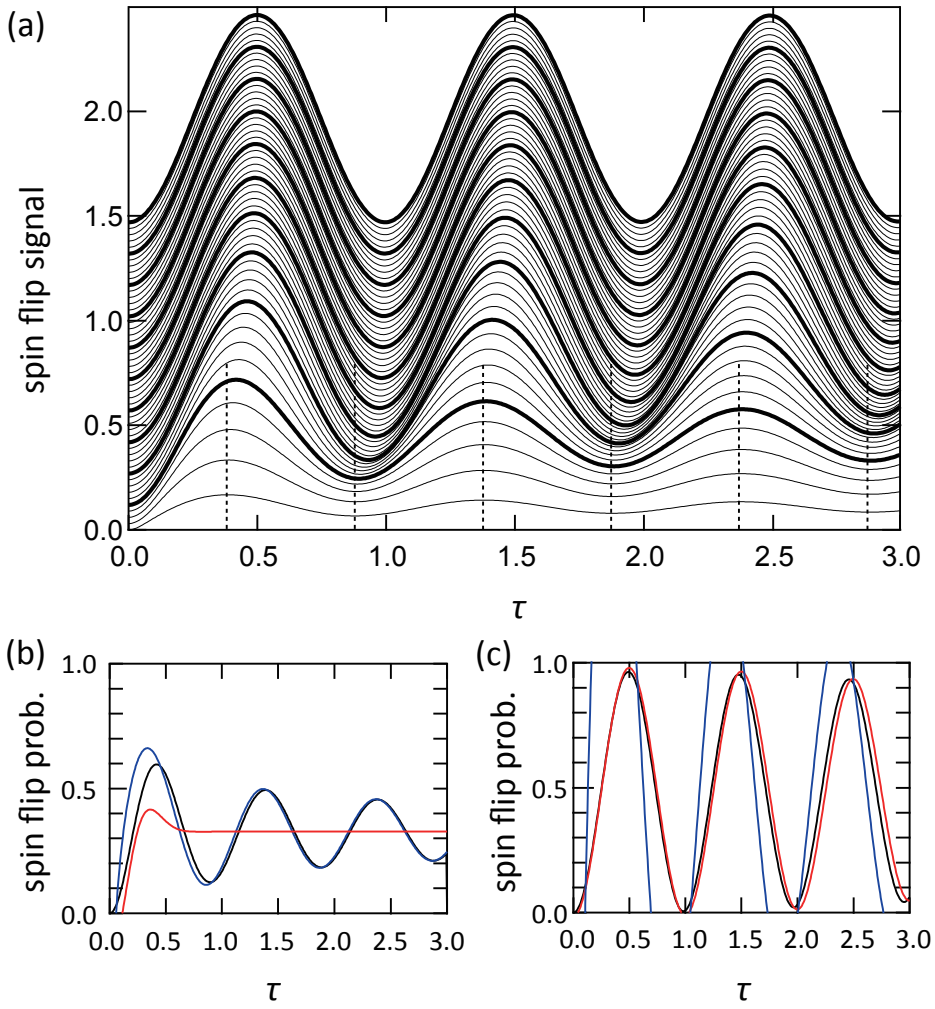

Figure 6.1: Simulated Rabi oscillations for different $\gamma = \omega_R/\sigma$. (a) Numerically simulated spin flip probability as a function of renormalized time τ for different values of γ. γ is stepped from 0 to 10 in step of 0.2. Thick lines represent traces for integer γ. Traces are offset for clarity. (b) Numerically simulated spin flip probability (black trace), along with the fast (red) and slow (blue) Rabi expressions for $\gamma = 1$. (c) Same type of plot for $\gamma = 5$. Slow Rabi expression (blue trace) produces an unphysical outcome in this regime.

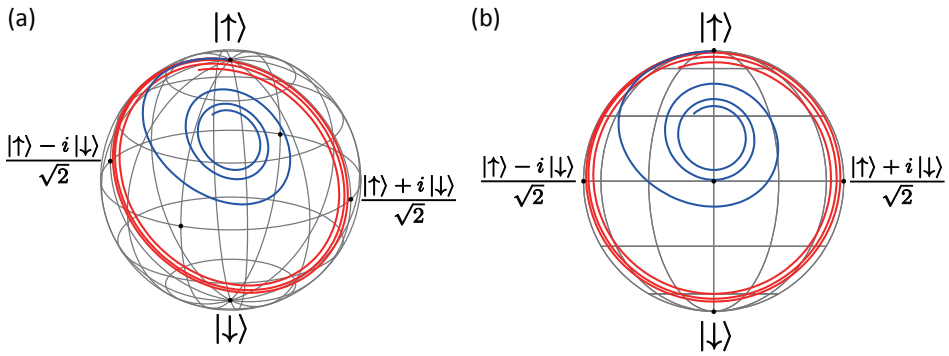

Figure 6.2: Simulated driven spin trajectories in the Bloch sphere. (a) Representation of the Bloch vector evolution of ensemble spin. Spin is initialized in the up-spin state at $\tau = 0$ and is driven by ESR for up to $\tau = 3$. The blue trace is for $\gamma = 1$ and the red one is for $\gamma = 5$. When spin is strongly driven the vector remains near the Bloch sphere (approximated by a pure state), whereas weakly driven spin rapidly goes inwards (i.e. mixed), approaching the z-axis. (b) Projection of the same trajectories onto the yz plane.

6π spin flips with no initial phase shift, by the fast Rabi expression (Eq. (5.1)), which shows large initial oscillations with no $\pi/4$ phase shift, followed by a rapid decay of oscillation (Fig. 6.3(a)). On the other hand, the Rabi oscillation with $f_{\mathrm{R}} \lesssim 15$ MHz is well approximated by the slow Rabi expression (Fig. 6.3(b),(c)). We note that the f_{R} ranges of fast and slow Rabi oscillations are consistent with the theoretical prediction (Fig. 6.1). Indeed, $f_{\mathrm{R}} = 15$ and 40 MHz corresponds to $\gamma = 2.1$ and 5.7, respectively, with a typical value of $\sigma = 2\pi \times 7.0$ MHz in GaAs QDs [15]. To illustrate the deviation of the fast, 86 MHz Rabi oscillation from the slow Rabi expression, we plot fitting parameter dependence in Fig. 6.3(d). Irrespective of values of fitting parameters, the slow Rabi expression cannot account for the experimental result, owing to the qualitative difference of the decay function and the oscillation phase.

6.3 Chevron Pattern

The electron-spin dynamics under detuned ESR driving gives further information about the effects of nuclear spins. The ESR spin flip probability when driven by detuned ESR in the presence of slow Gaussian-distributed nuclear

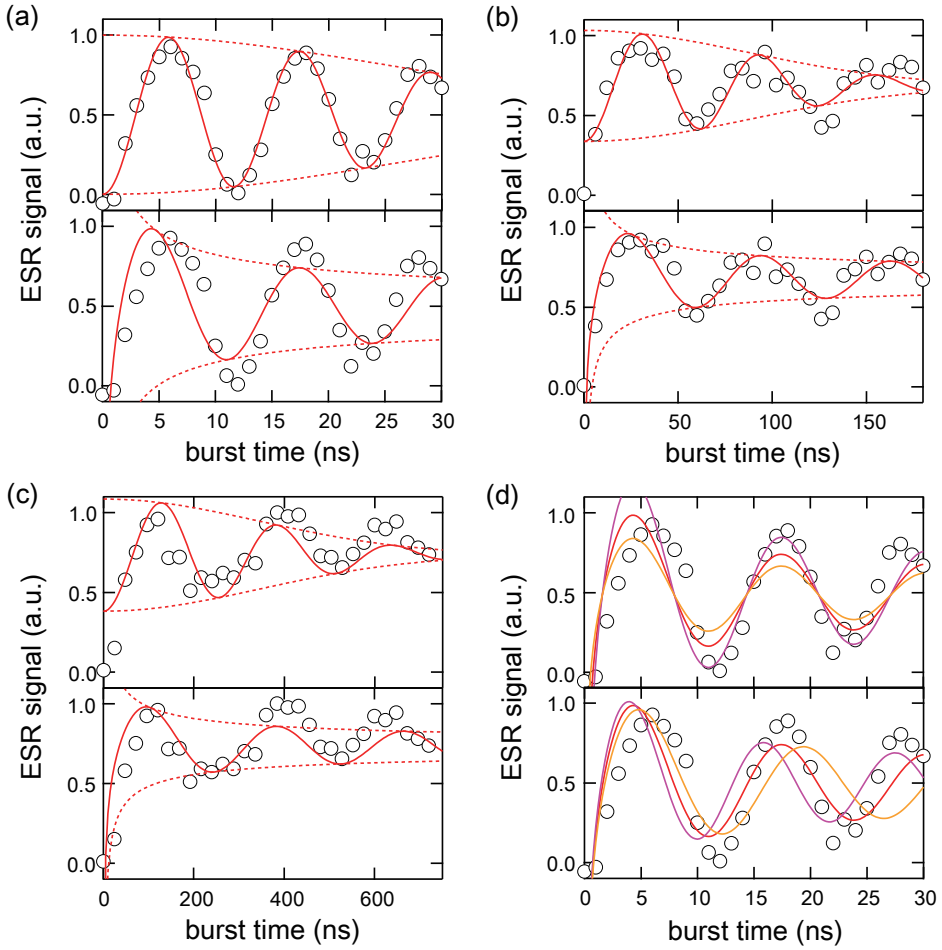

Figure 6.3: Comparison of fitting qualities. (a) Comparison of different fit functions of 86 MHz Rabi data. The top panel shows the least-square fit to the fast Rabi expression, whereas the bottom one is to the slow Rabi expression. (b),(c) Same type of comparison as in (a) for the 15 MHz and 4 MHz Rabi data. To resolve these slow oscillations, which are more susceptible to the nuclear field, B_{ext} is swept and the signal is processed following the procedure presented in ref. [66]. We note that with the present setup and device stability, the probability cannot be directly determined from the trans-conductance charge-sensing signal. Data presented here are therefore all linearly converted, whose scale is data dependent. (d) Parameter dependence of fit quality of the 86 MHz Rabi oscillation by the slow Rabi expression. In the top panel, the oscillation amplitude A' in Eq. (6.1) is intentionally changed by a factor of $\sqrt{2}$ or $1/\sqrt{2}$. In the bottom panel, f_{R} is changed by a factor of 1.1 or 0.9.

fluctuations can be expressed, in a similar manner to Eq. (5.2), as

$$P_{\mathrm{flip}}(t_{\mathrm{MW}}, \delta; \sigma) = \int_{-\infty}^{\infty} \mathrm{d}\delta_{\omega} D(\delta_{\omega}; \sigma) P_{\mathrm{flip}}(t_{\mathrm{flip}}; \delta + \delta_{\omega}), \tag{6.10}$$

where δ is the angular frequency detuning of the MW, σ is the standard deviation of the angular frequency detuning due to the nuclear field and t_{MW} is the MW burst duration. By introducing dimensionless parameters, $\tau = \omega_{\mathrm{R}} t$, $\gamma = \omega_{\mathrm{R}}/\sigma$, $\nu = \delta/\omega_{\mathrm{R}}$ and $y = \delta/\sigma$, it can be equivalently expressed as

$$P_{\mathrm{flip}}(\tau, \nu; \gamma) = \int_{-\infty}^{\infty} \mathrm{d}y \frac{\mathrm{e}^{-(y-\nu\gamma)^2}}{\sqrt{2\pi}\,(1+\nu^2)} \left(1 - \cos\left(\tau\sqrt{1+\nu^2}\right)\right). \tag{6.11}$$

In the coherent limit with $\sigma \to 0$ (or equivalently $\gamma \to \infty$), a map of $P_{\mathrm{flip}}(t_{\mathrm{MW}}, \delta; 0)$ (or $P_{\mathrm{flip}}(\tau, \nu; \infty)$) makes chevron patterns in the time-spectral (t_{MW}-δ) domain or in the τ-ν plane. The patterns become blurred, when we take into account the effect of static Gaussian-distributed Overhauser field. Figure 6.4 shows maps of P_{flip} for different values of $\gamma = \omega_{\mathrm{R}}/\sigma$. Chevrons can be recognized only for $\gamma \gtrsim 4$, which corresponds to $f_{\mathrm{R}} \gtrsim 28$ MHz for a typical value of $\sigma = 2\pi \times 7$ MHz for GaAs QDs.

Figure 6.5(a) plots the map of the Rabi oscillation intensity with $f_{\mathrm{R}} = 86$ MHz as a function of t_{MW} and B_{ext}. Chevron interference patterns are clearly recognized, indicating that we are in the strong driving regime with $\gamma \gtrsim 4$. This implies that driven electron-spin states are relatively immune to the nuclear spin noise on the timescale of interest. Otherwise, the chevron patterns would be blurred due to ensemble averaging over sizable Overhauser fluctuations within the integration time for each data pixel, and scattered due to slow drift within the whole measurement time. Indeed, these effects are evident in the map of the slow Rabi oscillation intensity with $f_{\mathrm{R}} = 15$ MHz (Fig. 6.5(b)). The slow drift of the interference pattern is due to the dynamical nuclear polarization (DNP), whose amplitude is comparable to that of the fluctuation. We discover that both effects of the fluctuating nuclear field and DNP are minimal or absent for the fast Rabi oscillation.

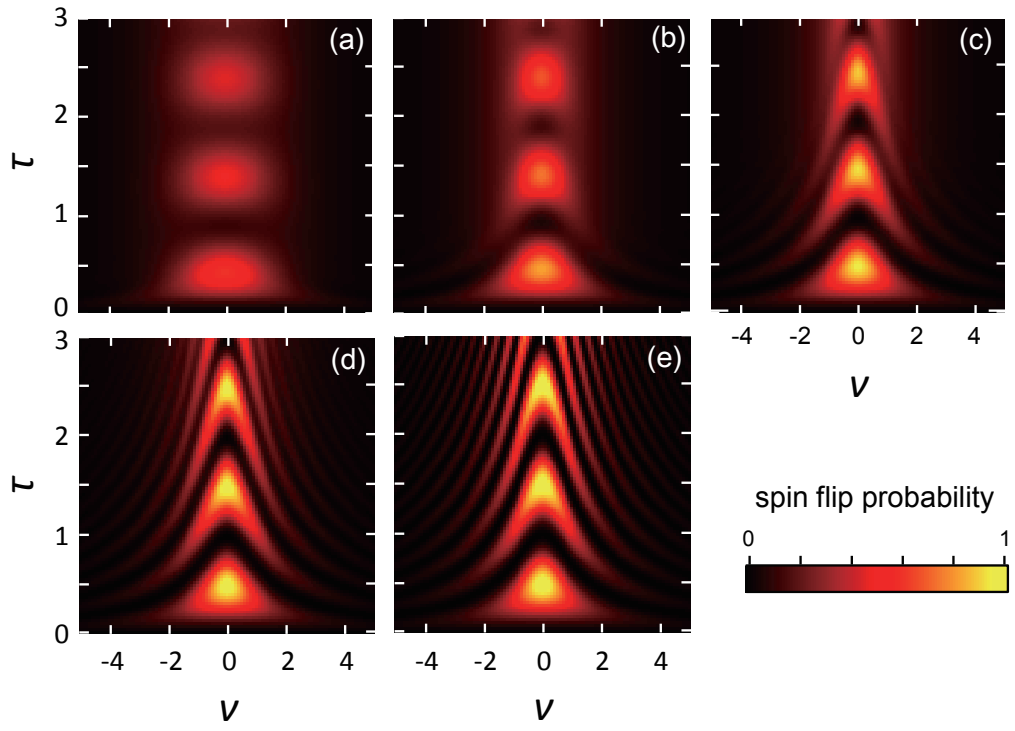

Figure 6.4: Simulated maps of spin flip probability in the τ-ν plane. The horizontal axis is the normalized frequency detuning, $\nu = \delta/\omega_{\mathrm{R}}$ and the vertical axis is the normalized MW burst time, $\tau = \omega_{\mathrm{R}} t_{\mathrm{MW}}$. Calculated for different values of the normalized Rabi frequency, $\gamma = \omega_{\mathrm{R}}/\sigma = 1$(a), 2(b), 4(c), 8(d) and ∞(e). Chevron patterns are recognized for $\gamma \gtrsim 4$.

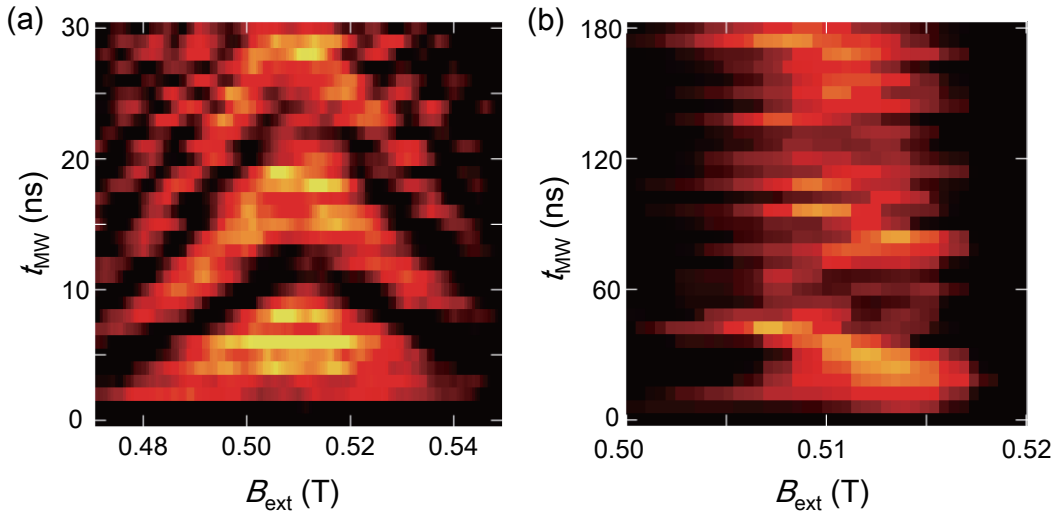

Figure 6.5: Map of ESR signals as a function of B_{ext} and duration of MW burst. Yellow is high signal, black is low. (a) $f_{\mathrm{R}} = 86$ MHz. Chevron patterns are clearly recognized. (b) $f_{\mathrm{R}} = 15$ MHz. Chevron patterns are scattered and blurred.

6.4 Summary

In this chapter we study the driven single-electron-spin dynamics coupled to a nuclear-spin bath. We observe distinct features when the electron spin is strongly driven by ESR. First, fast Rabi oscillations with $f_{\mathrm{R}} \gtrsim 40$ MHz show no oscillation phase shift and the decay is exponential within the first few Rabi periods. Second, chevron interference patterns are recognized in the Rabi oscillation intensity in the time-spectral domain. These features contradict a theoretical expectation from strong coupling to the slow environment which would invalidate the well-known Markovian Bloch equations. They are instead well captured by our standard static-bath model, when the Rabi field is at least 4 times larger than the bath fluctuation. Qualitative improvement of controllability of the coupled spin system demonstrated here will be a foundation of high fidelity quantum information processing with electron spin qubits. The exponential coherence decay observed here will be essential for quantum error correction, which is indispensable for quantum computation.

Chapter 7

Phase Rotation of a Single Electron Spin

Electron spin in QDs offers a distinguished platform for quantum computation in solids. In this system rotations about the x- and y-axes via ESR are widely accepted as the only resource for single spin-qubit operations, and to date fast rotation about the z-axis within the ensemble phase coherence time T_2^* is yet to be demonstrated. Here we propose a novel scheme for a single-step electrical phase rotation utilizing an inhomogeneous magnetic field induced by a proximal MM, and demonstrate up to 50 MHz operation. This is the fastest phase flip ever reported for single-electron spin qubits and can perform a $\pi/4$ phase rotation in 2.4 ns, an order of magnitude shorter than T_2^*, several tens of nanoseconds. We anticipate that the single-step z-rotation demonstrated here will facilitate experimental realization of various quantum gates such as CNOT.

7.1 Introduction

It is commonly known that x- and y-rotations via ESR are sufficient for arbitrary rotation of a single spin. By choosing the phase of the a.c. driving field, ESR can rotate electron spin about an arbitrary axis in the xy plane, but the rotation around the z-axis is an important exclusion. To implement the z-rotation, a 3-step decomposition into ESR rotations, $R_z(\theta) =$

$R_y(-\pi/2)R_x(\theta)R_y(\pi/2)$, can be used instead, where $R_\alpha(\theta)$ denotes a single-spin rotation around the α-axis by an angle θ. However, this implementation takes $(1 + \pi/\theta)$ times longer than the direct phase shift at the same speed would take. The gate time difference due to overhead (two R_y rotations) can be relevant, especially when θ is small. Indeed, even with 120 MHz ESR, a sequence of $R_y(-\pi/2)R_x(\pi/4)R_y(\pi/2)$ consumes 5.2 ns, which is competed by $R_z(\pi/4)$ operating at no faster than 24 MHz. In the meantime, most quantum circuits contain phase-shift gates such as the $\pi/8$ gate $T = R_z(\pi/4)$, the phase gate $S = R_z(\pi/2)$ and the Pauli-Z gate $Z = R_z(\pi)$. For instance, performing a CNOT gate with exchange gates and single qubit gates will involve three phase rotations typically, although the details depend of course on the particular decomposition scheme used (Fig. 7.1). Performing these gates would be much simpler and faster, if the spin phase can be directly controlled by electrical gating.

7.2 Concept for Electrical Phase Control

The kind of control magnetic field required for phase gates is quite different from the one used for ESR. While ESR requires an a.c. field perpendicular to the quantization axis, phase shift is induced by a parallel static field, which we call the Zeeman field as it defines the Zeeman energy. The phase acquisition rate of electron spin in the laboratory frame, or the so-called Larmor precession rate, is determined by the local Zeeman field. In the qubit reference frame where the spin phase is static under free evolution, the phase acquisition rate is proportional to the change of the Zeeman field, $\delta B_{\rm Z}$. We note that $\delta B_{\rm Z}$ is the shift of the Zeeman field with respect to the one defining the single qubit frame. If we can turn on and off this field, then the single-qubit phase can be gated, possibly quickly. Indeed, in GaAs QDs (with the Landé g-factor $|g| \sim 0.4$), for $\delta B_{\rm Z} = 10$ mT the relative phase evolution is as fast as 50 MHz.

The challenge is then how to electrically control the Zeeman field within a single QD. This is actually possible by utilizing the slating Zeeman field induced by a proximal MM (Fig. 7.2). If we displace the electron wave-function with gate voltages in the presence of the spatially inhomogeneous stray field, spin feels a different field, $\delta \boldsymbol{B}_{\rm MM}$. The x- and y-components of $\delta \boldsymbol{B}_{\rm MM}$ can be

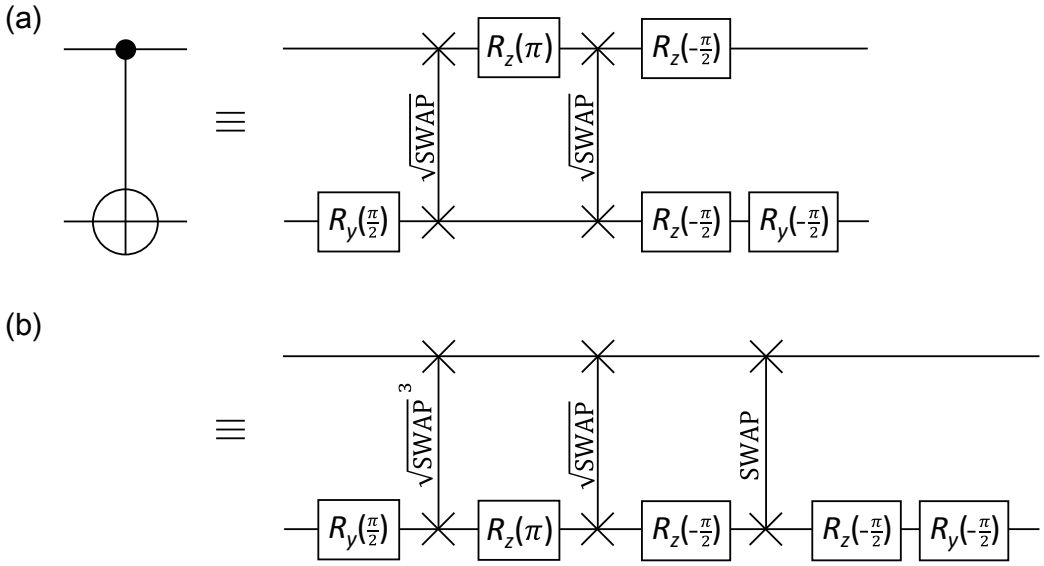

Figure 7.1: CNOT implementation and phase gates. (a) An example of decomposition of a CNOT circuit into exchange gates and single qubit rotations. Two $\sqrt{\text{SWAP}}$ and two $R_y(\theta)$ operations per one CNOT gate can be directly induced by exchange interaction and ESR, respectively. Three $R_z(\theta)$ gates per one CNOT cannot be performed directly by these conventional control knobs. (b) Another example of decomposition. Despite the increased total number of gates, this implementation has a potential advantage since single qubit rotations involve only one spin.

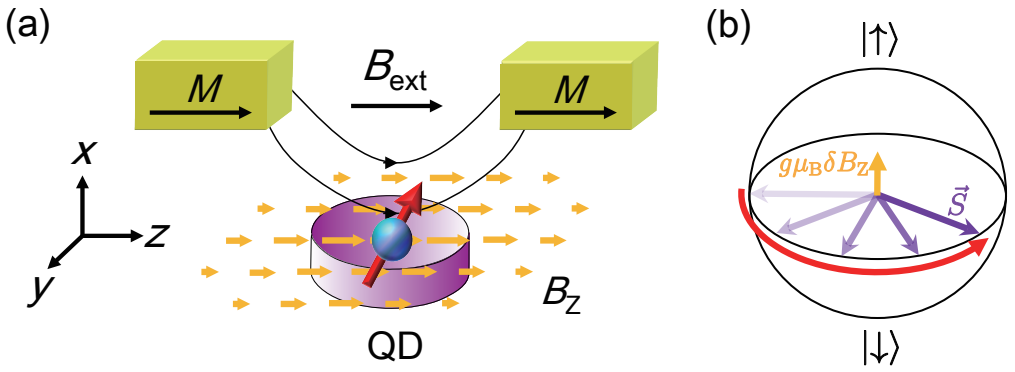

Figure 7.2: Phase gate concept. (a) The MM placed on top of the QD produces a spatially distributed Zeeman field. If the electron is displaced, spin will precess at a different frequency. (b) A qubit spin acquires phase due to change in the local Zeeman field, at a rate proportional to δB_Z, in the qubit reference frame.

disregarded, as they do not contribute to the total magnetic field to leading order approximation under the large external magnetic field $B_{ext} \parallel \hat{z}$, i.e. the effective field can be approximated as $\delta B_{MM,z}\hat{z}$. We can therefore gate control δB_Z ($= \delta B_{MM,z}$) under the spatially distributed Zeeman field imposed by a MM.

7.3 Electrical Control of the Zeeman Field

To demonstrate the proposed scheme of phase gate, we use a GaAs-based lateral DQD. We employ a cobalt MM of the refined design (see Chapter 4) and use a heterostructure with a shallow (57 nm deep) 2DEG in order to boost the inhomogeneous Zeeman field necessary for phase gates as well as the slanting field to drive ESR by MW irradiation. From stray field simulation if the QD position can be displaced by 10 nm, δB_Z is expected to be an order of 10 mT, which is already sufficient for performing a 50 MHz phase gate. At a dilution refrigerator temperature the device is tuned into the PSB regime near the (1,1)-(2,0) charge transition to initialize and detect spin states with charge sensing (see §5.2 for further details of experimentals). Increased spatial distribution of the local magnetic field induced by our MM is exemplified by $>$ 100 MHz Rabi

oscillations (see §5.4) and a ~ 100 mT ESR peak separation (see §5.3).

We further characterize the Zeeman field inhomogeneity from the pump-and-probe ESR spectra (Fig. 7.3). After initializing spins into parallel triplet states relying on PSB at zero level-detuning ($\varepsilon = 0$), a MW at a fixed frequency $f_{\mathrm{MW}} = 8.2$ GHz is burst at various gate voltage configurations in the (1,1) Coulomb blockade region, followed by PSB spin readout at $\varepsilon = 0$. The ESR signal is peaked when f_{MW} is consistent with the electron Zeeman energy determined by the sum of B_{ext} and the MM-induced local Zeeman field $\delta B_{\mathrm{MM},z}$ at the pump position. The gate dependent δB_{Z} will then be probed from the B_{ext} value at the ESR peak center. If we change the ESR pump position from points A to D and 1 to 4 in the (1,1) Coulomb blockade region (Fig. 7.3(b)), the two ESR peak centers shift fairly monotonically (Fig. 7.3(c)), reflecting the δB_{Z} tunability with gate voltage. The result indicates that the local Zeeman field can be electrically controlled over the range of 12 mT due to the displacement of the electron. This change δB_{Z} is accounted for if the electron is displaced by ~ 10 nm from A to D or from 1 to 4. We note that a 10 nm displacement can be induced by an electric field of reasonable strength (4 μV/nm given the harmonic potential with orbital energy spacing of 500 μeV). $\delta B_{\mathrm{Z}} = 12$ mT corresponds to 55 MHz phase accumulation, and therefore only 2.2 ns is needed to perform the $\pi/8$ gate, $T = Z(\pi/4)$. To implement this T gate in the same gating time would require 220 MHz ESR rotations with the conventional 3-step sequence.

7.4 Time-Resolved Measurement of Phase Rotation

7.4.1 Demonstration of Phase Control

Figure 7.4(a) shows the pulse sequence used to experimentally demonstrate the phase gate we propose. We rely on the PSB effect to initialize and readout the spin states. Since the PSB-based measurement is insensitive to spin phase itself, we incorporate two $\pi/2$ pulses via ESR (tuned to the right spin resonance) before and after the phase rotation to project the induced phase shift to the spin

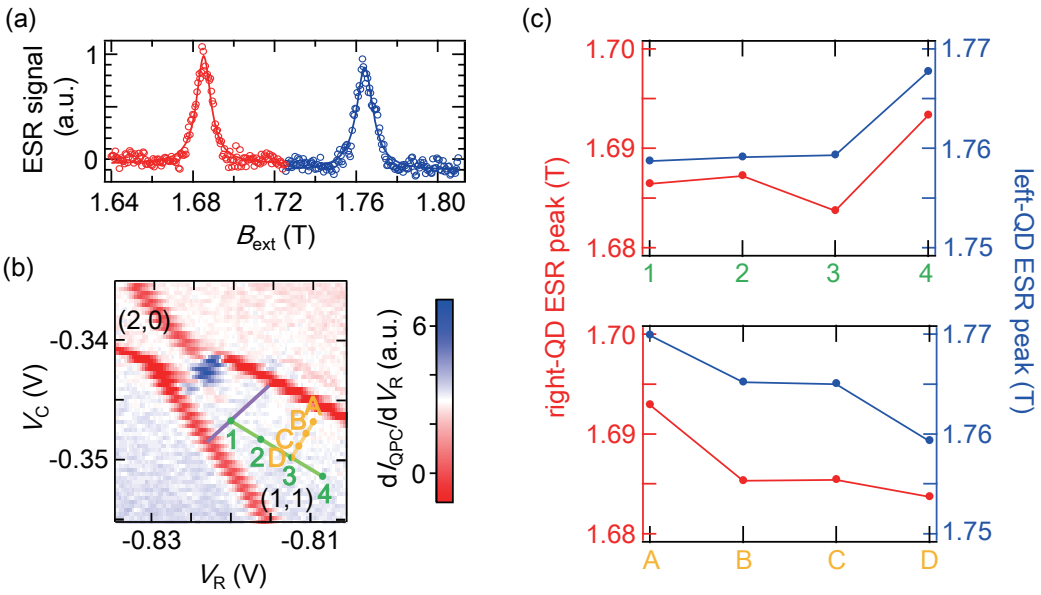

Figure 7.3: Probing local Zeeman fields. (a) ESR spectra. Two ESR peaks are clearly resolved, 80 - 100 mT apart. The peak at the lower (higher) field plotted in red (blue) is due to the resonance of the right (left) spin. The solid lines show the fitting results by a Lorentzian profile. (b) Pump positions in the stability diagram used for the field probe. The purple line indicates where $\varepsilon = 0$ at the (1,1)-(2,0) charge transition. (c) ESR peak field dependence on pump positions. Each data point represents the value of B_{ext} where the ESR peak is observed, after averaging over 50 B_{ext} sweeps.

z-component. Here the qubit reference frame is naturally defined by the local Zeeman field at P_0 (indicated in Fig. 7.4(b)) in the (1,1) Coulomb blockade region, where two $\pi/2$ pulses are applied, so that $\delta B_Z = 0$ at P_0. When the QD is biased at P_1, the qubit phase is accumulated due to the finite δB_Z. The measured spin signal oscillates sinusoidally at $f_Z = 53.9$ MHz as a function of voltage pulse duration at P_1 (Fig. 7.4(c)). This indicates $\delta B_Z = 12$ mT at P_1, which can be accounted for by ~ 10 nm shift of the electron wave-function in the right QD. The time required for $Z(\pi/4)$ is as short as 2.3 ns. Using the conventional sequence the gating time would be more than twice as long even with the 120 MHz rotation (the fastest ESR ever reported). We numerically simulate the average gate fidelity[1] $\bar{\mathcal{F}}$ for $Z(\pi)$ to be as high as 97.9 %, with $f_Z = 53.9$ MHz and $T_2^Z = 36.0$ ns. We note that unlike ESR gates, the gate fidelity for phase gates cannot be extracted directly from the probability of finding spin flip, as the signal may contain contribution from infidelity of ESR pulses involved in the sequence.

7.4.2 Pulse Amplitude Dependence

We further confirm the validity of our phase gate operation, by taking the amplitude dependence. Since δB_Z is expected to linearly increase with displacement, the phase accumulation rate f_Z would be roughly proportional to the pulse amplitude. To see this we use a slightly modified pulse sequence with an extra echoing π ESR pulse inserted, which maps the induced phase shift to the measurable z-component (Fig. 7.5(a)). In this $\pi/2$-π-$\pi/2$ sequence, the three ESR pulses are equally spaced in time just as in a conventional spin echo

[1]The average gate fidelity that quantifies how well a quantum operation $\mathcal{U}$ approximates a quantum gate U is here defined by [117, 126]

$$\bar{\mathcal{F}}(\mathcal{U}, U) = \int \mathrm{d}\psi \, \langle\psi|U^\dagger \mathcal{U}(|\psi\rangle\langle\psi|)U|\psi\rangle \,, \tag{7.1}$$

where the integral is over the uniform Haar measure $\mathrm{d}\psi$ on state space, normalized so that $\int \mathrm{d}\psi = 1$. $\bar{\mathcal{F}}(\mathcal{U}, U) \leq 1$ and $\bar{\mathcal{F}}(\mathcal{U}, U) = 1$ if and only if $\mathcal{U}$ implements U perfectly. $\bar{\mathcal{F}}(\mathcal{U}, U)$ for single qubit gates can be expressed, using experimentally accessible quantities, as

$$\bar{\mathcal{F}}(\mathcal{U}, U) = \frac{1}{2} + \frac{1}{12} \sum_{j=1,2,3} \mathrm{Tr}\left[U\sigma_j U^\dagger \mathcal{U}(\sigma_j)\right] , \tag{7.2}$$

where σ_j is the Pauli matrix.

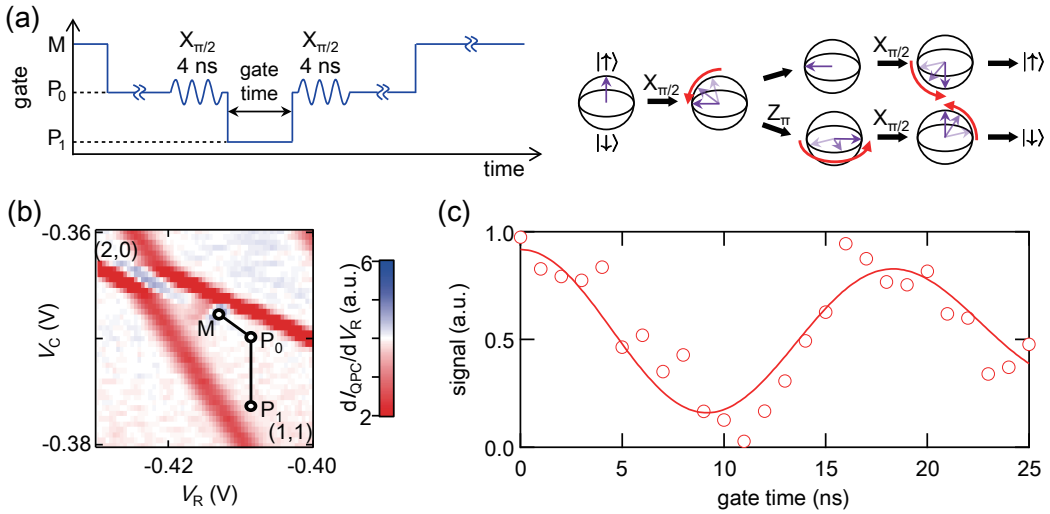

Figure 7.4: Demonstration of phase gate operation. (a) Pulse sequence and schematic representation in the Bloch sphere. The two ESR pulses map the phase flip to the bit flip. When the induced phase shift between these pulses is 0 the final spin state is the same as the initial state, whereas if it is phase flipped, the final spin state is (spin) flipped. (b) Specific gate voltage configuration used in the sequence. At M, $\varepsilon \approx 0$, and at P_0, $\varepsilon \approx -200\mu$eV, which should be enough to quench the exchange interaction. (c) Phase rotation at 54 MHz. The solid line is a least-square fit by $C + A\exp\left[-(t_{\rm gate}/T_2^Z)^2\right]\cos(2\pi f_Z t_{\rm gate})$, with $f_Z = 53.9$ MHz and $T_2^Z = 36.0$ ns.

sequence in order to rephase the unintended phase accumulation induced by the nuclear fluctuation. During the second interval, a voltage pulse is applied to perform a phase gate at various bias points of P_0 to P_3. The extracted oscillation frequency f_Z ranges from 0 to 40 MHz, depending on the bias points, or reflecting differences of local δB_Z. The quasi-linear dependence of f_Z on the pulse amplitude implies that our operation is performed as intended.

7.4.3 Discussion

The dephasing rate during the phase-shift gate operations is expected to coincide with the free induction decay rate with a characteristic time T_2^*, since the form of the Hamiltonian is essentially unchanged. Indeed, the extracted characteristic decay time $T_2^Z = 36$ ns for the 54 MHz phase gate is roughly consistent with $T_2^* = 94$ ns evaluated in the same device from measurement of

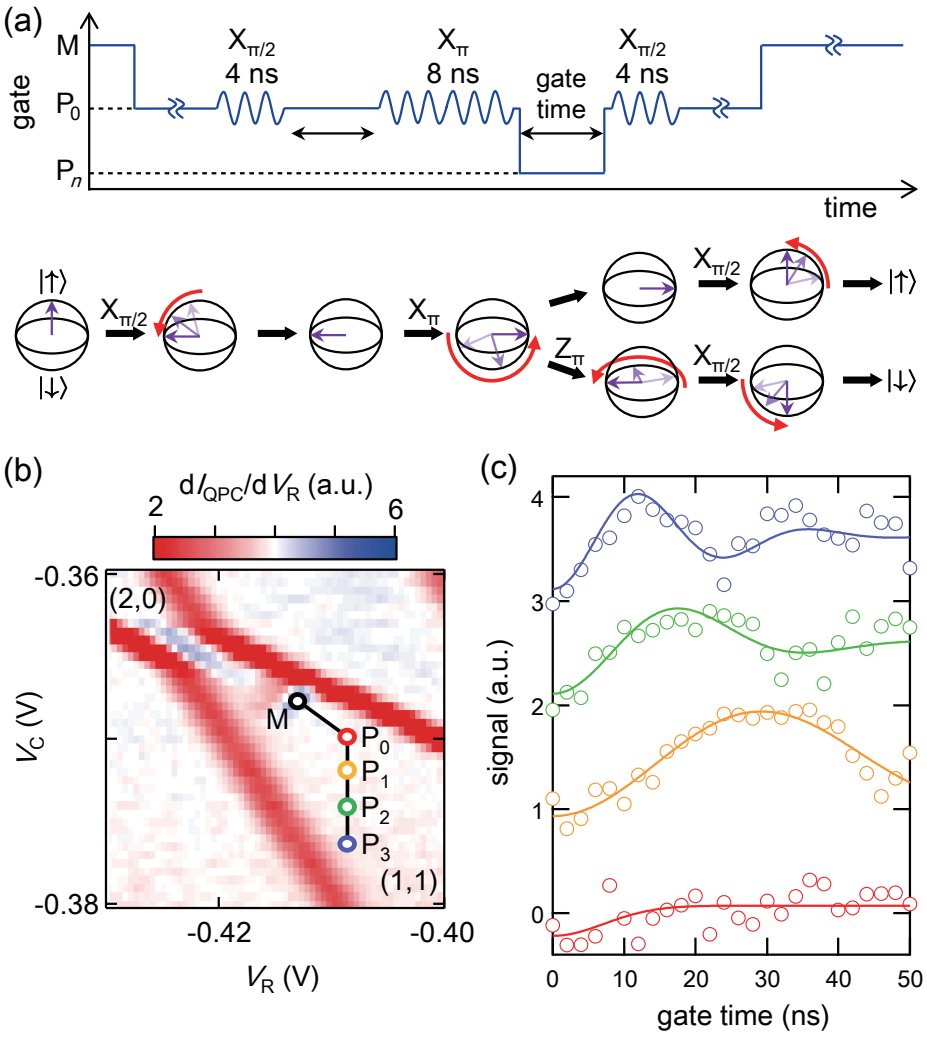

Figure 7.5: Amplitude dependence of phase gate operation. (a) The pulse sequence and the schematic representation in the Bloch sphere. Three ESR pulses are applied after an interval of gate time t_{gate} to rephase the unintended phase accumulation during the intervals, which could be there due to e.g. nuclear fluctuations. (b) Specific gate bias configuration. Points P_n $(n = 0, 1, 2, 3)$ are equally spaced in the gate voltage space. (c) Observed phase oscillation. The color indicates the gate bias P_n using the same color as in (b). Solid lines show best fits by $C + A\exp\left[-(t_{\mathrm{gate}}/T_2^Z)^2\right]\cos(2\pi f_Z t_{\mathrm{gate}})$. Signals are scaled using the fitting results of an independent 62.5 MHz ESR Rabi oscillation (see §5.4). Note that the trace for P_0 corresponds to the echo signal. Extracted values of f_Z are 16.3, 26.3 and 40.1 MHz, respectively for P_1, P_2 and P_3.

free induction decay during echo sequence (see §5.4.2.2 for details). Nevertheless we observe rapid damping of the "echoed" phase rotations in Fig. 7.5(c). The reason is not known at present, but it could be due to imperfection of ESR pulses, or the increased instability of the device.

7.5 Summary

In this chapter we propose and demonstrate single-step phase-shift gate operations of a single electron spin qubit. Our proposal for electrical phase control is to utilize a spatially distributed Zeeman field, which enables to turn on and off the phase accumulation by displacing the QD electron with gate voltage. From the pump-and-probe ESR spectra, the gate-induced change of the Zeeman field is measured to be as large as 12 mT in the strongly inhomogeneous stray field of a specially designed MM. Up to 54 MHz operation is revealed from observation of the direct phase rotation, using pulse sequences with additional x-rotations to map the phase rotation to spin rotation. Our phase gate has the ability to perform the so-called $\pi/8$ gate, or the z-rotation by $\pi/4$, in 2.3 ns. This is an order of magnitude shorter than T_2^* and is less than half the gating time of the same gate implemented in a conventional manner with 100 MHz ESR rotations. We anticipate that on the order of 100 MHz z-rotation will be feasible with optimized, larger gate pulses. The single-step phase gates demonstrated here will pave the way to experimental realization of various complicated quantum circuits of single spin qubits such as the state tomography of a single electron spin and CNOT.

Chapter 8

Toward Expansion to a Three Qubit System

Realization of a three-qubit system would be a milestone for fault-tolerant quantum computation with QDs, as quantum error correction of either a bit or a phase error requires at least three qubits. With a view to realizing three single-spin qubits in QDs, we endeavor to extend the MM technique to a three-qubit system. By incorporating the technique of radio-frequency (rf) reflectometry, we obtain a sufficient conductance sensitivity of the readout circuit to perform a single-shot spin measurement as well as fast device characterization. A TQD is tuned to a charge configuration relevant for qubit operations and shows fine gate tunability of the dot energy levels. Pump-and-probe measurements are conducted, and the possible causes of and remedies to the lack of spin-related signals are discussed.

8.1 Introduction

Although essential building blocks for universal computation with spins in QDs have been demonstrated experimentally, to date the number of QD-based spin qubits is limited to two [72, 127]. Extending to a TQD hosting three qubits is a natural step toward a scalable multi-qubit system and will open the door to the three-qubit error-correcting codes, the simplest code of their kind, which can correct any single bit- or phase-flip error of one of the physical qubits, depending

on the choice of the code, by encoding a qubit state using an entangled three-qubit state [9].

The TQD system has been actively studied recently. Following the observation of a charge stability diagram of a few electron TQD [36], the conductance through a TQD, including the tunneling event due to a QCA effect (see §2.3.2), was measured [34, 37] and device designs with greater tunablility [39, 128] or with compatibility with the MM technique [63] were extensively examined. Then the single-qubit operation and tomography using a three-spin state as a qubit [46, 50] as well as the coherent control of three spin states [52] employing the Landau-Zener-Stückelberg interferometry [129] have been demonstrated. Very recently, PSB has been observed in both two- and three-terminal TQD devices [38, 51]. Interactions between distant dots have been shown to play a role under some conditions [130, 131]. The response to MW irradiation is also investigated [132], whose understanding is important in performing ESR.

Although we use a gate geometry similar to those in these pioneering works, our approach presented here is unique in that a MM is incorporated so that each single-spin qubit can be accessed independently. The addressable ESR is a must to implement a three-qubit system with a TQD. This is because in the conventional scheme the single qubit is coded by well-defined single-qubit gates in a multi-qubit system.

8.2 MM Effect on Three Spin States

For high-fidelity qubit operations the difference of the local Zeeman field needs to be much larger than the hyperfine coupling (see §4.3). Here we theoretically study how the enhanced inhomogeneous magnetic field induced by a proximal MM affects the energy spectra of the TQD spin states.

The effective Hamiltonian of the three spin states confined in a series-coupled singly-occupied TQD subject to the MM stray field can be approximated (except near level crossing points) as [50]

$$\mathcal{H}_{\mathrm{TQD}}(\epsilon) = J_{12}\left(\boldsymbol{S}_1 \cdot \boldsymbol{S}_2 - \frac{1}{4}\right) + J_{23}\left(\boldsymbol{S}_2 \cdot \boldsymbol{S}_3 - \frac{1}{4}\right) + \mathcal{H}_{\mathrm{Z}}, \tag{8.1}$$

where $\boldsymbol{S}_i$ is the spin operator of the spin in the i-th QD, J_{ij} is the exchange cou-

pling between the spins in the i-th and j-th QDs and $\mathcal{H}_{\rm Z}$ describes the Zeeman energies. $J_{12}(J_{23})$ is induced by the tunnel couplings $t_{{\rm c},12}(t_{{\rm c},23})$ between QD1(2) and 2(3), and a function of the level-detuning ε, which is defined as half the electrostatic potential of the QD3 state relative to that of QD1 (Fig. 8.1(a)). By introducing $E_{\rm Z}$ as the Zeeman energy at QD2 and $\Delta_{12}(\Delta_{23})$ as the Zeeman energy difference between QD1(2) and QD2(3), the last Zeeman term of Eq. (8.1) can be expressed as

$$\mathcal{H}_{\rm Z} = E_{\rm Z}\sum_i S_{z,i} - \Delta_{12}S_{z,1} + \Delta_{23}S_{z,3}. \tag{8.2}$$

Figure 8.1 illustrates the simulated energy diagrams of the three spin system for representative parameter sets, and the effect of the inhomogeneous Zeeman field. When $\Delta_{12} = \Delta_{23} = 0$, as discussed in §3.1.3, the eight eigenstates are the four quadruplets $|{\rm Q}_{S_z}\rangle$ with $S_z = \pm 3/2, \pm 1/2$ and the four doublets $|\Delta^{\pm}_{S_z}\rangle$ with $S_z = \pm 1/2$ (see the rightmost panels in Fig. 8.1(c) and (d)). The energy of the doublet states $|\Delta^{\pm}_{S_z}\rangle$ with respect to that of the quadruplet state with the same S_z is obtained as $-(J_{12} + J_{23} \mp \sqrt{{J_{12}}^2 + {J_{23}}^2 - J_{12}J_{23}})/2$. Therefore these states can be mixed only when both J_{12} and J_{23} are suppressed and the energy difference becomes comparable to Δ_{12} or Δ_{23}. In conventional TQD devices without a MM, Δ_{12} and Δ_{23} are determined by the nuclear field, which is usually small and fluctuates in time. In contrast, we design these values as large as 1-2 μeV (corresponding roughly to a field difference of 50 - 100 mT in GaAs QDs), to achieve fast but addressable ESR. This is not only much larger than the hyperfine coupling, but can even compete with or overwhelm the exchange energies deep in the Coulomb blockade region (see the leftmost panels in Fig. 8.1(c) and (d)). Indeed, the spin Hamiltonian being dominated by the Zeeman terms is a necessary condition to avoid exchange interactions from being "always on" (which would complicate the calculation in the conventional framework).

In this "Zeeman-dominated" regime, it is appropriate to start with the eigenstates of $\mathcal{H}_{\rm Z}$ and then treat the tunneling effect as a perturbation. As a result, the energy diagram and the eigenstates deviate from those when exchange interactions dominate. If we assume that the Zeeman energy is smallest in QD1, and largest in QD3 for simplicity, $|{\downarrow}{\uparrow}{\uparrow}\rangle$ is the unperturbed ground state

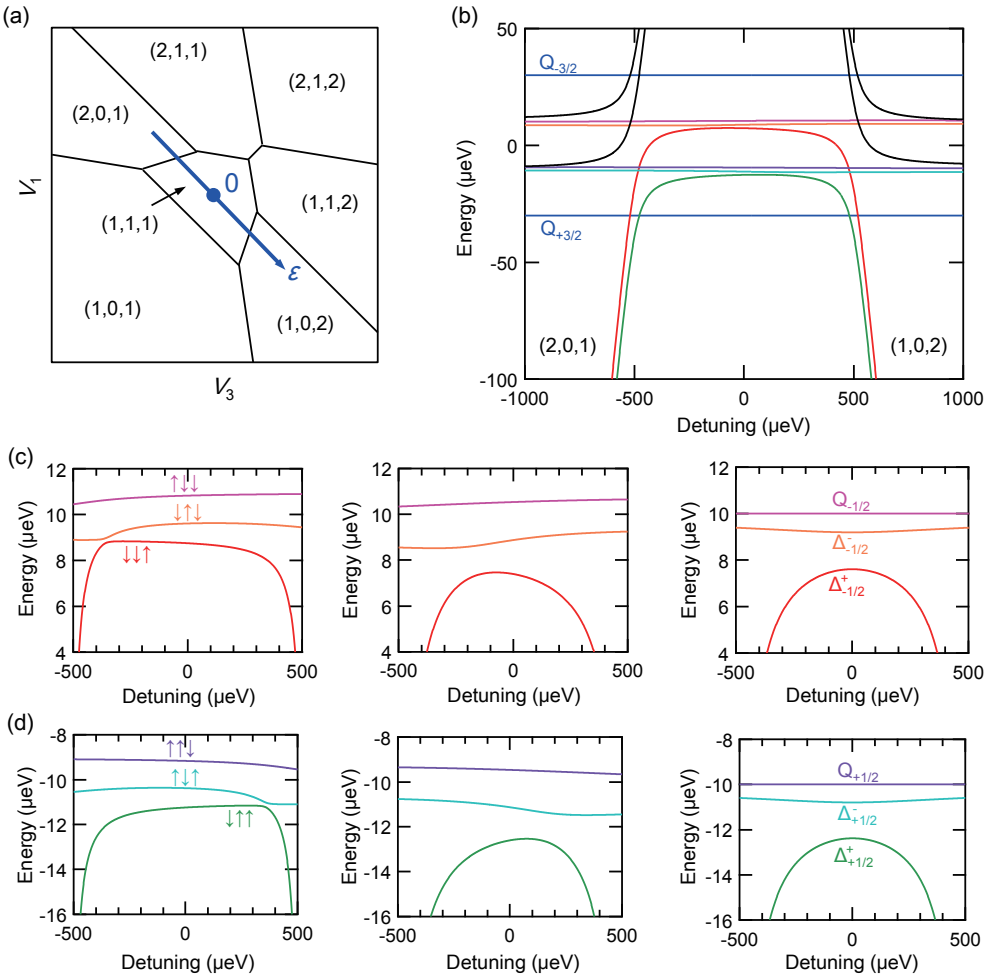

Figure 8.1: Three-electron spin energy diagrams. For simplicity, we restrict ourselves to the symmetric case with $t_{c,12} = t_{c,23}$ ($\equiv t_c$) and $\Delta_{12} = \Delta_{23}$ ($\equiv \Delta_Z$). (a) TQD stability diagram around the (1,1,1) region, with the level-detuning axis. (b) Three-spin energy diagram as a function of detuning, simulated for $E_Z = 20$ μeV, $\Delta_Z = -1$ μeV, $t_c = 20$ μeV. The size of the (1,1,1) region is set to be 1 meV. Due to suppressed exchange interactions the spectrum becomes dense near $\varepsilon = 0$. (c) Comparison of $S_z = -1/2$ energy diagrams in the (1,1,1) region for different parameters. $(\Delta_Z, t_c) = (-1\ \mu\text{eV}, 10\ \mu\text{eV})$, $(-1\ \mu\text{eV}, 20\ \mu\text{eV})$ and $(0\ \mu\text{eV}, 20\ \mu\text{eV})$ in the left, middle and right panel, respectively. In the left panel, the transition from the Zeeman-dominated domain to the exchange-dominated domain is marked by an avoided crossing located at $\varepsilon \approx -360$ μeV. For parameters used in the left panel, each eigenstate at $\varepsilon = 0$ is well approximated by a single Zeeman eigenstate, with the (Uhlmann) state fidelity > 90 %. On the other hand, for parameters used in the center panel, the fidelities are in the range of 47 - 83 %. (d) Same type of comparison for $S_z = 1/2$ states.

within the $S_z = 1/2$ subspace. Exchange interaction between the leftmost pair mixes this state with the first excited state $|\uparrow\downarrow\uparrow\rangle$, indicating the hybridized state of these two will form the new ground state as J_{12} gets large. On the other hand, this ground state is decoupled from the exchange interaction between the rightmost pair, as it cannot (virtually) tunnel to the (1,0,2) states due to the Pauli exclusion principle. This means that there must exist a level crossing with a superposition state of the other states in the $S_z = 1/2$ subspace as J_{23} increases. The same argument applies for the $S_z = -1/2$ subspace, with interchange of QD1 and QD3.

From Fig. 8.1(b) and (d) we see that for $|\Delta_Z| = 1$ μeV, $t_c = 20$ μeV is so large that the exchange coupling is not quenched even at $\varepsilon = 0$ (the detuning range, or the size of the (1,1,1) region, is limited by the finite charging energy, typically to the value on the order of 1 meV in GaAs QDs). When t_c is reduced to 10 μeV (Fig. 8.1(c)), the spin-spin interaction is dominated by the Zeeman terms and single-qubit states are not mixed near $\varepsilon = 0$. We can enter the region where the exchange coupling is dominant by moving toward charge boundaries, implying single- and two-qubit gate operations are compatible for this set of parameters. We note that achieving the Zeeman-dominated condition by substantially reducing t_c may not be favorable for fast entangling gates.

8.3 Measurement Setup

The measurement setup used in Chapters 5-7 is not capable of acquiring a number of stability diagrams (of a 3-dimensional nature [34,37,132]) necessary for tuning a TQD on reasonably short timescales. With a view to performing high-fidelity readout which will be involved in qubit experiments, here we implement the methods pioneered in refs. [133, 134] to observe charge dynamics rapidly.

8.3.1 Theory of Reflectometry Circuit

In the "conventional" d.c. charge sensing, the current through the sensor is monitored with a current-voltage (I-V) convertor at room temperature. The measurement bandwidth is limited to several tens of kHz because of the low-pass

filter (LPF) formed by the parasitic capacitance C_p (due to the measurement wires etc.) and the input impedance of the amplifier [135]. By using a cryogenic HEMT amplifier (and thus reducing C_p) the bandwidth can be increased up to 1 MHz [136], but this method is still limited by the LPF formed by C_p. An approach that circumvents this low-passing effect is to use an impedance matching network to transform the high resistance of the detector to roughly the $Z_0 = 50$ Ohm characteristic impedance of a transmission line [133]. High measurement bandwidth is achieved by applying this rf-reflectometry technique to the QPC charge sensing (rf-QPC) [134], allowing for single-shot spin-to-charge readout of a few-electron DQD [125]. The technique is applicable to an SET with possibly higher sensitivity as a charge sensor (rf-SET) [4], which enables single-shot spin measurement in ~ 100 ns with a signal-to-noise ratio (SNR) ~ 3 [31].

In rf-QPC, a QPC is embedded in an impedance matching network formed by a chip inductor of L and the parasitic capacitance of the bond pads and wires (Fig. 8.2(a)). We can express the frequency-dependent impedance of the model circuit as

$$Z(\omega) = i\omega L + \frac{R}{1 + i\omega R C_\mathrm{p}}. \tag{8.3}$$

$Z(\omega)$ approaches Z_0 at the resonance (angular) frequency

$$\omega_\mathrm{res} = \frac{1}{\sqrt{LC_\mathrm{p}}}\sqrt{1 - \frac{L}{2C_\mathrm{p}}(G^2 + {G_\mathrm{m}}^2)}, \tag{8.4}$$

where $G_\mathrm{m} = Z_0 C_\mathrm{p}/L$ is the conductance of the sensor resistor for the matching circuit to be perfectly impedance matched on resonance. The reflected power from the circuit is proportional to the square of the reflection coefficient $\Gamma(\omega) = (Z_0 - Z^*(\omega))/(Z_0 + Z(\omega))$, which can be calculated as [128]

$$|\Gamma(\omega)|^2 = 1 - \frac{4GG_\mathrm{m}}{(G + G_\mathrm{m})^2\left[1 - \frac{L}{4Cp}(G - G_\mathrm{m})^2\right] + L^2{C_\mathrm{p}}^2(\omega^2 - {\omega_\mathrm{res}}^2)^2}. \tag{8.5}$$

If we Taylor expand $|\Gamma(\omega_\mathrm{res})|^2$ around G_m we get

$$|\Gamma(\omega_\mathrm{res})|^2 \simeq \frac{1}{4{G_\mathrm{m}}^2}\left(1 - Z_0 G_\mathrm{m}\right)(G - G_\mathrm{m})^2, \tag{8.6}$$

which implies that the signal is actually relatively insensitive to conductance changes around $G_{\rm m}$. As the pre-factor scales almost as $1/{G_{\rm m}}^2$ (note that $Z_0 G_{\rm m} \ll 1$), the response away from the matching conductance becomes sharper with a lower $G_{\rm m}$.

8.3.2 Characterization of the Circuit Performance

We install in our Triton dry fridge the setup for rf reflectometry as illustrated in Fig. 8.2(b) and (c). With a test TQD device mounted, we first monitor the reflected rf carrier power with a network analyzer, and observe a dip when the QPC conductance $G_{\rm QPC}$ approaches the matching conductance (Fig. 8.3(a)). From a resonance frequency of 277.7 MHz and given $L = 560$ nH (here the left sensor channel is used in Fig. 8.2(b)), we can estimate $C_{\rm p} \approx 0.58$ pF from Eq. (8.4). The lumped-element model described in §8.3.1 predicts the matching resistance of 19 kOhm, which is consistent with the observation. We then use the demodulation circuit to obtain signals $V_{\rm rf}$ proportional to the reflected voltage. The relation between $V_{\rm rf}$ and the QPC current $I_{\rm QPC}$ is obtained by monitoring these signals simultaneously, yielding a quasi-linear dependence as shown in Fig. 8.3(b).

We evaluate the readout sensitivity following the procedure described in ref. [134]. The performance of the reflectometry setup can be assessed, independently of the device sensitivity, by the conductance sensitivity S_G. S_G can be determined experimentally by observing the amplitude modulation (AM) spectrum of the reflected signal under gate-voltage modulation. When we excite one of the surface gate voltages, two sidebands which are symmetric about the carrier frequency are observed, reflecting the modulation of $G_{\rm QPC}$, $\Delta G_{\rm QPC}$, at the modulation frequency. The spectral power of the sidebands is proportional to $\Delta G_{\rm QPC}$, which is not the case with the center band. SNR for a given bandwidth Δf is then obtained by the ratio of the height of a sideband to the noise floor, where Δf is given by the resolution bandwidth of the spectrum analyzer. We can then obtain S_G from

$$S_G = \frac{1}{2} \Delta G_{\rm QPC} \, (\Delta f)^{-1/2} \, 10^{-{\rm SNR}/20}, \tag{8.7}$$

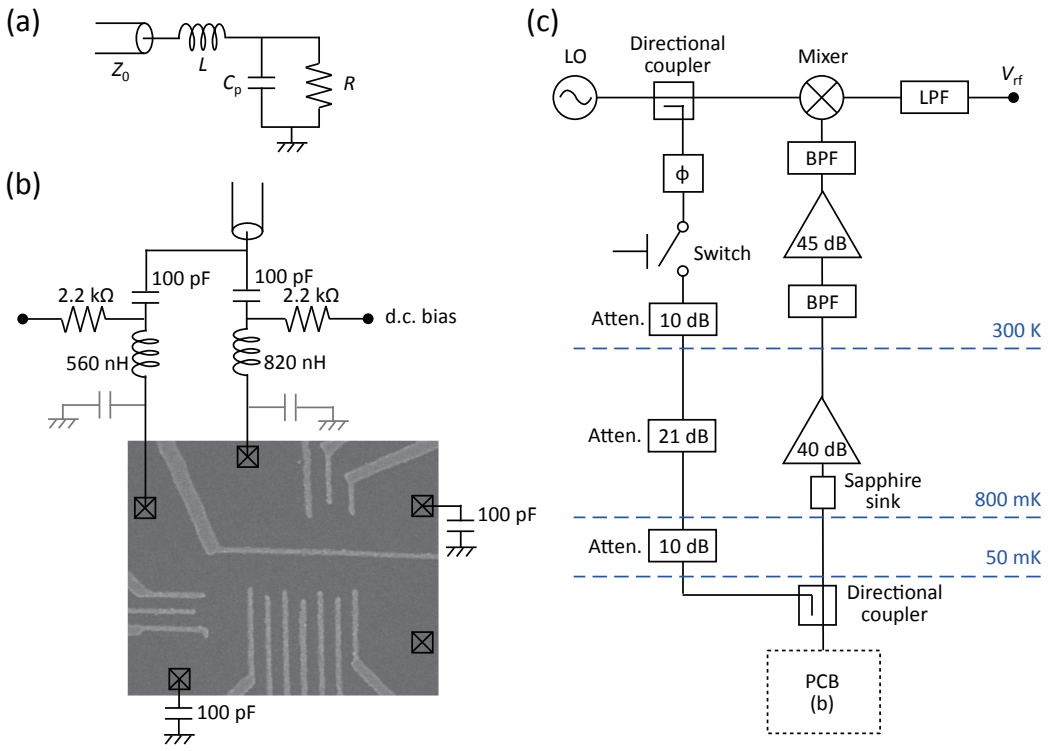

Figure 8.2: Reflectometry circuit. (a) L-network model that transforms the high resistance of the sensor R using the stray capacitance C_p and the inductance L toward the characteristic impedance of the transmission line Z_0. (b) Device and the surface-mount elements on the printed circuit board (PCB). Two matching circuits with different coils (and thus different resonance frequencies) are used for frequency-multiplexed readout of two sensor channels [50]. The bias-tees consisting of a capacitor and a resistor enable d.c. measurement. (c) Cryogenic and room-temperature measurement circuit. An rf carrier is applied to the device via a directional coupler (Minicircuits ZEDC-15-2B), which transmits solely the reflected signal with low loss to the cryo-amplifier (Caltech CITLF1) mounted at 800 mK. The phase shifter (Pulsar Microwave SO-06-411) shifts the phase of one of the split carrier signals before applied to the device, so that the reflected voltage becomes in phase with the other split part of the carrier signal at the mixer (Minicircuits ZP-3MH-S). If desired, the RF switch (Minicircuits ZASWA-2-50DR+) can blank the rf voltage, helping to conduct experiments using pulse sequences with a small dwell-time ratio at the readout stage as well as to reduce the back-action.

where the factor 1/2 comes from the number of sidebands and the unit of SNR is dB. From a 1 MHz AM spectrum we obtain $S_G = 10 \times 10^{-6}$ $(e^2/h)/\sqrt{\text{Hz}}$, which is comparable to the value of 5×10^{-6} $(e^2/h)/\sqrt{\text{Hz}}$ reported in ref. [134] (we note that a smaller S_G gives better sensitivity). Given S_G, the integration time t_{M} necessary to measure a conductance change of ΔG_{QPC} with a desired SNR in dB is expressed as

$$t_{\text{M}} = 2\left(\frac{S_G}{\Delta G_{\text{QPC}}}\right)^2 10^{\text{SNR}/10}. \tag{8.8}$$

We note that this is valid only when t_{M} is longer than the system response time determined by the circuit bandwidth, which can be evaluated, for instance, by taking the SNR dependence of AM modulation frequency (Fig. 8.3(d)). Our reflectometry circuit (with $S_G = 10 \times 10^{-6}$ $(e^2/h)/\sqrt{\text{Hz}}$) therefore allows, for instance, a conductance change of 0.003 e^2/h to be detected in $t_{\text{M}} = 20$ μs with unity SNR (i.e. SNR = 0 dB), which would be fast enough to perform single-shot spin detection.

8.4 Device Characterization

8.4.1 Device and the Simulated Magnetic Field

Figure 8.4(a) shows the TQD device measured. The plunger gates are connected to the high frequency lines (18 GHz-bandwidth) so that we can conduct pump-and-probe measurements. Gate S is chosen as the MW gate, because it is expected to have more or less the same lever-arms to all QDs. The MM is designed following the scheme proposed in Chapter 4, and guarantees $b_{\text{sl}}(\equiv \partial B_x/\partial z) \gtrsim 0.7$ mT/nm and $\Delta B_{\text{Z}} \gtrsim 25$ mT. The former is required for fast ESR, while the latter protects the qubit from ESR-crosstalk and exchange couplings and thus realizes high-fidelity single-qubit operations.

The upper charge sensor channel, operated as a QPC or an SET, is incorporated into a matching circuit formed by $L = 820$ nH and $C_{\text{p}} \sim 0.57$ pF. It resonates at 233.3 MHz when all sensor gates are negatively biased enough. We find out that the resonance frequency can be modulated by up to 6 MHz, depending on the choice of gates to deplete the channel. This is presumably

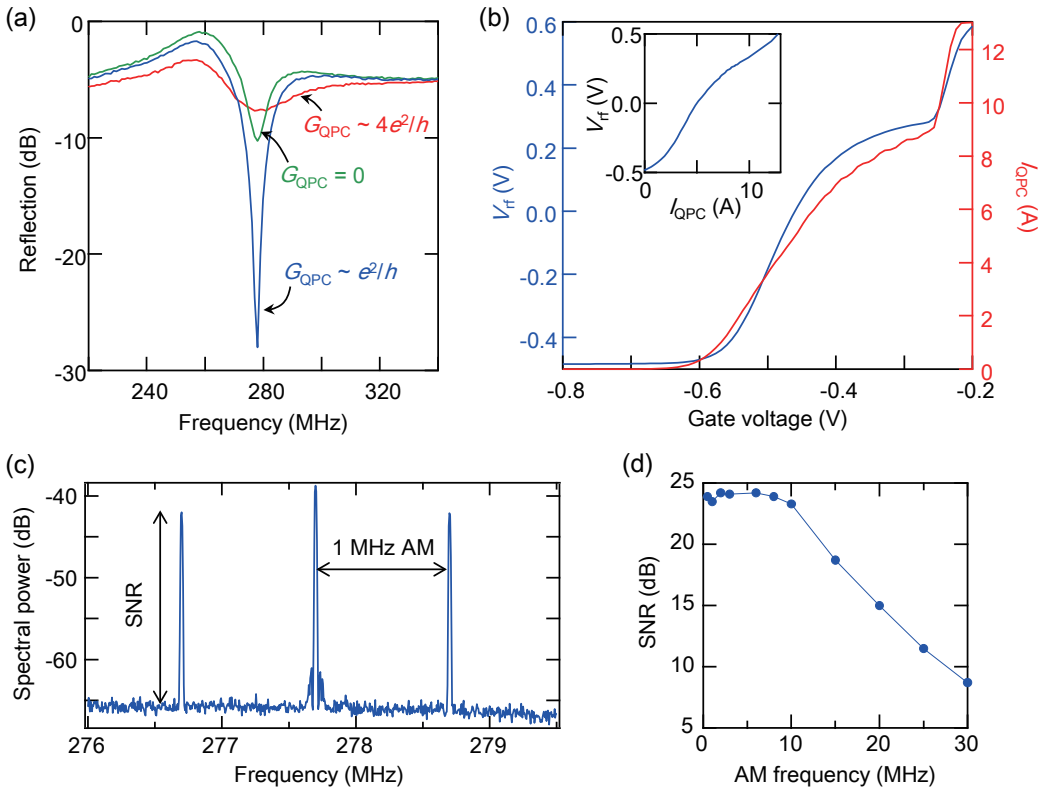

Figure 8.3: Characterization of the reflectometry circuit. (a) Reflection coefficient from the tank circuit for different g_{QPC}. Reflection signal at resonance is minimized around $g_{\mathrm{QPC}} \sim e^2/h$ and recovers as the QPC is further pinched off. (b) Demodulated response V_{rf} as a function of the QPC gate voltage, with the d.c. current. Inset shows transfer function of V_{rf} against I_{QPC}. (c) AM response of the reflected signal to 1 MHz gate modulation. SNR $= -24$ dB for $\Delta f = 10$ kHz and $\Delta g_{\mathrm{QPC}} = 0.032e^2/h$ estimated from the gate lever-arm. The estimated carrier power at the board is -80 dBm. (d) SNR as a function of modulation frequency. Above ~ 10 MHz, the Q factor of the impedance matching circuit limits the SNR and thus the measurement bandwidth.

because the geometric capacitance between the Schottky gates and the 2DEG (estimated to be $\sim$ 9 fF from the 10 μm^2 area size) adds to the effective C_p when the resistance between the coil and the 2DEG underneath the gate is low. We believe that this gate-tunablility can be an alternative to the varactor diode technique [137] to *in-situ* tune the resonance condition away from destructive interference due to the standing wave in the readout setup. Our technique is advantageous in that it requires no extra components to install and can minimize an undesirable increase of C_p.

8.4.2 TQD Stability Diagram

Figure 8.5(a) shows the TQD stability diagrams in the few electron regime. To boost our characterization speed, we use a digitizer (AlazarTech ATS9440) to record a time trace of the charge sensing signal V_rf synchronously with a low-frequency ($\sim$ 1 Hz) saw-tooth modulation to V_PL, from which we deduce the V_rf dependence on V_PL [134]. This "ramped" measurement is possible owing to the high-bandwidth of the rf-reflectometry readout and allows us to obtain a diagram in a minute, which is roughly a 10-fold time-saving compared with the conventional d.c. data taking. This way, the few electron regime can be reached in a relatively straightforward manner. The acquisition time of a diagram is limited by the ramping rate which cannot exceed the tunneling rates to measure a charge configuration at equilibrium.

To evaluate the device tunability we probe the 3D nature of the TQD stability diagram by tuning V_PC and taking the slice at the V_PL-V_PR plane. In this way we can cover the whole V_PL-V_PC-V_PR 3D gate voltage space. Figure 8.5(b) gives an example of such measurements, where the position of the middle-dot charging line is changed by V_PC, allowing for fine and independent tuning of the size of the (1,1,1) region. This confirms that in our device geometry the plunger gates can shift the energy level of each dot quite efficiently and selectively, which is crucial for pump-and-probe measurements.

8.4.3 Pump-and-Probe Measurements

Unlike DQDs or three-terminal TQDs [35, 38], detecting PSB in the conventional bias spectroscopy in a two-terminal TQD can be intricate [51]. To observe

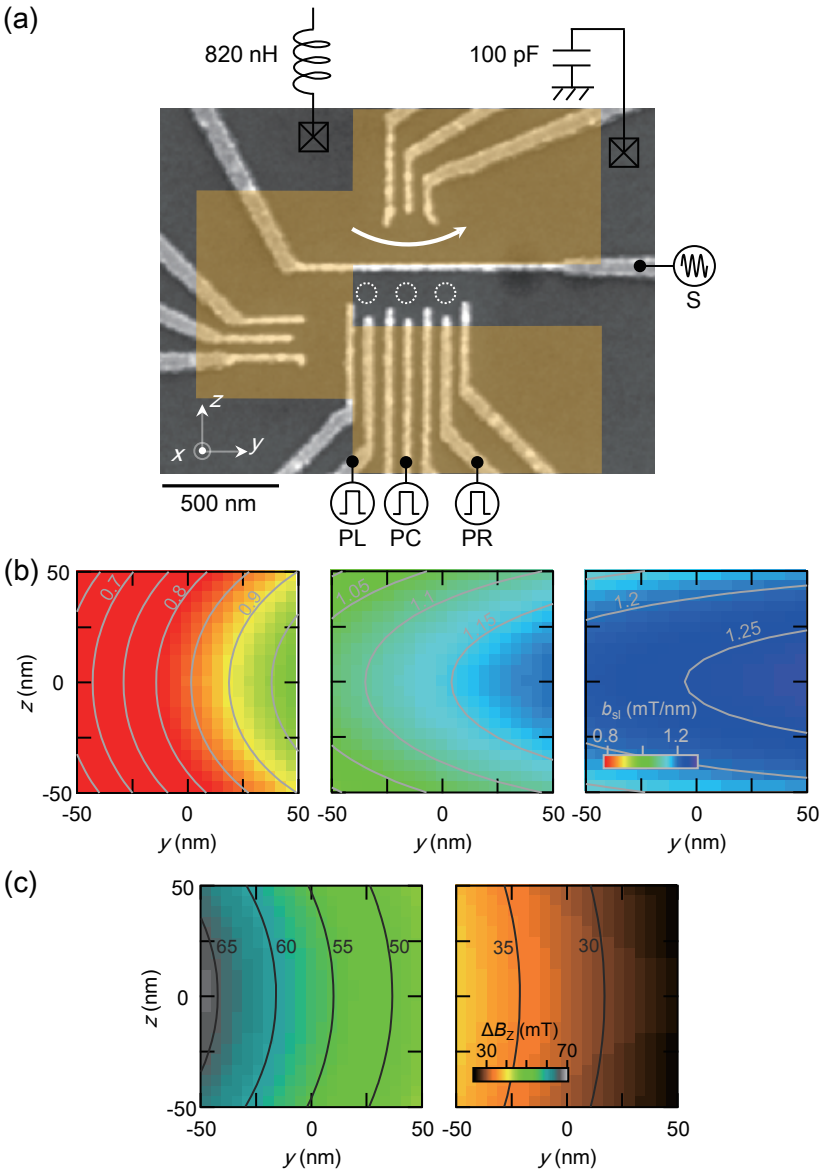

Figure 8.4: TQD device structure and simulated stray fields. (a) Scanning electron micrograph image of a similar device measured with the shape of a Co MM false-colored orange. The heterostructure (13729) is grown by the group of A.D. Wieck at Ruhr-Universität Bochum. The axes used in the main text are also shown. High frequency pulses can be applied on gates PL, PC, PR and S. (b) Numerically simulated distribution of the slanting field b_{sl} at each QD position. (c) Numerically simulated distribution of the local Zeeman field, between the left and middle QD (the left panel) and the middle and right QD (the right panel). The axes origin is at the center of the two relevant QDs.

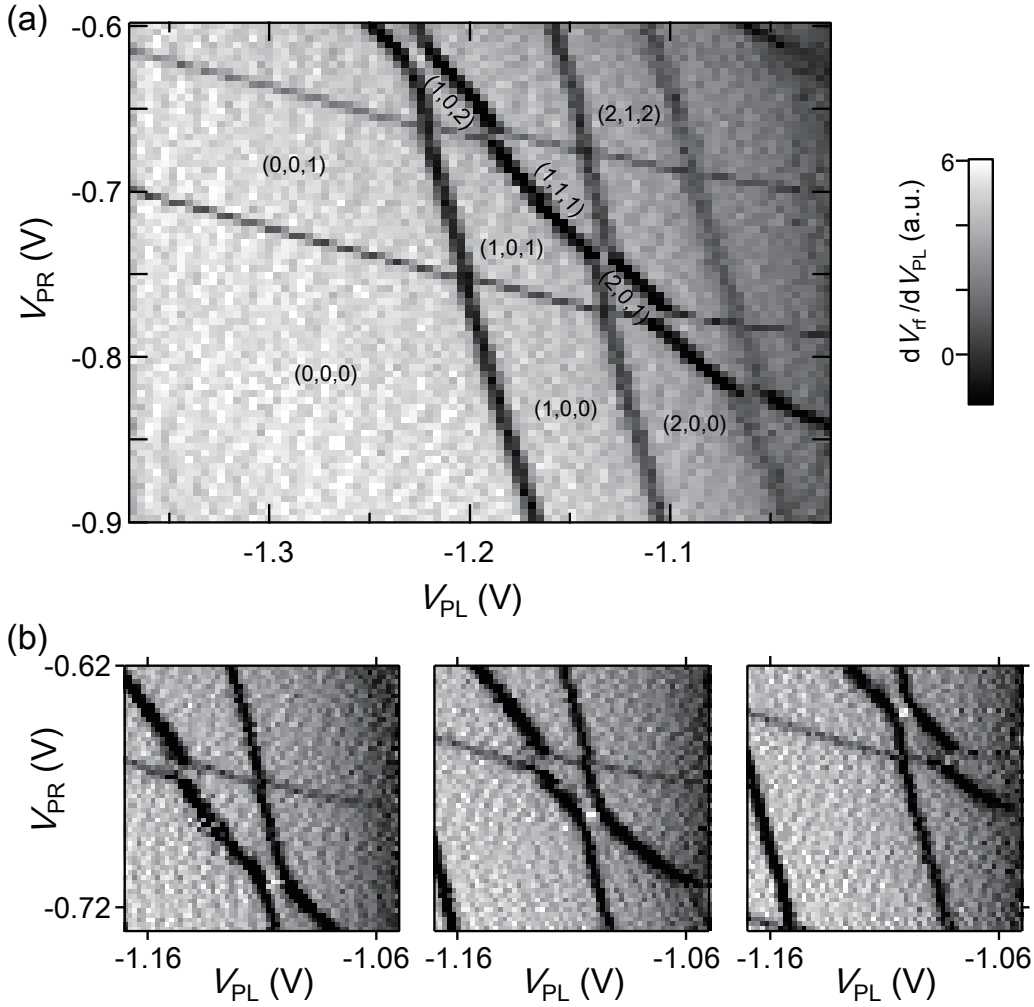

Figure 8.5: Few-electron TQD stability diagrams. (a) Diagram for charge assignment. The formation of a TQD is evident from the third slope of the transition line in the stability diagram. In the lower left region the charge transition lines are no longer observed, indicating that the TQD is completely empty. (b) Diagrams in the PL-PR voltage space as a function of the gate voltage of PC. The values of V_{PC} go from -1.32 to -1.36 V.

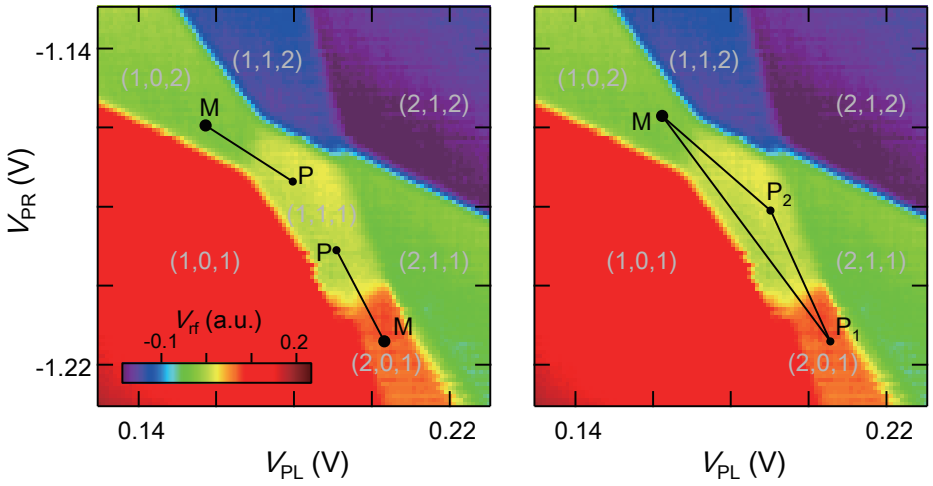

Figure 8.6: Examples of pulse sequences used in search of spin-related signals. M denotes the bias position during the measurement stage in the stability diagram. The two-stage pulses (the left panel) let the system evolve at P in the (1,1,1) region and measure the finding probability of (1,1,1) states. In the three-stage pulses (the right panel) another point P_1 in the (2,0,1) region is inserted before resting at P_2 in the (1,1,1) region to hopefully increase the initialization fidelity. A plane is subtracted from the original stability diagram to account for the gate leverarm.

spin-related phenomena such as PSB and ESR, we use instead the pump-and-probe technique [110], which has been used in refs. [46, 52, 138] to observe PSB under gate pulses. We try several types of pulse cycles with varying the dwell times or the voltage heights. Typical examples of sequences are shown schematically in Fig. 8.6. If the system is spin blocked, we expect V_{rf} measured either in the (1,0,2) or in the (2,0,1) region to approach the value for the (1,1,1) charge configuration only at finite magnetic fields. Unfortunately, however, we are yet to observe any conclusive spin-related signals. Our list of possible reasons includes 1) slow dot-lead and/or interdot tunneling rates with respect to the ramping rate or to the dwell time, 2) some trapping state which only relaxes in the slow co-tunneling processes, 3) fast spin relaxation at the readout stage due to Zeeman field gradients [139] and 4) imperfection of high-frequency pulses. It may be insightful to measure the interaction strength and the energy spectrum, for instance from the observation of a so-called spin-arch [52] to check the pulse (non-)adiabaticity conditions [129, 140].

8.5 Summary

In this chapter our attempt to realize a three-spin-qubit system is described. The rf-reflectometry technique for fast sensing is installed in our fridge and is demonstrated to yield a reasonably good conductance sensitivity of the readout setup, $10 \times 10^{-6}(e^2/h)/\sqrt{\text{Hz}}$. Our gate geometry as well as the fast data-acquisition technique facilitates to reach the (1,1,1) charge state neighbored by the (1,0,2) and (2,0,1) configurations, a regime of interest for implementing a three-qubit system. The device shows a satisfying tunability of the dot energy levels, a necessary ingredient for qubit operations. Unfortunately, spin-related signals are still elusive after trials of pump-and-probe measurements. Possible mechanisms and means are considered, with no fundamental obstacles found in the way toward our goal.

Chapter 9

Summary

This thesis focuses on single-electron spin qubits confined in GaAs quantum dots [6] and employs the micro-magnet technique [21] for high-fidelity qubit manipulation. The presented results can be summarized as follows.

1. We present a novel micro-magnet design to meet the requirements on the stray fields for high-fidelity spin control in the presence of a realistic amount of misalignment. (Chapter 4)

2. We find evidence of the strong inhomogeneous magnetic field by our tailored micro-magnet from an exceptionally large ESR peak separation of ~ 80 mT and above 120 MHz Rabi oscillations with a spin-flip fidelity of 97 %. (Chapter 5)

3. We demonstrate that the fast Rabi oscillations ($\gtrsim 40$ MHz) feature the zero oscillation phase shift and the exponential coherence decay, in clear contrast to the conventional breakdown of the Markovian Bloch equations by the strong coupling to a nuclear-spin bath. We also show that chevron patterns of the spin-flip intensity can be resolved in the time-spectral domain as an indication of the strong ESR drive. (Chapter 6)

4. We propose and demonstrate for the first time single-step phase-shift gate operations of a single electron spin qubit. We achieve above 50 MHz electrical phase rotation by utilizing the micro-magnet's inhomogeneous stray field. (Chapter 7)

We believe these improvements in controlling the coupled spin system will contribute to quantum information processing with electron spin qubits. The demonstrated fast single-qubit gating, together with the established rapid entangling gates, will make operation times necessary to implement fundamental quantum circuits much shorter than the ensemble phase coherence time T_2^*. The exponential coherence decay observed here may be integral to quantum error correction.

We anticipate that the ESR rotation speed can be doubled in future experiments by using a ferromagnet with stronger magnetization than cobalt and/or a thinner insulator (20 nm would be possible for instance with atomic-layer-deposition technology). We also expect that on the order of 100 MHz phase rotations will be feasible with optimized, larger gate pulses. Nuclear spin preparation [93,94,97–102] as well as dynamically error-corrected gates [141,142] may be combined to further improve the control fidelity in the nuclear spin bath.

The presented micro-magnet technique can be directly applied to quantum dots based on other materials, such as carbon nanotubes [26, 143–145], Si/Ge 2DEGs [56, 103, 146], or Ge/Si nanowires [147] where long coherence times are expected due to weak hyperfine interactions. Indeed, the large control fields (~ 20 mT) achieved here would implement single-qubit π-rotations within 1 ns in Si-based QDs (with $g \sim 2$), suggesting a fault-tolerant single-qubit gate fidelity [148] given the observed $T_2^* = 360$ ns [146] (the value would be further improved by isotope purification [103]).

Appendix A

Device Fabrication Recipe

A.1 Recipe Overview

Integrating magnets to QD devices obviously complicates device fabrication to a certain extent. Although it is a relatively straightforward extension of the conventional process for GaAs lateral QDs, our recipe for MM-QD devices involves as many as seven steps, so fabricating a new device usually means one week of work in the clean room. During my PhD course, lots of modifications were made as we learned better ways for higher yields. In this appendix, a recipe used for TQD devices with a MM is reviewed.

The first step fabricates alignment marks, needed to make all the following steps aligned with each other. Most importantly, one wants to overlay the gate electrodes and the micro-magnet within the specified precision of the ebeam machine, in our case (Exlionix ELS7700) 40 nm.[1] You may well skip the first step and combine it with the second by reducing the size of Ohmic contacts and changing the metal of alignment marks from Ti/Au to AuGe/Ni. However, marks fabricated in an independent step are more reliable especially when AuGe is thin or less visible after annealing.

The second step is to make Ohmic contacts. Note that the best rapid thermal annealing condition is different from wafer to wafer, so it needs retesting for each new wafer. This seems particularly important for wafers with low

[1] The wrong alignment strategy such as to use different chip sizes can easily spoil this accuracy.

2DEG carrier density, which are presumably suitable for making multiple QDs and/or low voltage operation. If the contact resistance is more than kOhms, it becomes difficult to perform sensitive charge sensing measurements.

The third step is to define the mesa, where the 2DEG layer is formed. This is the only step where photo-resist is used for patterning in our recipe. This is because ZEP is relatively weak against acid, and therefore not a good choice for wet etching. For rf-reflectometry measurement, it seems somehow important to etch the 2DEG thoroughly in terms of depth and/or area.

The fourth step fabricates fine gates. Here a thinner resist is used to properly deposit fine patterns and cold development technique is used for a better contrast. At the ebeam exposure, we first expose the core region and the rest, with all writing orders specified, to minimize the effect of the stage drift. For maximized alignment precision, we believe it is important that the core region be arranged at the chip center.

The fifth step is for bonding pads. The metal needs to be thick enough to electrically connect the gate on the mesa and the pad off the mesa. It is important to note that easily-broken pads can spoil the whole process.

The sixth step is Calixarene, an insulating layer between the gate and the MM. We use a solution of a mixture of Calix[6]-arene and Calix[9]-arene to monochloro-benzene, whose concentration is calibrated (through trial and error and color inspections) to 60 - 80 nm when spun twice. Monochloro-benzene needs to be added from time to time to obtain the same thickness. Two layers of Calixarene are necessary to avoid pinholes.

The final step fabricates the magnet. We use double layer ZEP simply to deposit cobalt thickly. The device must be kept in vacuum after deposition of the MM to avoid oxidization. We found that depositing a layer of gold on top of the MM did not help to reduce deterioration of Co.

A.2 Step-by-Step Recipe

Step 1. Mark

1. Cleave a 5 mm $\times$ 5 mm chip from the GaAs HEMT substrate.

2. Sonicate in Acetone for 3 mins, then in IPA for 3 mins for solvent cleaning.

3. Bake in an oven at 110 °C for 10 mins.
4. Spin ZEP 520A. Start at 500 rpm for 3 secs, ramp for 7 secs and keep at 4000 rpm for 50 secs. Thickness is typically 400 nm.
5. Bake on a hotplate at 180 °C for 3 mins, after cleaning the backside.
6. Expose with ebeam at 75 kV, with 60 pA for 1.0 - 1.8 μsecs, using 0.3 mm chips with a 60,000 dot resolution. Use OLA 1 and M 6 of our ELS7700.
7. Develop in Xylene at 20 °C for 30 secs, then rinse in IPA 30 secs.
8. Deposit Ti/Au = 30/170 nm at 1/3 Å/sec using ebeam.
9. Dip in NMP at 90 °C for ∼15 mins. Lift off with a pipette, and Acetone spray. Clean in Acetone and in IPA.

Step 2. Ohmic

1. Keep in Acetone for 3 mins, then in IPA for 3 mins for solvent cleaning.
2. Bake in an oven at 110 °C for 10 mins.
3. Spin ZEP 520A. Start at 500 rpm for 3 secs, ramp for 7 secs and keep at 4000 rpm for 50 secs. Thickness is typically 400 nm.
4. Bake on a hotplate at 180 °C for 3 mins, after cleaning the backside.
5. Expose with ebeam at 75 kV, with 2 nA for 4.0 μsecs, using a 1.2 mm chips with a 20,000 dot resolution. Use OLA 3 and M 3 of our ELS7700.
6. Develop in Xylene at 20 °C for 30 secs, then rinse in IPA 30 secs.
7. Deposit AuGe(12wt%)/Ni = 110/10 nm at 3/0.5 Å/sec using ebeam.
8. Dip in NMP at 90 °C for ∼15 mins. Lift off with a pipette, and Acetone spray. Clean in Acetone and in IPA.
9. Anneal in the H_2/N_2 atmosphere. Ramp to 420 °C in 2 mins, keep at 420 °C for 2 mins, and stop heating.

Step 3. Mesa

1. Keep in Acetone for 3 mins, then in IPA for 3 mins for solvent cleaning.
2. Bake in an oven at 110 °C for 10 mins.
3. Spin S1813. Start at 500 rpm for 3 secs, ramp for 7 secs and keep at 4000 rpm for 50 secs. Thickness is typically 1 μm.
4. Bake on hotplace at 90 °C for 5 mins.
5. Expose to UV for 15 secs, using a photo-mask.
6. Develop in S351:H_2O=1:5 for 60 secs. Clean in DI wafer (overflow) for 2 mins.
7. Bake in an oven at 110 °C for 20 mins.
8. Etch in H_3PO_4:H_2O_2:H_2O = 4:1:90, at 20 °C. Etching rate is typically 1 nm/sec. Aim for around 120 nm when the depth of the 2DEG is 100 nm, for example.
9. Remove resist in Acetone at 90 °C for 5 mins. Rinse in IPA.

Step 4. Gate

1. Keep in NMP at 90 °C for 3 mins, in Acetone at 90 °C for 3 mins, then in IPA for 3 mins for solvent cleaning.
2. Bake in an oven at 110 °C for 10 mins.
3. Spin ZEP 520A:Anisole = 1:1. Start at 500 rpm for 3 secs, and immediately keep at 5000 rpm for 50 secs. Thickness is typically 100 nm.
4. Bake on a hotplate at 180 °C for 3 mins, after cleaning the backside.
5. Expose with ebeam at 75 kV, with 60 pA for 7 μsecs (line) and 3 μsecs (dot/area), using 0.3 mm chips with a 60,000 dot resolution. Use OLA 1 and M 6 of our ELS7700. Use as mark A the one that is closest to the fine pattern, and as mark B the one that is far enough away, to maximize the alignment precision. If the liftoff of gate metal on the bumpy AuGe/Ni is problematic, the Ohmic area should be exposed as well.
6. Develop in Xylene at 5 °C for 30 secs, then rinse in IPA 30 secs.

7. Deposit Ti/Au = 10/20 nm at 0.5/0.7 Å/sec using ebeam.
8. Dip in NMP at 90 °C for ∼ 25 mins. Lift off with a pipette, and Acetone spray. Clean in Acetone and in IPA.

Step 5. Bonding Pad

1. Keep in Acetone for 3 mins, then in IPA for 3 mins for solvent cleaning.
2. Bake in an oven at 110 °C for 10 mins.
3. Spin ZEP 520A. Start at 500 rpm for 3 secs, ramp for 7 secs and keep at 4000 rpm for 50 secs. Thickness is typically 400 nm.
4. Bake on a hotplate at 180 °C for 3 mins, after cleaning the backside.
5. Expose with ebeam at 75 kV, with 2 nA for 4.0 μsecs, using 1.2 mm chips with a 20,000 dot resolution. Use OLA 3 and M 3 of our ELS7700.
6. Develop in Xylene at 20 °C for 30 secs, then rinse in IPA 30 secs.
7. Deposit Ti/Au = 20/220 nm at 0.7/3 Å/sec using ebeam.
8. Dip in NMP at 90 °C for ∼ 15 mins. Lift off with a pipette, and Acetone spray. Clean in Acetone and in IPA.

Step 6. Calixarene

1. Keep in Acetone for 3 mins, then in IPA for 3 mins for solvent cleaning.
2. Bake in an oven at 110 °C for 10 mins.
3. Spin diluted Calixarene. Start at 500 rpm for 3 secs, immediately[2] keep at 4000 rpm for 50 secs.
4. Bake on a hotplate at 180 °C for 5 mins, after cleaning the backside.
5. Spin diluted Calixarene (2nd layer). Start at 500 rpm for 3 secs, immediately keep at 4000 rpm for 50 secs. Thickness is typically 60-100 nm.[3]

[2]Skipping a 7 sec ramp makes the Calixarene considerably thinner.
[3]The thickness is indicated by the color.

6. Bake in an oven at 180 °C for 30 mins, after cleaning the backside.
7. Expose with ebeam at 75 kV, with 210 pA for 47 μsecs, using 0.15 mm chips with a 20,000 dot resolution. Use OLA 1 and M 9 of our ELS7700.
8. Develop in Xylene at 20 °C for 30 secs, then rinse in IPA 30 secs.

Step 7. Magnet

1. Keep in Acetone for 3 mins, then in IPA for 3 mins for solvent cleaning.
2. Bake in an oven at 110 °C for 10 mins.
3. Spin ZEP 520A. Start at 500 rpm for 3 secs, ramp for 7 secs and keep at 4000 rpm for 40 secs.
4. Bake on a hotplate at 180 °C for 3 mins, after cleaning the backside.
5. Spin ZEP 520A (2nd layer). Start at 500 rpm for 3 secs, ramp for 7 secs and keep at 4000 rpm for 40 secs. Total thickness is typically 800 nm.
6. Bake on a hotplate at 180 °C for 3 mins, after cleaning the backside.
7. Expose with ebeam at 75 kV, with 60 pA for 2.4 μsecs, using 0.3 mm chips with a 60,000 dot resolution. Use OLA 1 and M 6 of our ELS7700. Choose the same alignment marks as for the gate step whenever possible.[4]
8. Develop in Xylene at 20 °C for 30 secs, then rinse in IPA 30 secs.
9. Deposit Ti/Co = 10/250 nm at 0.7/1 Å/sec using ebeam.[5]
10. Dip in NMP at 90 °C for $\sim$ 15 mins.[6] Lift off with a pipette, and Acetone spray. Clean in Acetone and in IPA.

[4] To make this almost always possible, these marks are used exclusively for these two steps. In other steps other pairs of marks are used.

[5] The cobalt deposition takes more than half an hour, and if the thermal contact is bad the top plate of the evaporator heats up. This damages the resist and can make the liftoff problematic. Evaporation at higher rates can result in bad liftoff as well.

[6] Dipping in NMP for too long can damage cobalt and possibly Calixarene.

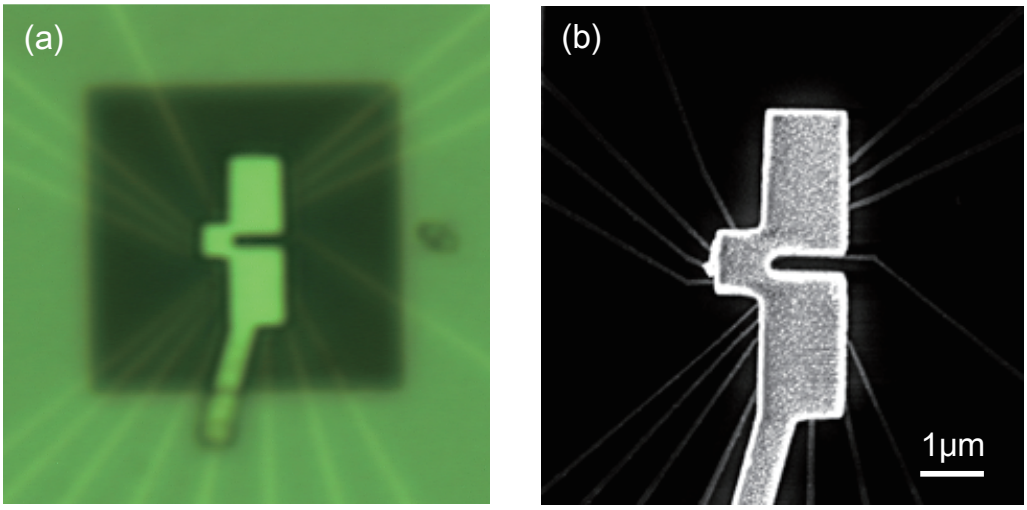

Figure A.1: Images of a completed MM-QD device. (a) Optical image of the core region. The Co MM is placed just above the QD, on top of a Calixarene layer (the dark square region) and is contacted with a Ti/Au electrode (yellow). The small patterns just on the right side of the core region are the alignment markers, from which to identify the overlay misalignment before and after Co deposition. (b) Scanning electron micrograph of the core region. The surrounding region is dark and opaque due to insulating Calixarene. No side walls are found, implying a successful lift-off process.

Appendix B

Simplified Wall-Wall Control Procedure

Tuning multiple QDs into a relevant regime can be a tedious job, especially when the right direction to take is in a complete darkness. Here we provide a very simple, yet somewhat helpful diagnostics of the relative tunnel couplings for a double QD in the sequential tunneling regime. A similar discussion based on the rate-equation model can be found in ref. [115].

When the source-drain bias is applied such that the chemical potential of the right reservoir is energetically higher than that of the left, electron (e) and hole (h) transport cycles near the $(N_{\rm L}, N_{\rm R})$-$(N_{\rm L}+1, N_{\rm R}-1)$ charge boundaries are (see §2.3.1)

$$\begin{aligned} \text{e}: \quad & (N_{\rm L}, N_{\rm R}) \xrightarrow{\Gamma_{\rm C}} (N_{\rm L}+1, N_{\rm R}-1) \xrightarrow{\Gamma_{\rm L}} (N_{\rm L}, N_{\rm R}-1) \xrightarrow{\Gamma_{\rm R}} (N_{\rm L}, N_{\rm R}) \\ \text{h}: \quad & (N_{\rm L}, N_{\rm R}) \xrightarrow{\Gamma_{\rm C}} (N_{\rm L}+1, N_{\rm R}-1) \xrightarrow{\Gamma_{\rm R}} (N_{\rm L}+1, N_{\rm R}) \xrightarrow{\Gamma_{\rm L}} (N_{\rm L}, N_{\rm R}). \end{aligned}$$

Here Γ_α ($\alpha = {\rm L}, {\rm R}, {\rm C}$) denote the tunneling rates of the left, right and center barriers, respectively. Average charge configurations in these bias triangles can

be modeled as

$$\begin{aligned} \text{e}: \quad & \left[{\Gamma_{\text{C}}}^{-1}(N_{\text{L}}, N_{\text{R}}) + {\Gamma_{\text{L}}}^{-1}(N_{\text{L}}+1, N_{\text{R}}-1) + {\Gamma_{\text{R}}}^{-1}(N_{\text{L}}, N_{\text{R}}-1)\right] / {\Gamma_{\text{tot}}}^{-1} \\ & = (N_{\text{L}}, N_{\text{R}}) + \left(\frac{{\Gamma_{\text{L}}}^{-1}}{{\Gamma_{\text{tot}}}^{-1}}, -\frac{{\Gamma_{\text{L}}}^{-1} + {\Gamma_{\text{R}}}^{-1}}{{\Gamma_{\text{tot}}}^{-1}} \right) \qquad \text{(B.1)} \\ \text{h}: \quad & \left[{\Gamma_{\text{C}}}^{-1}(N_{\text{L}}, N_{\text{R}}) + {\Gamma_{\text{R}}}^{-1}(N_{\text{L}}+1, N_{\text{R}}-1) + {\Gamma_{\text{L}}}^{-1}(N_{\text{L}}+1, N_{\text{R}})\right] / {\Gamma_{\text{tot}}}^{-1} \\ & = (N_{\text{L}}, N_{\text{R}}) + \left(\frac{{\Gamma_{\text{L}}}^{-1} + {\Gamma_{\text{R}}}^{-1}}{{\Gamma_{\text{tot}}}^{-1}}, -\frac{{\Gamma_{\text{R}}}^{-1}}{{\Gamma_{\text{tot}}}^{-1}} \right), \qquad \text{(B.2)} \end{aligned}$$

where ${\Gamma_{\text{tot}}}^{-1} = {\Gamma_{\text{L}}}^{-1} + {\Gamma_{\text{R}}}^{-1} + {\Gamma_{\text{C}}}^{-1}$. Let us denote by $\Delta I_{\text{L(R)}}$ the change of the sensor current, by a single charge in each QD. Then the change of the sensor current on the zero level detuning line (i.e. the bottom line of the bias triangles) is given by

$$\begin{aligned} \text{e}: \quad & \Delta I_{\text{e}} = \frac{{\Gamma_{\text{L}}}^{-1}}{{\Gamma_{\text{tot}}}^{-1}} \Delta I_{\text{L}} - \frac{{\Gamma_{\text{L}}}^{-1} + {\Gamma_{\text{R}}}^{-1}}{{\Gamma_{\text{tot}}}^{-1}} \Delta I_{\text{R}} \qquad \text{(B.3)} \\ \text{h}: \quad & \Delta I_{\text{h}} = \frac{{\Gamma_{\text{L}}}^{-1} + {\Gamma_{\text{R}}}^{-1}}{{\Gamma_{\text{tot}}}^{-1}} \Delta I_{\text{L}} - \frac{{\Gamma_{\text{R}}}^{-1}}{{\Gamma_{\text{tot}}}^{-1}} \Delta I_{\text{R}}. \qquad \text{(B.4)} \end{aligned}$$

In most cases, in the regime of interest $\Gamma_{\text{C}} \gg \Gamma_{\text{L}}, \Gamma_{\text{R}}$, so that ${\Gamma_{\text{tot}}}^{-1} \simeq {\Gamma_{\text{L}}}^{-1} + {\Gamma_{\text{R}}}^{-1}$. Then the above expressions are further simplified to

$$\begin{aligned} \Delta I_{\text{e}} &\simeq \frac{{\Gamma_{\text{L}}}^{-1}}{{\Gamma_{\text{L}}}^{-1} + {\Gamma_{\text{R}}}^{-1}} \Delta I_{\text{L}} - \Delta I_{\text{R}} \qquad \text{(B.5)} \\ \Delta I_{\text{h}} &\simeq \Delta I_{\text{L}} - \frac{{\Gamma_{\text{R}}}^{-1}}{{\Gamma_{\text{L}}}^{-1} + {\Gamma_{\text{R}}}^{-1}} \Delta I_{\text{R}}. \qquad \text{(B.6)} \end{aligned}$$

It is important to note that visibility of the zero detuning lines for electron and hole transport cycles can be different. Depending on the sensitivity ratio $\alpha_{\text{S}} = \Delta I_{\text{L}} / \Delta I_{\text{R}}$, and the tunneling rate ratio $\alpha_{\Gamma} = \Gamma_{\text{L}} / \Gamma_{\text{R}}$, the change can be vanishingly small. Figure B.1 illustrates the stability diagrams in some limiting cases.

From Eqs. (B.3) and (B.4), the visibility ratio $\alpha_{\text{V}} = \Delta I_{\text{e}} / \Delta I_{\text{h}}$ can be expressed as

$$\alpha_{\text{V}} = \frac{\alpha_{\text{S}} - \alpha_{\Gamma} - 1}{\alpha_{\text{S}} \alpha_{\Gamma} + \alpha_{\text{S}} - \alpha_{\Gamma}}, \qquad \text{(B.7)}$$

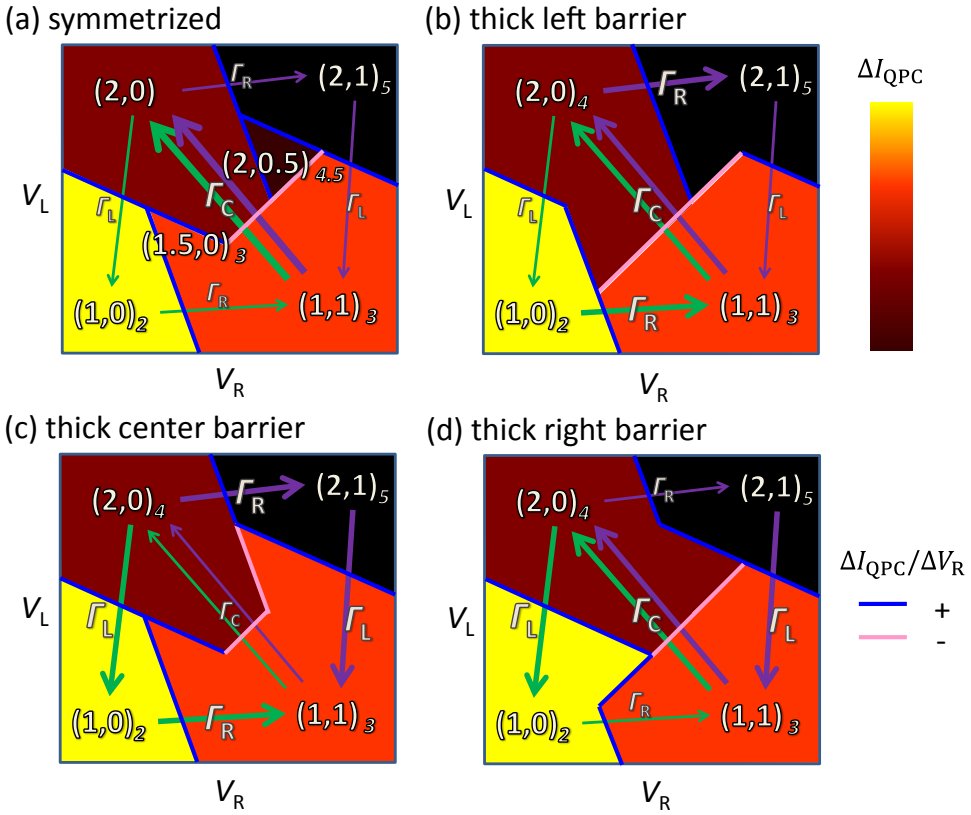

Figure B.1: Charge sensing signal maps for a quick tuning diagnosis. Diagrams are schematically shown in various limiting cases of relative barrier thicknesses: $\Gamma_{\mathrm{L}} \sim \Gamma_{\mathrm{R}} \ll \Gamma_{\mathrm{C}}$ ((a)), $\Gamma_{\mathrm{L}} \ll \Gamma_{\mathrm{R}} \lesssim \Gamma_{\mathrm{C}}$ ((b)), $\Gamma_{\mathrm{L}} \sim \Gamma_{\mathrm{R}} \gg \Gamma_{\mathrm{C}}$ ((c)) and $\Gamma_{\mathrm{R}} \ll \Gamma_{\mathrm{L}} \lesssim \Gamma_{\mathrm{C}}$ ((d)). The suffix numbers indicate the relative charge sensing signals when $\alpha_{\mathrm{S}} = 2$. When the transport is spin blocked, the diagram should look like (c).

from which α_Γ can be written as

$$\alpha_\Gamma = \frac{-\alpha_S \alpha_V + \alpha_S - 1}{\alpha_S \alpha_V - \alpha_V + 1}. \tag{B.8}$$

Since α_S and α_V can be independently measured from a stability diagram, α_Γ can be estimated from this expression.

References

[1] R. C. Ashoori, "Electrons in artificial atoms." *Nature* **379**, 413–419 (1996). 1

[2] L. P. Kouwenhoven, T. H. Oosterkamp, M. W. S. Danoesastro, M. Eto, D. G. Austing, T. Honda and S. Tarucha, "Excitation spectra of circular, few-electron quantum dots." *Science* **278**, 1788–1792 (1997). 1, 10

[3] L. P. Kouwenhoven, D. G. Austing and S. Tarucha, "Few-electron quantum dots." *Reports on Progress in Physics* **64**, 701 (2001). 1, 6

[4] W. Lu, Z. Ji, L. Pfeiffer, K. W. West and A. J. Rimberg, "Real-time detection of electron tunnelling in a quantum dot." *Nature* **423**, 422–425 (2003). 1, 104

[5] J. M. Elzerman, R. Hanson, L. H. Willems van Beveren, B. Witkamp, L. M. K. Vandersypen and L. P. Kouwenhoven, "Single-shot read-out of an individual electron spin in a quantum dot." *Nature* **430**, 431–435 (2004). 1, 31, 43

[6] D. Loss and D. P. DiVincenzo, "Quantum computation with quantum dots." *Physical Review A* **57**, 120 (1998). 1, 25, 39, 61, 115

[7] D. P. DiVincenzo, "Quantum computation." *Science* **270**, 255–261 (1995). 1

[8] R. Hanson, J. R. Petta, S. Tarucha and L. M. K. Vandersypen, "Spins in few-electron quantum dots." *Reviews of Modern Physics* **79**, 1217–1265 (2007). 2, 42, 43

[9] M. A. Nielsen and I. L. Chuang, *Quantum Computation and Quantum Information (Cambridge Series on Information and the Natural Sciences)*. Cambridge University Press, (2004). 2, 26, 40, 60, 71, 100

[10] D. DiVincenzo, "Two-bit gates are universal for quantum computation." *Physical Review A* **51**, 1015–1022 (1995). 2

[11] A. Barenco, C. H. Bennett, R. Cleve, D. P. DiVincenzo, N. Margolus, P. Shor, T. Sleator, J. A. Smolin and H. Weinfurter, "Elementary gates for quantum computation." *Physical Review A* **52**, 3457–3467 (1995). 2

[12] D. P. DiVincenzo, "The physical implementation of quantum computation." *Fortschritte der Physik* **48**, 771–783 (2000). 2, 25

[13] A. V. Khaetskii, D. Loss and L. Glazman, "Electron spin decoherence in quantum dots due to interaction with nuclei." *Physical Review Letters* **88**, 186802 (2002). 2, 42, 79

[14] F. H. Koppens, J. A. Folk, J. M. Elzerman, R. Hanson, L. H. van Beveren, I. T. Vink, H. P. Tranitz, W. Wegscheider, L. P. Kouwenhoven and L. M. Vandersypen, "Control and detection of singlet-triplet mixing in a random nuclear field." *Science* **309**, 1346–50 (2005). 2, 31, 45, 46, 65

[15] F. H. L. Koppens, D. Klauser, W. A. Coish, K. C. Nowack, L. P. Kouwenhoven, D. Loss and L. M. K. Vandersypen, "Universal phase shift and nonexponential decay of driven single-spin oscillations." *Physical Review Letters* **99**, 106803 (2007). 2, 71, 72, 78, 80, 83

[16] F. Bloch, "Nuclear induction." *Physical Review* **70**, 460–474 (1946). 2

[17] J. R. Petta, A. C. Johnson, J. M. Taylor, E. A. Laird, A. Yacoby, M. D. Lukin, C. M. Marcus, M. P. Hanson and A. C. Gossard, "Coherent manipulation of coupled electron spins in semiconductor quantum dots." *Science* **309**, 2180–4 (2005). 2, 25, 27, 32, 39, 45, 61, 67

[18] S. A. Wolf, D. D. Awschalom, R. A. Buhrman, J. M. Daughton, S. von Molnár, M. L. Roukes, A. Y. Chtchelkanova and D. M. Treger, "Spintronics: A spin-based electronics vision for the future." *Science* **294**, 1488–1495 (2001). 3

[19] I. Žutić, J. Fabian and S. Das Sarma, "Spintronics: Fundamentals and applications." *Reviews of Modern Physics* **76**, 323–410 (2004). 3

[20] Y. Tokura, W. van der Wiel, T. Obata and S. Tarucha, "Coherent single electron spin control in a slanting Zeeman field." *Physical Review Letters* **96**, 047202 (2006). 3, 34, 36, 48, 62

[21] M. Pioro-Ladrière, T. Obata, Y. Tokura, Y. S. Shin, T. Kubo, K. Yoshida, T. Taniyama and S. Tarucha, "Electrically driven single-electron spin resonance in a slanting Zeeman field." *Nature Physics* **4**, 776–779 (2008). 3, 34, 47, 48, 49, 50, 51, 52, 53, 61, 62, 115

[22] S. Tarucha, D. G. Austing, T. Honda, R. J. van der Hage and L. P. Kouwenhoven, "Shell filling and spin effects in a few electron quantum dot." *Physical Review Letters* **77**, 3613 (1996). 10, 11

[23] M. Ciorga, A. S. Sachrajda, P. Hawrylak, C. Gould, P. Zawadzki, S. Jullian, Y. Feng and Z. Wasilewski, "Addition spectrum of a lateral dot from Coulomb and spin-blockade spectroscopy." *Physical Review B* **61**, R16315–R16318 (2000). 11

[24] M. Jung, K. Hirakawa, Y. Kawaguchi, S. Komiyama, S. Ishida and Y. Arakawa, "Lateral electron transport through single self-assembled InAs quantum dots." *Applied Physics Letters* **86** (2005). 11

[25] C. Fasth, A. Fuhrer, M. T. Björk and L. Samuelson, "Tunable double quantum dots in InAs nanowires defined by local gate electrodes." *Nano Letters* **5**, 1487–1490 (2005). 11

[26] N. Mason, M. J. Biercuk and C. M. Marcus, "Local gate control of a carbon nanotube double quantum dot." *Science* **303**, 655–658 (2004). 11, 116

[27] A. Y. Cho and J. R. Arthur, "Molecular beam epitaxy." *Progress in Solid State Chemistry* **10, Part 3**, 157–191 (1975). 13

[28] T. Mimura, S. Hiyamizu, T. Fujii and K. Nanbu, "A new field-effect transistor with selectively doped GaAs/n-$Al_xGa_{1-x}As$ heterojunctions." *Japanese Journal of Applied Physics* **19**, L225–L227 (1980). 13

[29] B. J. van Wees, H. van Houten, C. W. J. Beenakker, J. G. Williamson, L. P. Kouwenhoven, D. van der Marel and C. T. Foxon, "Quantized conductance of point contacts in a two-dimensional electron gas." *Physical Review Letters* **60**, 848–850 (1988). 14

[30] C. W. J. Beenakker and H. van Houten, *Quantum Transport in Semiconductor Nanostructures*, vol. 44, 1–228. Academic Press, (1991). 14

[31] C. Barthel, M. Kægaard, J. Medford, M. Stopa, C. M. Marcus, M. P. Hanson and A. C. Gossard, "Fast sensing of double-dot charge arrangement and spin state with a radio-frequency sensor quantum dot." *Physical Review B* **81**, 161308 (2010). 14, 104

[32] W. G. van der Wiel, S. De Franceschi, J. M. Elzerman, T. Fujisawa, S. Tarucha and L. P. Kouwenhoven, "Electron transport through double quantum dots." *Reviews of Modern Physics* **75**, 1–22 (2002). 15, 63, 74

[33] T. H. Oosterkamp, T. Fujisawa, W. G. van der Wiel, K. Ishibashi, R. V. Hijman, S. Tarucha and L. P. Kouwenhoven, "Microwave spectroscopy of a quantum-dot molecule." *Nature* **395**, 873–876 (1998). 19, 50, 52, 63

[34] D. Schröer, A. D. Greentree, L. Gaudreau, K. Eberl, L. C. L. Hollenberg, J. P. Kotthaus and S. Ludwig, "Electrostatically defined serial triple quantum dot charged with few electrons." *Physical Review B* **76**, 075306 (2007). 21, 22, 24, 100, 103

[35] T. Takakura, *Observation and control of electron states in lateral multiple quantum dots for realization of spin qubits.* PhD thesis, The University of Tokyo, (2012). 21, 23, 24, 54, 109

[36] L. Gaudreau, S. A. Studenikin, A. S. Sachrajda, P. Zawadzki, A. Kam, J. Lapointe, M. Korkusinski and P. Hawrylak, "Stability diagram of a few-electron triple dot." *Physical Review Letters* **97**, 036807 (2006). 22, 100

[37] G. Granger, L. Gaudreau, A. Kam, M. Pioro-Ladrière, S. A. Studenikin, Z. R. Wasilewski, P. Zawadzki and A. S. Sachrajda, "Three-dimensional transport diagram of a triple quantum dot." *Physical Review B* **82**, 075304 (2010). 22, 24, 100, 103

[38] T. Kobayashi, T. Ota, S. Sasaki and K. Muraki, "Cooperative lifting of spin blockade in a three-terminal triple quantum dot." *ArXiv e-prints* (2013). 24, 100, 109

[39] L. Gaudreau, A. Kam, G. Granger, S. A. Studenikin, P. Zawadzki and A. S. Sachrajda, "A tunable few electron triple quantum dot." *Applied Physics Letters* **95**, 193101 (2009). 24, 100

[40] R. Hanson and D. D. Awschalom, "Coherent manipulation of single spins in semiconductors." *Nature* **453**, 1043–9 (2008). 25, 61

[41] T. D. Ladd, F. Jelezko, R. Laflamme, Y. Nakamura, C. Monroe and J. L. O'Brien, "Quantum computers." *Nature* **464**, 45–53 (2010). 25, 61

[42] D. D. Awschalom, L. C. Bassett, A. S. Dzurak, E. L. Hu and J. R. Petta, "Quantum spintronics: Engineering and manipulating atom-like spins in semiconductors." *Science* **339**, 1174–1179 (2013). 25, 61

[43] J. Levy, "Universal quantum computation with spin-1/2 pairs and heisenberg exchange." *Physical Review Letters* **89**, 147902 (2002). 25

[44] D. P. DiVincenzo, D. Bacon, J. Kempe, G. Burkard and K. B. Whaley, "Universal quantum computation with the exchange interaction." *Nature* **408**, 339–342 (2000). 25

[45] F. H. Koppens, C. Buizert, K. J. Tielrooij, I. T. Vink, K. C. Nowack, T. Meunier, L. P. Kouwenhoven and L. M. Vandersypen, "Driven coherent oscillations of a single electron spin in a quantum dot." *Nature* **442**, 766–71 (2006). 25, 38, 39, 47, 52, 61, 62

[46] J. Medford, J. Beil, J. M. Taylor, S. D. Bartlett, A. C. Doherty, E. I. Rashba, D. P. DiVincenzo, H. Lu, A. C. Gossard and C. M. Marcus, "Self-consistent measurement and state tomography of an exchange-only spin qubit." *Nature Nanotechnology* **8**, 654–659 (2013). 25, 30, 100, 112

[47] L. M. Roth, B. Lax and S. Zwerdling, "Theory of optical magneto-absorption effects in semiconductors." *Physical Review* **114**, 90–104 (1959). 26

[48] J. F. Poyatos, J. I. Cirac and P. Zoller, "Complete characterization of a quantum process: The two-bit quantum gate." *Physical Review Letters* **78**, 390 (1997). 26, 60

[49] J. M. Taylor, J. R. Petta, A. C. Johnson, A. Yacoby, C. M. Marcus and M. D. Lukin, "Relaxation, dephasing, and quantum control of electron spins in double quantum dots." *Physical Review B* **76**, 035315 (2007). 27, 42

[50] E. A. Laird, J. M. Taylor, D. P. DiVincenzo, C. M. Marcus, M. P. Hanson and A. C. Gossard, "Coherent spin manipulation in an exchange-only qubit." *Physical Review B* **82**, 075403 (2010). 30, 100, 106

[51] M. Busl, G. Granger, L. Gaudreau, R. Sánchez, A. Kam, M. Pioro-Ladrière, S. A. Studenikin, P. Zawadzki, Z. R. Wasilewski, A. S. Sachrajda and G. Platero, "Bipolar spin blockade and coherent state superpositions in a triple quantum dot." *Nature Nanotechnology* **8**, 261–265 (2013). 30, 100, 109

[52] L. Gaudreau, G. Granger, A. Kam, G. C. Aers, S. A. Studenikin, P. Zawadzki, M. Pioro-Ladrière, Z. R. Wasilewski and A. S. Sachrajda, "Coherent control of three-spin states in a triple quantum dot." *Nature Physics* **8**, 54–58 (2012). 30, 100, 112

[53] K. C. Nowack, M. Shafiei, M. Laforest, G. E. Prawiroatmodjo, L. R. Schreiber, C. Reichl, W. Wegscheider and L. M. Vandersypen, "Single-shot correlations and two-qubit gate of solid-state spins." *Science* **333**, 1269–72 (2011). 31, 61

[54] K. Ono, D. G. Austing, Y. Tokura and S. Tarucha, "Current rectification by Pauli exclusion in a weakly coupled double quantum dot system." *Science* **297**, 1313–1317 (2002). 31

[55] A. Pfund, I. Shorubalko, K. Ensslin and R. Leturcq, "Suppression of spin relaxation in an InAs nanowire double quantum dot." *Physical Review Letters* **99**, 036801 (2007). 31

[56] N. Shaji, C. B. Simmons, M. Thalakulam, L. J. Klein, H. Qin, H. Luo, D. E. Savage, M. G. Lagally, A. J. Rimberg, R. Joynt, M. Friesen, R. H. Blick, S. N. Coppersmith and M. A. Eriksson, "Spin blockade and lifetime-enhanced transport in a few-electron Si/SiGe double quantum dot." *Nature Physics* **4**, 540–544 (2008). 31, 116

[57] M. R. Buitelaar, J. Fransson, A. L. Cantone, C. G. Smith, D. Anderson, G. A. C. Jones, A. Ardavan, A. N. Khlobystov, A. A. R. Watt, K. Porfyrakis and G. A. D. Briggs, "Pauli spin blockade in carbon nanotube double quantum dots." *Physical Review B* **77**, 245439 (2008). 31

[58] S. Foletti, H. Bluhm, D. Mahalu, V. Umansky and A. Yacoby, "Universal quantum control of two-electron spin quantum bits using dynamic nuclear polarization." *Nature Physics* **5**, 903–908 (2009). 32, 46

[59] L. M. K. Vandersypen and I. L. Chuang, "NMR techniques for quantum control and computation." *Reviews of Modern Physics* **76**, 1037–1069 (2005). 33, 40, 45, 52, 60

[60] F. Koppens, K. Nowack and L. Vandersypen, "Spin echo of a single electron spin in a quantum dot." *Physical Review Letters* **100**, 236802 (2008). 34, 39, 45, 51, 61, 67, 75

[61] S. Nadj-Perge, S. M. Frolov, E. P. Bakkers and L. P. Kouwenhoven, "Spin-orbit qubit in a semiconductor nanowire." *Nature* **468**, 1084–7 (2010). 34, 38, 39, 71, 78

[62] E. Rashba, "Theory of electric dipole spin resonance in quantum dots: Mean field theory with Gaussian fluctuations and beyond." *Physical Review B* **78**, 195302 (2008). 34, 48

[63] T. Takakura, M. Pioro-Ladrière, T. Obata, Y. S. Shin, R. Brunner, K. Yoshida, T. Taniyama and S. Tarucha, "Triple quantum dot device designed for three spin qubits." *Applied Physics Letters* **97**, 212104 (2010). 36, 48, 54, 64, 100

[64] M. Pioro-Ladrière, T. Obata, Y. Tokura, Y.-S. Shin, T. Kubo, K. Yoshida, T. Taniyama and S. Tarucha, "Selective manipulation of electron spins with electric fields." *Progress of Theoretical Physics Supplement* **176**, 322–340 (2008). 36

[65] V. N. Golovach, M. Borhani and D. Loss, "Electric-dipole-induced spin resonance in quantum dots." *Physical Review B* **74**, 165319 (2006). 38, 71

[66] K. C. Nowack, F. H. Koppens, Y. V. Nazarov and L. M. Vandersypen, "Coherent control of a single electron spin with electric fields." *Science* **318**, 1430–3 (2007). 38, 39, 47, 50, 51, 61, 71, 74, 78, 84

[67] J. W. G. van den Berg, S. Nadj-Perge, V. S. Pribiag, S. R. Plissard, E. P. A. M. Bakkers, S. M. Frolov and L. P. Kouwenhoven, "Fast spin-orbit qubit in an indium antimonide nanowire." *Physical Review Letters* **110**, 066806 (2013). 38, 39, 71, 78

[68] E. Laird, C. Barthel, E. Rashba, C. Marcus, M. Hanson and A. Gossard, "Hyperfine-mediated gate-driven electron spin resonance." *Physical Review Letters* **99**, 246601 (2007). 38, 46, 47, 61

[69] T. Obata, M. Pioro-Ladrière, Y. Tokura, Y.-S. Shin, T. Kubo, K. Yoshida, T. Taniyama and S. Tarucha, "Coherent manipulation of

individual electron spin in a double quantum dot integrated with a micromagnet." *Physical Review B* **81**, 085317 (2010). 39, 48, 50, 51, 71, 78

[70] G. Burkard, D. Loss and D. P. DiVincenzo, "Coupled quantum dots as quantum gates." *Physical Review B* **59**, 2070 (1999). 39

[71] T. Meunier, V. Calado and L. Vandersypen, "Efficient controlled-phase gate for single-spin qubits in quantum dots." *Physical Review B* **83**, 121403 (2011). 39, 58, 62

[72] R. Brunner, Y. S. Shin, T. Obata, M. Pioro-Ladrière, T. Kubo, K. Yoshida, T. Taniyama, Y. Tokura and S. Tarucha, "Two-qubit gate of combined single-spin rotation and interdot spin exchange in a double quantum dot." *Physical Review Letters* **107**, 146801 (2011). 40, 41, 48, 49, 51, 54, 61, 62, 78, 99

[73] W. H. Zurek, "Decoherence, einselection, and the quantum origins of the classical." *Reviews of Modern Physics* **75**, 715–775 (2003). 40

[74] J. M. Taylor and M. D. Lukin, "Dephasing of quantum bits by a quasistatic mesoscopic environment." *Quantum Information Processing* **5**, 503–536 (2006). 42, 71, 78, 80

[75] X. Hu and S. Das Sarma, "Charge-fluctuation-induced dephasing of exchange-coupled spin qubits." *Physical Review Letters* **96**, 100501 (2006). 42

[76] O. E. Dial, M. D. Shulman, S. P. Harvey, H. Bluhm, V. Umansky and A. Yacoby, "Charge noise spectroscopy using coherent exchange oscillations in a singlet-triplet qubit." *Physical Review Letters* **110**, 146804 (2013). 42

[77] A. V. Khaetskii and Y. V. Nazarov, "Spin-flip transitions between Zeeman sublevels in semiconductor quantum dots." *Physical Review B* **64**, 125316 (2001). 42, 43

[78] G. Dresselhaus, "Spin-orbit coupling effects in zinc blende structures." *Physical Review* **100**, 580–586 (1955). 42

[79] E. Rashba, "Properties of semiconductors with an extremum loop. 1. Cyclotron and combinational resonance in a magnetic field perpendicular

to the plane of the loop." *Soviet Physics, Solid State* **2**, 1109–1122 (1960). 42

[80] P. Pfeffer, "Effect of inversion asymmetry on the conduction subbands in GaAs-$Ga_{1-x}Al_xAs$ heterostructures." *Physical Review B* **59**, 15902–15909 (1999). 42

[81] S. Amasha, K. MacLean, I. Radu, D. Zumbühl, M. Kastner, M. Hanson and A. Gossard, "Electrical control of spin relaxation in a quantum dot." *Physical Review Letters* **100**, 046803 (2008). 43

[82] V. N. Golovach, A. Khaetskii and D. Loss, "Phonon-induced decay of the electron spin in quantum dots." *Physical Review Letters* **93**, 016601 (2004). 43

[83] W. A. Coish and J. Baugh, "Nuclear spins in nanostructures." *physica status solidi (b)* **246**, 2203–2215 (2009). 43

[84] E. A. Chekhovich, M. N. Makhonin, A. I. Tartakovskii, A. Yacoby, H. Bluhm, K. C. Nowack and L. M. K. Vandersypen, "Nuclear spin effects in semiconductor quantum dots." *Nature Matererials* **12**, 494–504 (2013). 43, 46

[85] D. Paget, G. Lampel, B. Sapoval and V. I. Safarov, "Low field electron-nuclear spin coupling in gallium arsenide under optical pumping conditions." *Physical Review B* **15**, 5780–5796 (1977). 45

[86] I. A. Merkulov, A. L. Efros and M. Rosen, "Electron spin relaxation by nuclei in semiconductor quantum dots." *Physical Review B* **65**, 205309 (2002). 45, 79

[87] W. A. Coish and D. Loss, "Hyperfine interaction in a quantum dot: Non-Markovian electron spin dynamics." *Physical Review B* **70**, 195340 (2004). 45, 46, 78

[88] H. Bluhm, S. Foletti, I. Neder, M. Rudner, D. Mahalu, V. Umansky and A. Yacoby, "Dephasing time of GaAs electron-spin qubits coupled to a nuclear bath exceeding 200μs." *Nature Physics* **7**, 109–113 (2011). 45, 60, 61

[89] K. Ono and S. Tarucha, "Nuclear-spin-induced oscillatory current in spin-blockaded quantum dots." *Physical Review Letters* **92**, 256803 (2004). 46

[90] J. Baugh, Y. Kitamura, K. Ono and S. Tarucha, "Large nuclear Overhauser fields detected in vertically coupled double quantum dots." *Physical Review Letters* **99**, 096804 (2007). 46

[91] G. Petersen, E. A. Hoffmann, D. Schuh, W. Wegscheider, G. Giedke and S. Ludwig, "Large nuclear spin polarization in gate-defined quantum dots using a single-domain nanomagnet." *Physical Review Letters* **110**, 177602 (2013). 46

[92] J. Petta, J. Taylor, A. Johnson, A. Yacoby, M. Lukin, C. Marcus, M. Hanson and A. Gossard, "Dynamic nuclear polarization with single electron spins." *Physical Review Letters* **100**, 067601 (2008). 46

[93] H. Bluhm, S. Foletti, D. Mahalu, V. Umansky and A. Yacoby, "Enhancing the coherence of a spin qubit by operating it as a feedback loop that controls its nuclear spin bath." *Physical Review Letters* **105**, 216803 (2010). 46, 116

[94] I. T. Vink, K. C. Nowack, F. H. L. Koppens, J. Danon, Y. V. Nazarov and L. M. K. Vandersypen, "Locking electron spins into magnetic resonance by electron-nuclear feedback." *Nature Physics* **5**, 764–768 (2009). 46, 67, 116

[95] T. Obata, M. Pioro-Ladrière, Y. Tokura and S. Tarucha, "The photon-assisted dynamic nuclear polarization effect in a double quantum dot." *New Journal of Physics* **14**, 123013 (2012). 46, 67

[96] O. N. Jouravlev and Y. V. Nazarov, "Electron transport in a double quantum dot governed by a nuclear magnetic field." *Physical Review Letters* **96**, 176804 (2006). 46

[97] M. S. Rudner and L. S. Levitov, "Electrically driven reverse Overhauser pumping of nuclear spins in quantum dots." *Physical Review Letters* **99**, 246602 (2007). 46, 52, 67, 116

[98] J. Danon and Y. Nazarov, "Nuclear tuning and detuning of the electron spin resonance in a quantum dot: Theoretical consideration." *Physical Review Letters* **100**, 056603 (2008). 46, 52, 116

[99] J. Danon, I. Vink, F. Koppens, K. Nowack, L. Vandersypen and Y. Nazarov, "Multiple nuclear polarization states in a double quantum dot." *Physical Review Letters* **103**, 046601 (2009). 46, 67, 116

[100] D. Klauser, W. A. Coish and D. Loss, "Nuclear spin state narrowing via gate-controlled Rabi oscillations in a double quantum dot." *Physical Review B* **73**, 205302 (2006). 46, 52, 116

[101] M. S. Rudner and L. S. Levitov, "Self-polarization and dynamical cooling of nuclear spins in double quantum dots." *Physical Review Letters* **99**, 036602 (2007). 46, 116

[102] M. S. Rudner, L. M. K. Vandersypen, V. Vuletić and L. S. Levitov, "Generating entanglement and squeezed states of nuclear spins in quantum dots." *Physical Review Letters* **107**, 206806 (2011). 46, 116

[103] A. Wild, J. Kierig, J. Sailer, J. W. Ager, Iii, E. E. Haller, G. Abstreiter, S. Ludwig and D. Bougeard, "Few electron double quantum dot in an isotopically purified ^{28}Si quantum well." *Applied Physics Letters* **100**, 143110–4 (2012). 48, 116

[104] M. Pioro-Ladrière, Y. Tokura, T. Obata, T. Kubo and S. Tarucha, "Micromagnets for coherent control of spin-charge qubit in lateral quantum dots." *Applied Physics Letters* **90**, 024105 (2007). 48

[105] T. Obata unpublished. 48, 49, 51

[106] F. H. L. Koppens, C. Buizert, I. T. Vink, K. C. Nowack, T. Meunier, L. P. Kouwenhoven and L. M. K. Vandersypen, "Detection of single electron spin resonance in a double quantum dot." *Journal of Applied Physics* **101**, 081706 (2007). 48, 52

[107] J. J. Olivero and R. L. Longbothum, "Empirical fits to the Voigt line width: A brief review." *Journal of Quantitative Spectroscopy and Radiative Transfer* **17**, 233–236 (1977). 52

[108] Y.-S. Shin, T. Obata, Y. Tokura, M. Pioro-Ladrière, R. Brunner, T. Kubo, K. Yoshida and S. Tarucha, "Single-spin readout in a double quantum dot including a micromagnet." *Physical Review Letters* **104**, 046802 (2010). 58, 62

[109] C. Barthel, J. Medford, C. Marcus, M. Hanson and A. Gossard, "Interlaced dynamical decoupling and coherent operation of a singlet-triplet qubit." *Physical Review Letters* **105**, 266808 (2010). 60

[110] T. Fujisawa, D. G. Austing, Y. Tokura, Y. Hirayama and S. Tarucha, "Allowed and forbidden transitions in artificial hydrogen and helium atoms." *Nature* **419**, 278–281 (2002). 61, 112

[111] W. Coish and D. Loss, "Exchange-controlled single-electron-spin rotations in quantum dots." *Physical Review B* **75**, 161302 (2007). 62

[112] T. H. Stoof and Y. V. Nazarov, "Time-dependent resonant tunneling via two discrete states." *Physical Review B* **53**, 1050–1053 (1996). 63

[113] M. Pioro-Ladrière, J. H. Davies, A. R. Long, A. S. Sachrajda, L. Gaudreau, P. Zawadzki, J. Lapointe, J. Gupta, Z. Wasilewski and S. Studenikin, "Origin of switching noise in GaAs/Al_xGa_{1-x}As lateral gated devices." *Physical Review B* **72**, 115331 (2005). 63

[114] C. Buizert, F. H. L. Koppens, M. Pioro-Ladrière, H.-P. Tranitz, I. T. Vink, S. Tarucha, W. Wegscheider and L. M. K. Vandersypen, "*InSitu* reduction of charge noise in GaAs/Al_xGa_{1-x}As Schottky-gated devices." *Physical Review Letters* **101**, 226603 (2008). 63

[115] A. C. Johnson, J. R. Petta and C. M. Marcus, "Singlet-triplet spin blockade and charge sensing in a few-electron double quantum dot." *Physical Review B* **72**, 165308 (2005). 65, 125

[116] C. E. Pryor and M. E. Flatté, "Landé g factors and orbital momentum quenching in semiconductor quantum dots." *Physical Review Letters* **96**, 026804 (2006). 67

[117] M. D. Bowdrey, D. K. L. Oi, A. J. Short, K. Banaszek and J. A. Jones, "Fidelity of single qubit maps." *Physics Letters A* **294**, 258–260 (2002). 71, 95

[118] Y. Tokura private communication. 73

[119] A. J. Leggett, S. Chakravarty, A. T. Dorsey, M. P. A. Fisher, A. Garg and W. Zwerger, "Dynamics of the dissipative two-state system." *Reviews of Modern Physics* **59**, 1–85 (1987). 74

[120] V. V. Dobrovitski, A. E. Feiguin, R. Hanson and D. D. Awschalom, "Decay of Rabi oscillations by dipolar-coupled dynamical spin environments." *Physical Review Letters* **102**, 237601 (2009). 74

[121] F. M. Cucchietti, J. P. Paz and W. H. Zurek, "Decoherence from spin environments." *Physical Review A* **72**, 052113 (2005). 74, 80

[122] F. Beaudoin and W. A. Coish, "Enhanced hyperfine-induced spin dephasing in a magnetic-field gradient." *Physical Review B* **88**, 085320 (2013). 74

[123] W. A. Coish, J. Fischer and D. Loss, "Exponential decay in a spin bath." *Physical Review B* **77**, 125329 (2008). 77

[124] D. J. Reilly, J. M. Taylor, E. A. Laird, J. R. Petta, C. M. Marcus, M. P. Hanson and A. C. Gossard, "Measurement of temporal correlations of the Overhauser field in a double quantum dot." *Physical Review Letters* **101**, 236803 (2008). 79

[125] C. Barthel, D. Reilly, C. Marcus, M. Hanson and A. Gossard, "Rapid single-shot measurement of a singlet-triplet qubit." *Physical Review Letters* **103**, 160503 (2009). 79, 104

[126] M. A. Nielsen, "A simple formula for the average gate fidelity of a quantum dynamical operation." *Physics Letters A* **303**, 249–252 (2002). 95

[127] M. D. Shulman, O. E. Dial, S. P. Harvey, H. Bluhm, V. Umansky and A. Yacoby, "Demonstration of entanglement of electrostatically coupled singlet-triplet qubits." *Science* **336**, 202–205 (2012). 99

[128] J. R. Medford, *Spin Qubits in Double and Triple Quantum Dots*. PhD thesis, Harvard University, (2013). 100, 104

[129] S. N. Shevchenko, S. Ashhab and F. Nori, "Landau-Zener-Stückelberg interferometry." *Physics Reports* **492**, 1–30 (2010). 100, 112

[130] F. R. Braakman, P. Barthelemy, C. Reichl, W. Wegscheider and L. M. K. Vandersypen, "Long-distance coherent coupling in a quantum dot array." *Nature Nanotechnology* **8**, 432–437 (2013). 100

[131] T. Takakura, A. Noiri, T. Obata, T. Otsuka, J. Yoneda, K. Yoshida and S. Tarucha, "Single to quadruple quantum dots with tunable tunnel couplings." *ArXiv e-prints* (2014). 100

[132] F. R. Braakman, P. Barthelemy, C. Reichl, W. Wegscheider and L. M. K. Vandersypen, "Photon- and phonon-assisted tunneling in the three-dimensional charge stability diagram of a triple quantum dot array." *Applied Physics Letters* **102**, 112110 (2013). 100, 103

[133] R. J. Schoelkopf, P. Wahlgren, A. A. Kozhevnikov, P. Delsing and D. E. Prober, "The radio-frequency single-electron transistor (rf-SET): A fast and ultrasensitive electrometer." *Science* **280**, 1238–1242 (1998). 103, 104

[134] D. J. Reilly, C. M. Marcus, M. P. Hanson and A. C. Gossard, "Fast single-charge sensing with a rf quantum point contact." *Applied Physics Letters* **91**, 162101 (2007). 103, 104, 105, 107, 109

[135] L. M. K. Vandersypen, J. M. Elzerman, R. N. Schouten, L. H. Willems van Beveren, R. Hanson and L. P. Kouwenhoven, "Real-time detection of single-electron tunneling using a quantum point contact." *Applied Physics Letters* **85**, 4394–4396 (2004). 104

[136] I. T. Vink, T. Nooitgedagt, R. N. Schouten, L. M. K. Vandersypen and W. Wegscheider, "Cryogenic amplifier for fast real-time detection of single-electron tunneling." *Applied Physics Letters* **91**, 123512 (2007). 104

[137] T. Müller, B. Küng, S. Hellmüller, P. Studerus, K. Ensslin, T. Ihn, M. Reinwald and W. Wegscheider, "An in situ tunable radio-frequency quantum point contact." *Applied Physics Letters* **97**, 202104 (2010). 109

[138] A. C. Johnson, J. R. Petta, J. M. Taylor, A. Yacoby, M. D. Lukin, C. M. Marcus, M. P. Hanson and A. C. Gossard, "Triplet-singlet spin relaxation via nuclei in a double quantum dot." *Nature* **435**, 925–928 (2005). 112

[139] C. Barthel, J. Medford, H. Bluhm, A. Yacoby, C. M. Marcus, M. P. Hanson and A. C. Gossard, "Relaxation and readout visibility of a singlet-triplet qubit in an Overhauser field gradient." *Physical Review B* **85**, 035306 (2012). 112

[140] J. R. Petta, H. Lu and A. C. Gossard, "A coherent beam splitter for electronic spin states." *Science* **327**, 669–72 (2010). 112

[141] K. Khodjasteh and L. Viola, "Dynamically error-corrected gates for universal quantum computation." *Physical Review Letters* **102**, 080501 (2009). 116

[142] K. Khodjasteh, D. A. Lidar and L. Viola, "Arbitrarily accurate dynamical control in open quantum systems." *Physical Review Letters* **104**, 090501 (2010). 116

[143] H. Ingerslev Jørgensen, K. Grove-Rasmussen, K. Y. Wang, A. M. Blackburn, K. Flensberg, P. E. Lindelof and D. A. Williams, "Singlet-triplet physics and shell filling in carbon nanotube double quantum dots." *Nature Physics* **4**, 536–539 (2008). 116

[144] F. Pei, E. A. Laird, G. A. Steele and L. P. Kouwenhoven, "Valley-spin blockade and spin resonance in carbon nanotubes." *Nature Nanotechnology* **7**, 630–634 (2012). 116

[145] E. A. Laird, F. Pei and L. P. Kouwenhoven, "A valley-spin qubit in a carbon nanotube." *Nature Nanotechnology* **8**, 565–568 (2013). 116

[146] B. M. Maune, M. G. Borselli, B. Huang, T. D. Ladd, P. W. Deelman, K. S. Holabird, A. A. Kiselev, I. Alvarado-Rodriguez, R. S. Ross, A. E. Schmitz, M. Sokolich, C. A. Watson, M. F. Gyure and A. T. Hunter, "Coherent singlet-triplet oscillations in a silicon-based double quantum dot." *Nature* **481**, 344–347 (2012). 116

[147] Y. Hu, H. O. Churchill, D. J. Reilly, J. Xiang, C. M. Lieber and C. M. Marcus, "A Ge/Si heterostructure nanowire-based double quantum dot with integrated charge sensor." *Nature Nanotechnology* **2**, 622–5 (2007). 116

[148] A. M. Steane, "Overhead and noise threshold of fault-tolerant quantum error correction." *Physical Review A* **68**, 042322 (2003). 116